Titre: Title:	High Fidelity Numerical Simulation of 3D Arc Extinction in a High Voltage Circuit Breaker
Auteur: Author:	Soheil Namvar
Date:	2020
Type:	Mémoire ou thèse / Dissertation or Thesis
Référence: Citation:	Namvar, S. (2020). High Fidelity Numerical Simulation of 3D Arc Extinction in a High Voltage Circuit Breaker [Ph.D. thesis, Polytechnique Montréal]. PolyPublie. https://publications.polymtl.ca/5268/

POLYTECHNIQUE MONTRÉAL
affiliée à l'Université de Montréal

High Fidelity Numerical Simulation of 3D Arc Extinction in a High Voltage Circuit Breaker

SOHEIL NAMVAR
Département de génie mécanique

Thèse présentée en vue de l'obtention du diplôme de *Philosophiæ Doctor*
Génie mécanique

Avril 2020

POLYTECHNIQUE MONTRÉAL
affiliée à l'Université de Montréal

Cette thèse intitulée :

High Fidelity Numerical Simulation of 3D Arc Extinction in a High Voltage Circuit Breaker

présentée par **Soheil NAMVAR**
en vue de l'obtention du diplôme de *Philosophiæ Doctor*
a été dûment acceptée par le jury d'examen constitué de :

Marcelo REGGIO, président
Jean-Yves TRÉPANIER, membre et directeur de recherche
Ricardo CAMARERO, membre et codirecteur de recherche
Philippe ROBIN-JOUAN, membre et codirecteur de recherche
Massimo CIMMINO, membre
Adrian ILINCA, membre externe

DEDICATION

To my beloved wife, my sons and my parents

. . .

ACKNOWLEDGEMENTS

I wish to declare my sincere thanks to Prof. Jean-Yves Trepánier and Prof. Ricardo Camarero for their support, guidance and wisdom.
I would like to express my gratitude to Mr. Philippe Robin-Jouan for sharing his knowledge constantly through precious comments.

This research is partially supported by General Electric (GE). Also, the financial support from the Simulation-based Engineering Science (Génie Par la Simulation) program funded through the CREATE program from the Natural Sciences and Engineering Research Council of Canada is gratefully acknowledged.

RÉSUMÉ

Cette recherche vise la simulation numérique 3D de l'arc dans un disjoncteur à haute tension SF6 à courant zéro. Dans le but de capturer et de quantifier les instabilités 3D de l'arc à courant zéro, la méthode des volumes finis est utilisée pour résoudre des équations Euler (modifiées pour les gaz réel). La méthode WENO (Weighted Essentially Non-Oscillatory) est utilisée pour atteindre une précision spatiale du 5e ordre pour une compréhension à haute résolution des phénomènes complexes impliqués dans la simulation d'arc. Le chauffage ohmique est obtenu en utilisant une méthode de différence finie compacte du 4ème ordre et le transfert d'énergie radiative est modélisé via la méthode P1. Une méthode TVD Runge-Kutta de troisième ordre est implémentée pour l'intégration temporelle. Le domaine de calcul est un cuboïde, discrétisé en maillage cartésien, à l'intérieur de la buse du disjoncteur qui comprend l'arc et exclut les parois solides et les deux électrodes. L'arc est allumé via un code interne à l'intérieur de la buse. Les résultats sont ensuite cartographiés sur le cuboïde et le courant est réduit à zéro une fois que l'état stationnaire est atteint. Pour étudier les effets 3D de l'arc, une légère asymétrie est imposée à la configuration du problème en déplaçant le domaine de calcul de sorte que l'axe de l'arc ne coïncide pas avec la ligne de symétrie du cuboïde. L'effet de ce déplacement est mesuré sur la résistance électrique du milieu gazeux à l'arc. En comparant le profil numérique de température radiale avec la mesure de température, il est conclu que le schéma WENO et les résultats du premier ordre tombent dans une plage de précision acceptable et la méthode WENO prédit un profil de température plus précis. On observe également que les résultats sont plus précis pour le noyau d'arc que pour les frontières d'arc, en raison de l'absence des termes visqueux responsables de la diffusion d'énergie et du mélange turbulent. Il est également conclu que les équations d'Euler sont capables de capturer les effets 3D de l'arc. Ces effets doivent être pris en compte dans la conception des disjoncteurs car ils sont directement proportionnels à la résistance du milieu gazeux qui a un fort impact sur l'efficacité du disjoncteur.

ABSTRACT

This research aims at 3D numerical simulation of arc inside an SF6 high voltage circuit breaker at current zero. With the goal of capturing and quantifying the arc 3D instabilities at current zero, FVM is used to solve real-gas-modified Euler equations. A Weighted Essentially Non-Oscillatory (WENO) method is employed to reach a 5^{th} order spatial accuracy for a better understanding of complex phenomena involved in the arc simulation. The ohmic heating is solved using a 4^{th} order compact finite difference method and the radiative energy transfer is modelled via P1 method. A 3^{rd} order TVD Runge-Kutta integration method is implemented to represent the solver evolution in time. The computational domain is a cuboid, discretized on a Cartesian grid, inside the circuit breaker nozzle which includes the arc and excludes the nozzle walls and the two electrodes. The arc is ignited via an in-house code inside the nozzle. The results are then mapped to the cuboid and the current is ramped down to zero once the steady state is reached. To investigate the arc 3D effects, a slight asymmetry is imposed to the problem configuration by moving the computational domain so the arc axis does not coincide the line of symmetry of the cuboid. The effect of this displacement is measured on the arc gaseous medium resistance. Comparing the numerical radial temperature profile with temperature measurement, it is concluded that although both the WENO scheme and the 1^{st} order results fall into an acceptable range of accuracy, the WENO method predicts a more accurate temperature profile. It is observed that the results are more accurate for the arc core than the arc boundary, due to the absence of the viscous terms who are responsible for energy diffusion and turbulent mixing in the arc boundary. It is concluded that the Euler equations are capable of capturing the arc 3D effects. These effects should be considered in circuit breakers design since they are directly proportional to the medium resistance which has a strong impact on the circuit breaker efficiency.

TABLE OF CONTENTS

LIST OF TABLES

LIST OF FIGURES

LIST OF SYMBOLS AND ACRONYMS

CFD	Computational Fluid Dynamics
CZ	Current Zero
DOM	Discrete Ordinate Method
GCB	Gas Circuit Breaker
HVCB	High Voltage Circuit Breaker
IBM	Immersed Boundary Method
LES	Large Eddy Simulation
LTE	Local Thermodynamic Equilibrium
M-B	Maxwell-Boltzmann
MHD	Magnetohydrodynamics
MMS	Method of Manufactured Solutions
NEC	Net Emission Coefficient
PML	Prandtl Mixing Length
PTFE	Polytetrafluoroethylene
RANS	Reynolds Averaged Navier-Stokes
RRRV	Rate of the Rise of Recovery Voltage
TRV	Transient Recovery Voltage
WENO	Weighted Essentially non Oscillatory

LIST OF APPENDICES

CHAPTER 1 INTRODUCTION

A circuit breaker is a device that cuts off the current when a fault occurs in an AC power distribution network. To safely perform this task in a high voltage network, the circuit is opened by separating two mechanically driven electrodes as shown in Fig. 1.1. Because of the high voltage, the electric current persists and heats the gas until it is ionized and a plasma channel (the electric arc) forms between the two electrodes. At the natural passage to current zero (CZ) in an AC network, the arc is cooled, stabilized and extinguished by a high pressure cold gas (usually SF6) which is blown into the nozzle containing the electrodes.

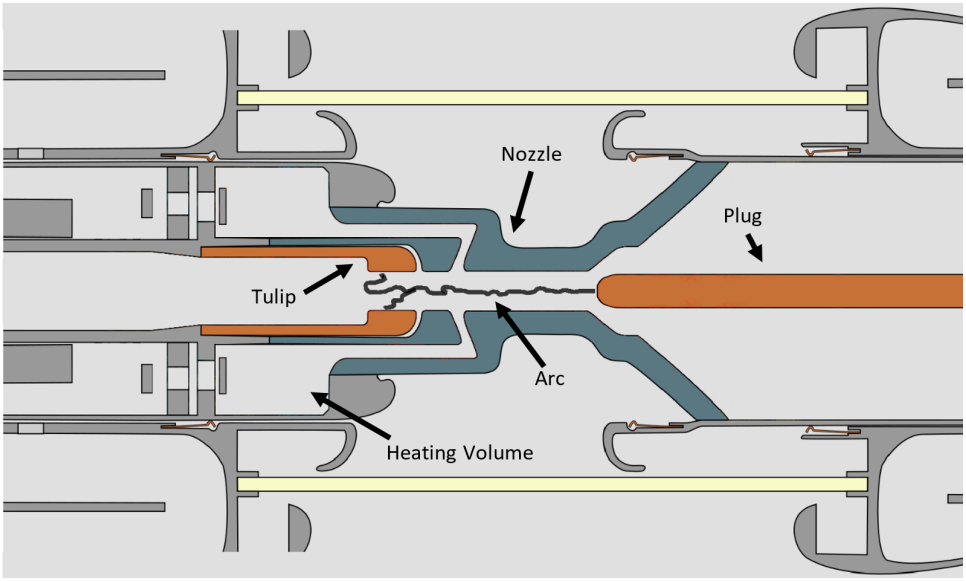

Figure 1.1 Section of a high voltage circuit breaker

The operation of a Gas Circuit Breaker (GCB) can be divided into three steps [1]:

1. Back heating phase: at sufficiently high current, the radiative heat emitted from the arc ablates the surrounding nozzle walls which are generally made of polytetrafluoroethylene (PTFE). This increases the pressure which causes back-flow to the heating volume.

2. Out flow phase: the gas from the back flow mixes with the cold gas inside the heating volume causing a rise in pressure. The gas mixture then flows into the arc zone.

3. Extinction: when the AC current reaches zero, the colder gas is blown over the arc, the conductance of the gaseous medium starts to decreases as the hot conductive plasma is

cooled. At CZ (Fig. 1.2), the applied network voltage starts to recover, which is referred to as Transient Voltage Recovery (TRV) [2]. This voltage applied on a resistance may form a post-arc, making the gaseous medium conductive, resulting in an extinction failure. In such a case, the extinction process is performed at the next CZ. After two failures, the GCB can be destroyed.

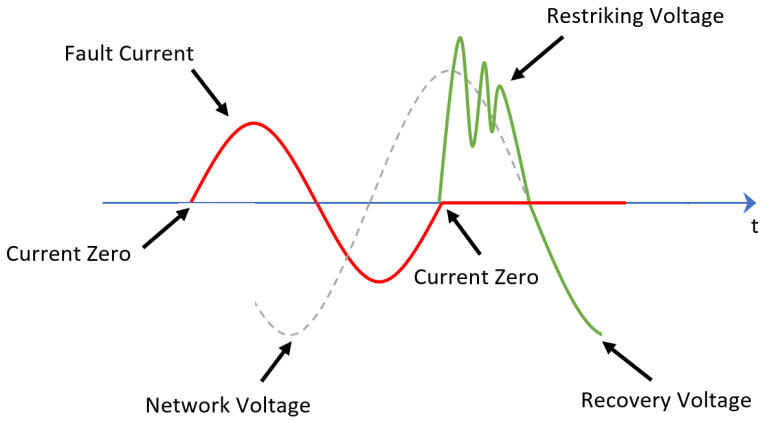

Figure 1.2 Voltage and current variations during current cut-off

1.1 Need for Research

HVCBs should be able to interrupt currents in the range of up to 100 kA, in the order of ten milliseconds. In this context, the detailed design of this device becomes very important. Circuit breaker manufacturers are investing large resources to keep this development ongoing.

Due to the extreme operating conditions, the experimental investigation of such devices are very limited. Numerical simulation, on the other hand, has proven capable of predicting the gas properties at a low cost. This allows useful design parameters to be considered in the development of circuit breakers. Despite the numerous explorations conducted in this area, the arc behaviour needs to be investigated more thoroughly in a 3D context at the time of CZ since failure or success of the current cut happens at the vicinity of this point.
An in-house code (MC^3) has been developed at École Polytechnique de Montréal by Computational Engineering Research Group (GRMIAO) with a specific application to design HVCBs. This software is capable of grid generation, simulation and post-processing (Fig. 1.3 and Fig. 1.4). The solver uses FVM to solve 2D axisymmetric Euler equations with 1^{st} order accuracy. The solution includes the dominant physical phenomena for arc simulation i.e. Ohmic heating, Lorentz force and radiation. Additional transport equations are also employed to account for multi-species gas flow.

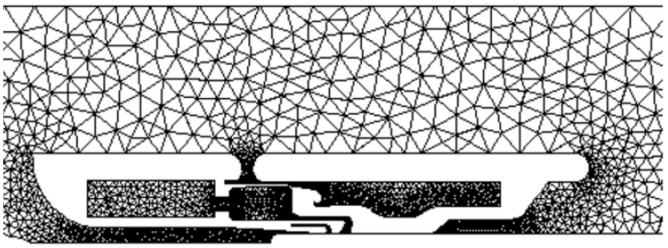

(a) Circuit closed (electrodes attached)

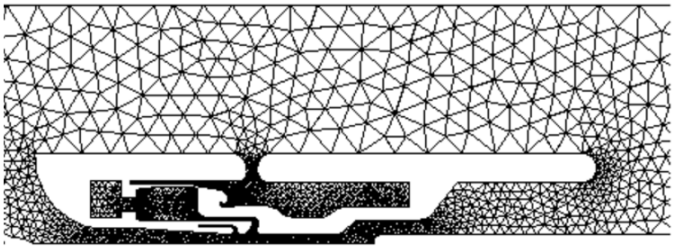

(b) Circuit open (electrodes detached)

Figure 1.3 MC^3 dynamic grid generation

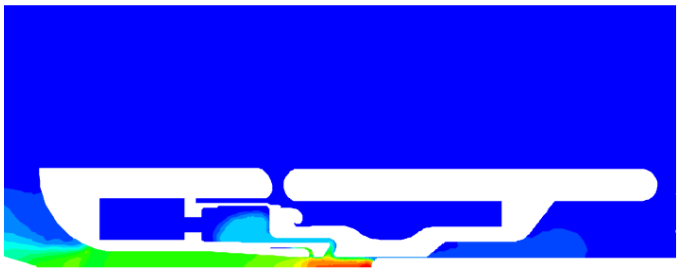

(a) Temperature

(b) Pressure

Figure 1.4 Arc-flow properties for a circuit breaker obtained from MC^3

Although for high-current flows an axisymmetric model, as in MC^3, responds well to the arc

simulation requirements, a 3D approach is needed to investigate the arc details when the current approaches zero. In this phase, the accurate prediction of arc temperature and the medium resistance are vital for an efficient circuit breaker design.
This project will contribute to the extension of MC^3 capabilities towards an accurate arc extinction simulation. The current research exploits high order schemes for solving the gas flow equations and for calculating the energy source terms. With many complex physical phenomena involved in an arc-flow, a high order simulation contributes to a better understanding of the flow and the arc properties.

1.2 Thesis Objectives

At CZ, the resistance of the gaseous medium is highly dependent on the gas properties (i.e density, temperature and pressure). Under the condition of low resistance during CZ, the high electric potential may cause the occurrence of post-arcs as the medium may become conductive again, leading to a failure for the circuit breaker to cut the current. Therefore, an accurate gas property calculation leads to a better prediction of the arc resistance needed for the evaluation of circuit breaker failure.

A 3D simulation able to predict the gas properties with sufficient accuracy will contribute to the design of the next generation of circuit breakers. The general goal of this thesis is to develop and validate a methodology for the numerical investigation of a 3D arc. The objectives to accomplish this goal are:

1. Development and verification of a code to predict the gas properties of arc plasma by solving the flow and the source term equations. Using high order schemes, this code will be able to handle 3D arc simulations with coarser grids as compared to 1^{st} order schemes. This is an enabling tool to investigate and understand arc behaviour.

2. Quantification of the 3D features' impact on important arc characteristics e.g. resistance, voltage, etc. This will be achieved by applying the code to a specific problem with known initial conditions, boundary conditions and measurements. Once the code is validated by comparing the results, further measurements will be carried out.

3. Improvement of MC^3 for 3D arc simulations near CZ by coupling it with the tool developed in this research. Being 2D axisymmetric, MC^3 can be used to initialize the arc. The results of the arc initialization can then be mapped to the 3D code where the current can be ramped down to CZ and 3D effect can be investigated.

   Using high order accuracy for solving the flow and source terms equations, this research

gives an insight into the complex phenomena and their influence during CZ while paving the way for further developments in MC^3.

1.3 Thesis Structure

In Chapter 2, the different phenomena involved in arc simulation are presented as well as their equations. Each phenomenon is accompanied by literature review for a better understanding of available models and numerical schemes. Chapter 3 addresses the general methodology for arc simulation while elaborating on the used models and numerical schemes. Chapter 4 starts with test cases to verify the accuracy of each component of arc simulation, separately, and ends with a test case which integrates all components. Chapter 5 is dedicated to results validation. In this chapter, the arc temperature profile obtained from numerical schemes is compared to the experiment. Once the the simulation is validated, contours and curves of the flow (temperature, pressure, density, Mach and velocity) are discussed at CZ. The arc's global parameters such as resistance and voltage are also presented. This chapter is finalized with an investigation on arc's 3D effects. Chapter 6 discusses the conclusions, limitations and the future research.

CHAPTER 2 Arc literature review and governing equations

A plasma is a mixture of electrons, ions and neutral particles (Fig. 2.1) such that the collection is electrically neutral [3]. Due to the presence of free electrons, plasma is electrically conductive. Ions and neutrals are categorized as heavy particles since their masses are much higher than electrons (the mass ratio is 1840 in Helium). Such a mixture is frequently referred to as the fourth state of matter since 99% of the known universe is composed of plasma [4].

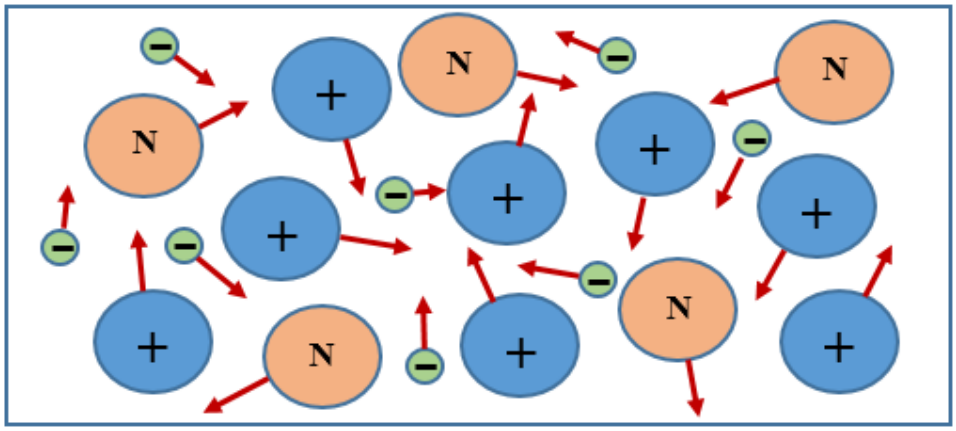

Figure 2.1 Schematic of plasma containing electrons, ions and neutrals

2.1 Thermal plasmas and LTE (Local Thermodynamic Equilibrium) state

Plasmas are characterized fundamentally by their temperature, density and magnetic field. Other properties can be obtained from these fundamental parameters [5]. Fig. 2.2 shows plasma classification of various occurrences of plasmas.

In order to describe the macroscopic properties of a gas, a distribution function is introduced since the gas molecules do not travel at the same speed. The Maxwell-Boltzmann function defines the most probable velocity distribution in a gas at a certain temperature. This distribution function which forms the basis of the gas kinetic theory can be expressed as follows.

$$f(v) = \frac{4}{\sqrt{\pi}}\left(\frac{2kT}{m}\right)^{\frac{3}{2}} v^2 \exp\left(-\frac{mv^2}{2kT}\right) \tag{2.1}$$

where m is the mass of the particle, v is the particle velocity, T represents absolute temperature and k is the Boltzmann constant. The distribution function $f(v)$ is shown in Fig. 2.3

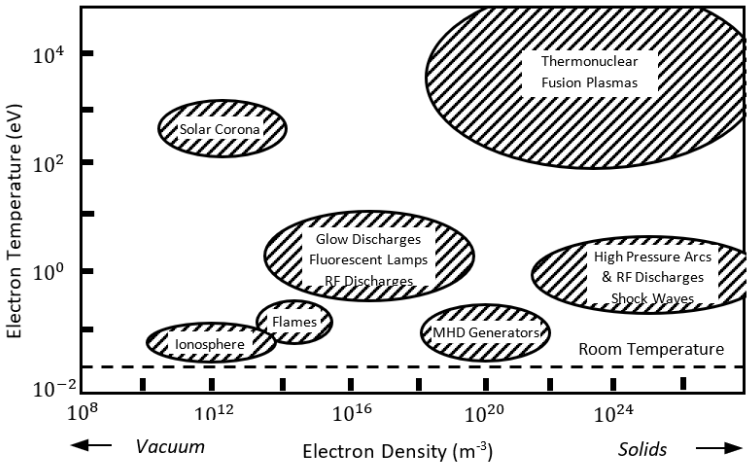

Figure 2.2 Plasma classification based on density and temperature [4]

which reaches the maximum (the most probable velocity) at $v_m = (\frac{2kT}{m})^{\frac{1}{2}}$.

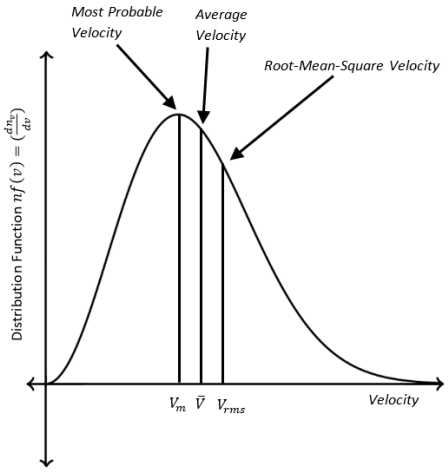

Figure 2.3 Maxwell-Boltzmann (M-B) distribution of velocities in a gas at temperature T

From this distribution, the average velocity can be calculated as

$$\bar{v} = \int_0^\infty v f(v) dv = (\frac{8kT}{\pi m})^{\frac{1}{2}} \tag{2.2}$$

and the mean-square velocity is given by

$$\bar{v^2} = \int_0^\infty v^2 f(v) dv = \frac{3kT}{m} \tag{2.3}$$

A plasma that follows the M-B distribution is referred to as a thermal plasma. In such a plasma, the mixture of ions, electrons and neutrals can be described by a unique temperature. As shown in Eq. 2.4, this temperature is defined by the average kinetic energy of particles obtained from Eq. 2.3.

$$\frac{1}{2}m\bar{v^2} = \frac{3}{2}kT \tag{2.4}$$

Thermal plasmas are by definition in or close to LTE. This state depends strongly on the frequency of the colliding particles and their energy exchange during a collision. The exchange of kinetic energy between two particles with masses m and m' is given by

$$\Delta E_{kinetic} = \frac{2mm'}{(m+m')^2} \tag{2.5}$$

For a collision between particles of the same mass the energy exchange is simply $\Delta E_{kinetic} = \frac{1}{2}$. In a collision-dominated (hot) plasma any particle that deviates from the M-B distribution is collided by many particles. Thus, any distortion from the M-B distribution will be quickly (by less than 10 collisions) damped [4]. In this situation, the plasma will be in kinetic equilibrium which is one of the basic requirements of LTE existence. In such an equilibrium the heavy particles' temperature approaches the electron temperature ($T_e = T_h$) hence the plasma is said to be in kinetic equilibrium. The temperature of thermal (or LTE, equilibrium, hot) plasmas is usually around 10^4 K and their electron densities range from 10^{21} to 10^{26} m^{-3}. Typically, the pressure in LTE plasmas exceed 10 kPa. As shown in Fig. 2.4, for pressures less than 10 kPa the electron and heavy particle temperature curves diverge ($T_e > T_h$).

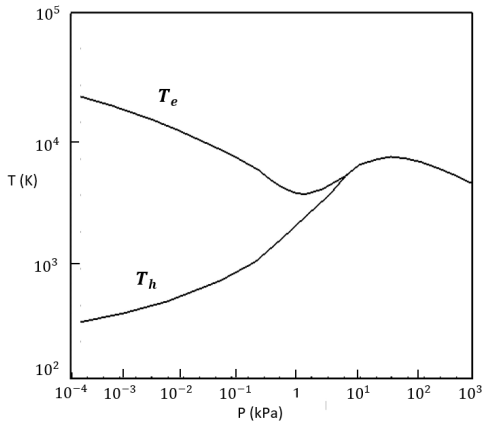

Figure 2.4 Behavior of electron temperature T_e and heavy particle temperature T_h in an arc plasma [4]

2.1.1 LTE in Circuit Breakers

Generally, the plasma produced inside a circuit breaker can be treated as a fluid and described by one temperature according to LTE assumption [6]. However, all the arc zone can not be assumed to be in LTE. Thus, departures from LTE have been addressed in researches such as [7] where the plasma is simulated using a two-temperature model close to electrodes (sheath region shown in Fig. 2.5).

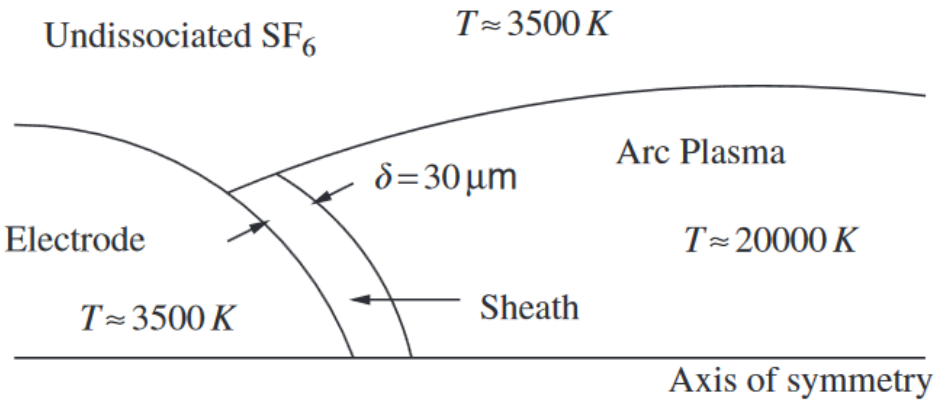

Figure 2.5 Sheath region near electrodes in arc simulation [7]

It is worth mentioning that due to the variable gas properties such as specific heat (shown in Fig. 2.6) in constant pressure and volume (C_V, C_P) the equation of state can be used locally (not globally). The gas properties are hence obtained from tabulated data as functions of temperature, pressure, density and component ratio.

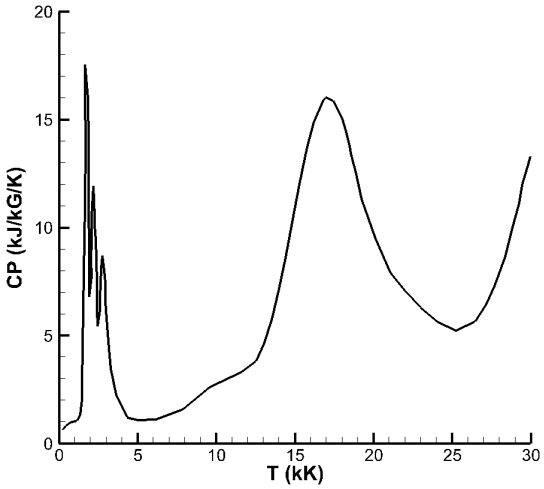

Figure 2.6 Variation of specific heat of SF6 with temperature at 0.1 bar [8]

2.2 Governing Equations

Supposing to be in LTE, the plasma flow can be treated as a fluid. The macroscopic properties of the fluid such as pressure, velocity, density and temperature are obtained by the mass, momentum and energy conservation laws. Hence, the governing equations of an arc inside a circuit breaker can be stated as a general advection-diffusion equation with inclusion of source terms as shown in Eq. 2.6.

$$\frac{\partial(\rho\phi)}{\partial t} + \nabla.(\rho\phi\overrightarrow{V}) - \nabla.(\Gamma_\phi \nabla_\phi) = S_\phi \tag{2.6}$$

where ϕ is the dependent variable, ρ is the gas density, Γ is the diffusion coefficient and S is the source term. The physical phenomena involved in a GCB are numerous and complex including the flow of a compressible gas from subsonic to supersonic speeds [14], ablation (wall evaporation), radiation, ohmic heating and Lorentz force (caused by magnetic field). Fig. 2.7 shows a schematic overview of physical phenomena included in an electric arc.

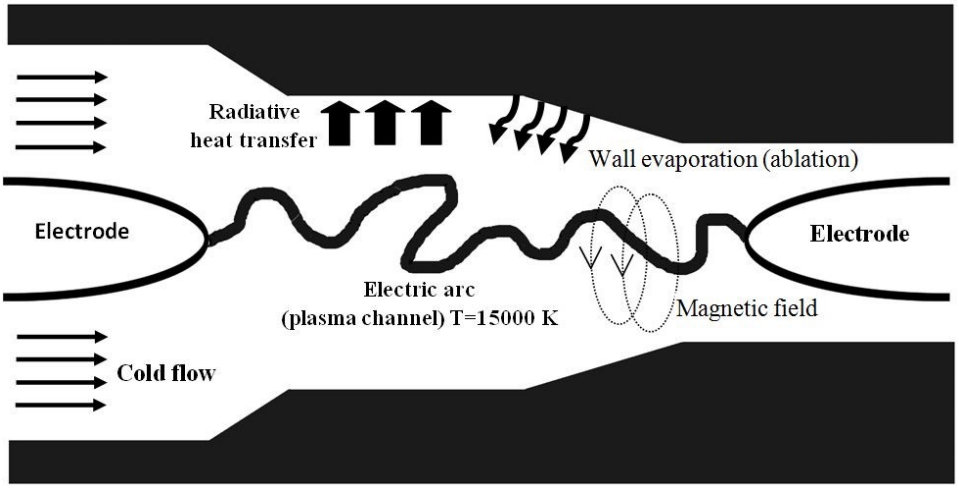

Figure 2.7 Physical phenomena included in arc simulation

2.2.1 Ohmic Heating (Joule's Effect)

As a current passes through a resistance, it produces heat which is known as Joule or Ohmic heating. Because of the high current in the circuit breaker, Joule heating plays a dominant role in the energy balance and should be considered as a source term in the energy equation. By Ohm's law in a conducting medium, the electric current density is

$$J = \sigma E \tag{2.7}$$

where $\sigma = \sigma(P, T)$ is the electrical conductivity of the fluid and E is the electrical field. From $E = -\nabla\phi$ and considering the conservation of electric current, the following relation can be derived,

$$\nabla.(\sigma\nabla\phi) = 0. \tag{2.8}$$

Solving Eq. 2.8 for ϕ, the electric field can be calculated by taking the gradient of electric potential. Finally, according to Joule's law, ohmic heating will be

$$S_{ohm} = \sigma E^2 \tag{2.9}$$

2.2.2 Electromagnetic Field (Lorentz Force)

At high currents, the Lorentz force plays an important role in arc behaviour. This is particularly important near the electrodes where the current density is high [9]. To evaluate the effect of the magnetic field on the flow properties such as pressure and temperature, Maxwell's equations are coupled to the Navier-Stokes equations resulting in magnetohydrodynamics (MHD). The Lorentz force is the main source term for the momentum equation computed as follows

$$F_{LORENTZ} = \overrightarrow{J} \times \overrightarrow{B} \tag{2.10}$$

where $\overrightarrow{J}$ is the current density and $\overrightarrow{B}$ is the magnetic field. The magnetic field is computed using simplified Maxwell's Eqs. [9]

$$\nabla.\overrightarrow{B} = 0 \tag{2.11}$$

$$\nabla.\overrightarrow{J} = 0 \tag{2.12}$$

$$\nabla \times \overrightarrow{E} = 0 \tag{2.13}$$

$$\nabla \times \overrightarrow{H} = 0 \tag{2.14}$$

where $\overrightarrow{H}$ represents the self-induced magnetic field defined as follows

$$\overrightarrow{B} = \mu_0 \overrightarrow{H} \tag{2.15}$$

with μ_0 being the magnetic permeability of empty space.

Taking the curl of Eq. 2.14, one may write

$$\nabla(\nabla.\overrightarrow{H}) - \nabla^2\overrightarrow{H} = \nabla \times \overrightarrow{H} \tag{2.16}$$

from which the magnetic field $\overrightarrow{H}$ can be obtained. It is important to mention that in this research, the effect of magnetic field is neglected since for the range of currents (<1000 A) used in the simulations, the Lorentz force can be neglected.

2.2.3 Radiation

Radiative heat transfer is one of the dominant energy transport mechanisms in high temperature plasmas, and as such it is the most important cooling mechanism of arc and the reason of nozzle wall ablation [10]. The available methods to include the radiative heat transfer in circuit breaker simulations are Net Emission Coefficient (NEC), P1 and Discrete Ordinates Method (DOM).

Net Emission Coefficient (NEC) Model

NEC is one of the earliest and yet the simplest model [11]. It is basically obtained by replacing the arc by an isothermal cylinder of radius R for which the net emission coefficient ε_N at the center can be found as

$$\varepsilon_N = \int_0^\infty B_v K_v exp(-K_v R) dv \tag{2.17}$$

where B_v is the black body radiation, K_v is the absorption coefficient and R is the isothermal cylinder radius. In this equation, light scattering is neglected and the LTE is assumed for the gas [12]. Investigations have been carried out to calculate NEC and its dependence on pressure, temperature and arc radius [13]. It has been found that this semi-empirical model is adequate for the radiative heat transfer in the core of the arc. However, it is not capable of giving an accurate temperature profile at the edge of the arc [12]. This is due to the fact that it is based on emission only and the absorption needs to be defined empirically [10]. Due to the low cost and more accurate results in the arc center, this model has been widely used [14] while improved methods have been developed for temperature profiles away from the center of the arc.

P1 Model

The P1 model is derived from the conservation of the radiative energy along a path of direction $\hat{s}$ (equation 2.18) [16]

$$\frac{dI_v}{ds} = \nabla I_v|_{\hat{s}}.\hat{s} = K_v I_{bv} - \beta_v I_v + \frac{\sigma_{sv}}{4\pi}\int_{4\pi} I_v(\hat{s}_i)\Phi(\hat{s}_i,\hat{s})d\Omega_i \tag{2.18}$$

where I_v is the spectral radiative intensity in a direction $\hat{s}$ at a frequency v, k_v is the coefficient of absorption and σ_{sv} is the coefficient of scattering. $\beta_v = K_v + \sigma_{sv}$ is known as the extinction coefficient and $\Phi(\hat{s}_i,\hat{s})$ is the phase function [17]. Following some simplifications [18] Eq. 2.18 becomes

$$\frac{dI_v}{ds} = \nabla I_v|_{\hat{s}}.\hat{s} = K_v(I_{bv} - I_v) \tag{2.19}$$

In this model, it is assumed that the radiative intensity can be expressed as a Fourier series as,

$$I_v(r,\hat{s}) = \sum_{l=0}^{\infty}\sum_{m=-l}^{l} I_l^m(r)Y_l^m(\hat{s}). \tag{2.20}$$

The two variables $I_l^m(r)$ and $Y_l^m(\hat{s})$ correspond to coordinates and direction, respectively. The model considers the first term of this Fourier series and it can be shown that the intensity can be related to G_v, the incident radiation as follows [16]

$$\nabla.(\frac{1}{K_v}\nabla G_v) = 3K_v(G_v - 4\pi I_{bv}). \tag{2.21}$$

While the P1 model provides more detailed information about radiative heat transfer than the NEC model the most prominent shortcomings can be stated as follows:

1. Lack of realistic boundary conditions
2. Numerical instabilities caused by assumptions and approximation
3. Inherent diffusive behaviour

These drawbacks finally lead to non-physical results in some situations in 2D geometries [16].

Discrete Ordinates Method (DOM)

In this model, the radiative transfer equation is discretized spatially and the integral over the directions is approximated by a sum over a finite number of directions (ordinates) sweeping the total solid angle of 4π. This model is computationally expensive since the equations are

solved for several directions and different frequency bands [10]. Although DOM is considered to have great accuracy [19] some serious drawbacks prevent its use for the entire domain of arc. The main disadvantage being that it does not guarantee the conservation of radiant energy. It also suffers from false scattering caused by spatial discretization and ray effect [20]. Currently, a combination of P1 and DOM models is recommended for circuit breaker simulations [10] i.e. P1 is applied to the core of the arc while DOM is used elsewhere. In this way the efficiency of P1 and accuracy of DOM can be exploited at the same time.

2.3 Ablation

The rate of mass ablation is the evaporation of the nozzle wall (PTFE) caused by the incidental radiative heat transfer. It is important to consider ablation in arc simulation since it contributes to pressure build up in the heating volume [21]. Ablation is modeled in the following manner

$$\dot{m} = \frac{q_{surface}}{h_v + h_{PTFE}} \tag{2.22}$$

where $q_{surface}$ is the radiative heat transfer emitted to the nozzle walls, h_{PTFE} is the enthalpy necessary for PTFE to produce gaseous plasma at 1000 K, and h_v is the enthalpy to increase the plasma temperature from 1000 to 3500 K. The PTFE vapor is mixed with the SF6 flow inside the circuit breaker and forms a multi-species flow. With the change of nozzle wall geometry its efficiency decreases. That is why efforts have been made to calculate the change in nozzle geometry and include it in circuit breaker simulation [22].

2.4 Turbulence

Fang et al. [23] investigated the arc extinction considering a laminar flow. The predicted arc temperature profile was more accurate at the arc core than the arc boundaries. It was inferred that the absence of turbulence was the reason of the simulation inaccuracy in arc boundaries. Furthermore, this research led to another article in which the effect of turbulence was included in the simulation [25]. The final conclusion was that arc boundaries can be predicted more accurately when turbulence is accounted for in the simulations.

The gas inside a circuit breaker undergoes a large acceleration due to the rapid expansion caused by the ohmic heating. The mixture of a hot plasma with a cold gas causes high temperature gradients. Large acceleration, high temperature gradients together with the effect of Lorentz force make the flow unstable and turbulent [19]. As an energy transfer mecha-

nism, turbulence is considered to impact flow characteristics during the following phases of HVCBs [1]:

1. In the back heating phase, turbulent mixing of hot gas from the arc zone and the cold gas takes place in the heating volume.

2. In the out-flow phase, high pressure gas flows into the arc zone to cool the arc. Turbulent mixing plays a significant role in mixing hot plasma and the cold gas. To account for the arc physics, particularly at the arc boundaries, a turbulence model should be coupled with the numerical simulation.

3. After CZ, the dielectric withstand of the gas becomes an important variable which is determined by flow parameters dependent on turbulence [1].

Delalondre et al. [27] conducted a 2D axisymmetric numerical simulation to investigate arc turbulence. Three turbulence models were applied to a 5000 A, 20 cm long arc in a 1 bar air. Assuming the presence of both laminar and turbulent regimes, the standard $K-\varepsilon$, low Reynolds $K-\varepsilon$ and the Reynolds stress models were tested. Comparing the mean temperature profiles, they noticed that the maximum predicted temperature is highly dependent on the turbulence model, i.e 50000 K for the Reynolds Stress model, 31000 K for the standard $K-\varepsilon$ model and 46000 K for the low Reynolds $K-\varepsilon$ model. Furthermore, the arc radius was also predicted differently when different models were applied. The turbulence rate curves suggested a higher turbulence rate in the arc fringe where it is exposed to colder gas than in the core of the plasma.

In addition, an LES model was applied to a 1000 A transient arc cooled by SF6 with back pressure of 5 bars [27]. The methodology of this 3D simulation consists in choosing a box as a computational domain to exclude the electrodes and include a part of the arc. As a result, turbulent energy transport is plotted radially across the arc and compared to ohmic heating and radiative heat transfer. It is suggested that the ohmic and radiative energies are stronger sources to drive the arc compared to turbulent transport energy.

High viscosity variation, various length and time scales and fast transfer of energy source in terms of short circuits have made turbulence modelling a challenge in HVCBs [24].

The objectives of the present research will be better accomplished if turbulence is not considered in the simulation. The reason can be elaborated in the three following categories:

1. Focus Divergence

The application of different turbulence models in arc simulation remains an issue which needs more investigation. Although some issues are clarified about turbulence (e.g. pressure inside the heating volume does not depend on turbulence and could be considered laminar) for the arc zone turbulence modelling, specially near CZ, there is "no consensus" [10]. The literature is dominated by the K-epsilon family models while this model is not able to predict the arc-flow interaction accurately. This model assumes a fully developed flow in its derivation [27] while the rapid interactions in the vicinity of current-zero, prevent the flow to become fully developed. Another drawback of this model is that there are four constants involved in the k and ε transport equations to be determined with the help of experimental data [34] which are absent for the internal configuration found in HVCB geometries. This model does not yield unique results when applied to arcs with different currents [26]. Some works [10], suggest LES as an accurate and suitable turbulence model in which the number of adjustable constants is significantly reduced. A drawback of LES is the large computational cost since for a high accuracy, a finer mesh is essentially needed [33].

2. Arc Core VS Arc Boundary

   It is inferred from the literature that the turbulent mixing is a dominant transport mechanism in the arc boundary while the arc core is more influenced by convective (inviscid) terms. With experimental data and numerical simulations available for arc core temperature, the numerical simulation of this research can be validated for the arc core even if the diffusion-dominated part of the arc is neglected.

3. Simplicity

   The objective of this thesis is investigating the CZ in a 3D context. This investigation can be established with less complexities if Euler equations are used. The methodology, as explained in Section 3, is to apply 1^{st} and 5^{th} order methods to simulate the arc and compare the results. Including the viscous terms requires a 1^{st} and a 5^{th} order method of calculation to comply with the global order of accuracy. This adds a drastic complication to the arc simulation. While the simulation methodology is simplified by avoiding the walls as well as using Cartesian mesh, using Euler equations instead of Navier-Stokes equations adds another level of simplicity to this research.

2.5 Current-Zero

One of the earliest investigations on the arc phenomena were carried out by Frind et al. [35]. In this experiment, an arc was initialized with a 2000A current and was decreased toward

zero at a linear rate. An important parameter studied was the Rate of the Rise of Recovery Voltage (RRRV) around CZ. The results were compared for air and SF6 for different pressures and current decay rates. Hermann et al. [36] carried out an experimental study for a 2000A peak current arc cooled by nitrogen. This included pressure measurements on the wall as well as axial and radial measurements while the current is held steady at the peak. The current was ramped down afterwards, with a constant decay rate. The unsteady experiment is accompanied by axial temperature decay measured in the vicinity of CZ. Both steady and unsteady measurements are compared to calculations where relatively good agreement was observed. This work also provides some detailed experimental information on the laminar and turbulent part of the arc. Using fast scanning technique, the intensity distribution of arc is captured providing information about the arc structure. It can be inferred from this research that during CZ, there are instabilities affecting the electric arc. The radius of the arc is measured from 0.5 to 1mm while the eddies which trigger the instabilities are measured to be 2mm to 4mm. It is concluded that the eddies are formed as result of cold gas mixing with hot plasma. The experiment also shows that at high steady current the effect of turbulence is negligible compared to strong convective energy transfer. Images taken from the arc around CZ in different axial positions show that the turbulent unstable part of the non-axisymmetric arc start close to the nozzle throat. In an investigation on the application of CFD in arc simulation [10], it is pointed out that turbulent structures are 3D according to a superposition of shadowgraph and light emission image. Accordingly, for proper treatment of geometries with 3D arcs as in the case of rotating arc circuit breakers, 3D simulation becomes a necessity. Fang et al. [25] carried out a 2D axisymmetric simulation for SF6 gas-blast arc inside a nozzle during current-zero. The PML turbulence model was adopted for simplicity and the equation constant was obtained by trial and error by matching numerical and experimental results. Generalization of the results to other geometries was recommended “to be done cautiously”.

In 2012, the fluid-plasma interaction in GCBs was investigated using higher order solution [37]. In this 3D simulation a high order LES is implemented by solving an additional transport equation with the dynamic Smagorinsky model. Using this method, the transfer of information between the sub grid and large scale eddies is improved. Another feature of this simulation is high order (5^{th}) spatial discretization by using WENO (weighted essentially-non oscillatory) scheme. This is done since LES is considered very sensitive to the spatial discretization and numerical as well as physical diffusion would occur using low order methods. Despite the detailed investigation provided on the interaction of fluid-plasma, no validation was provided to ensure the accuracy of this simulation.

2.6 Literature Review Conclusion

According to the critical review, certain aspects of arc-flow such as CZ, arc departure from 2D axisymmetric structure and the effect of 3D effects on arc radius and gaseous medium resistance still needs further elaboration.

CZ Investigation: Despite the numerous studies concerning nearly all phases of the GCBs operation, few investigations has been carried out on the parameters which can influence the arc extinction. When the current is at the peak, the arc is relatively stable and most of the energy transfer is done through the convection mechanism. At CZ, the effect of instabilities on critical parameters such as RRRV becomes crucial considering that extinction failure becomes possible at this phase. The role of other source terms such as radiation could also be in question.

3D simulation: Despite a few 3D arc simulations, the literature is dominated by 2D-axisymmetric numerical simulations. The reason is simply the fact that arc can be considered as a cylinder. While this assumption is true for high current (1000A) and steady arcs, 3D effects start to emerge as the current decreases to CZ. That is why 3D simulation is recommended and required for a better understanding of arc physics [10].

High Order Simulation: Almost all of the arc simulations are carried out with low order schemes for spatial discretization, temporal discretization, numerical integration and boundary condition implementation. Higher order solutions give better resolution of the details for complex flow structures compared to a low order simulation on the same grid, because in high order simulations, a wider spectrum of space and time scales are taken into account.

A methodology, as explained in Section 3, is adopted to fulfil these requirements.

CHAPTER 3 Methodology

It has been chosen to carry out the arc simulation inside the Aachen nozzle which was explored experimentally by Leseberg [53]. Sufficient information about the geometry, nozzle total pressure and more importantly measured temperature profile makes the Aachen nozzle an informative case for arc numerical simulation. In addition, other numerical simulations are available for arcs formed in this nozzle [23, 25]. To carry out the simulation, a set of 3D Euler equations are solved where a part of the Aachen nozzle is discretized with a structured Cartesian mesh. This methodology is detailed in the following sections.

3.1 Initialization

For the sake of simplicity this research addresses only the arc and the nozzle walls are not included. This is schematically shown in Fig. 3.1.

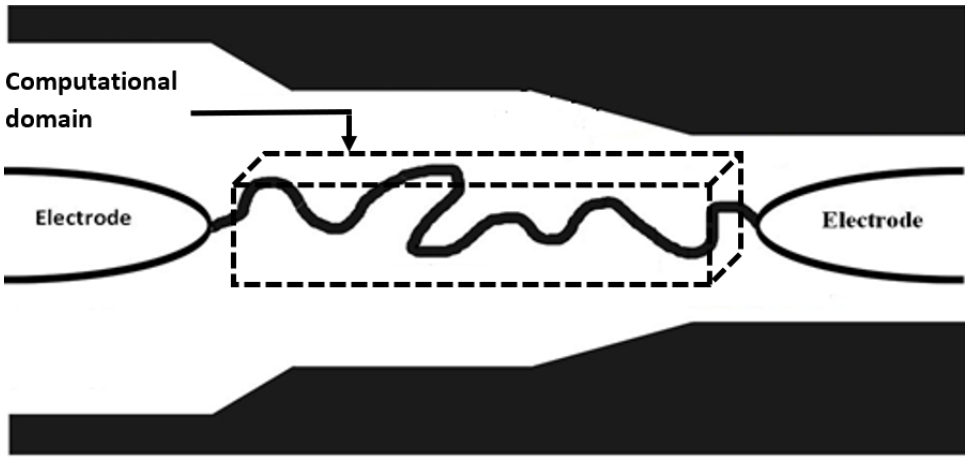

Figure 3.1 Computational domain for the 3D simulation

Such an approach makes the schemes easier to implement while rendering the simulation less computationally expensive. The simplicity of such an approach can be explained as follows:

1. The walls are not considered therefore, ablation equation can be excluded from the simulation.

2. With a smaller computational domain, the grid can be refined on the arc zone which keeps the focus on the arc and provides more information on the arc behaviour.

3. The rectangular computational domain can be discretized to a structured Cartesian mesh. Solving the arc governing equations on a Cartesian mesh is less complicated while being less computationally expensive.

4. The research team is currently working on an extension of the present work to include wall boundaries using an Immersed Boundary Method (IBM). The present methodology paves the way for such a development.

For this methodology to be carried out, the arc is ignited and stabilized using MC^3 and the results are used to initialize the solution in the 3D code as follows:

1. Using MC^3, the arc is ignited in the nozzle between the two electrodes and kept steady at a specified current (1000A in this research).

2. The results are then mapped from the MC^3 2D axisymmetric triangular mesh, to the 3D, structured Cartesian mesh to be used as an initial condition. This is shown in Fig. 3.2.

3. The arc is kept at the specified current (1000A) in the 3D code until the steady state is reached. At this current, the arc is fully axisymmetric.

4. Once steady, the arc is ramped down in the 3D code to CZ.

3.2 SF6 Flow

The SF6 flow is simulated by solving the following system of Euler equations.

$$\frac{\partial U}{\partial t} + \frac{\partial F_x}{\partial x} + \frac{\partial G_y}{\partial y} + \frac{\partial H_z}{\partial z} = S \tag{3.1}$$

with

$$\begin{aligned} U &= (\rho, \rho u, \rho v, \rho w, \rho E_T)^t, \\ F_x &= (\rho u, \rho u^2 + P, \rho uv, \rho uw, (\rho E_T + P)u)^t, \\ G_y &= (\rho v, \rho uv, \rho v^2 + P, \rho vw, (\rho E_T + P)v)^t, \\ H_z &= (\rho w, \rho uw, \rho vw, \rho w^2 + P, (\rho E_T + P)w)^t, \end{aligned} \tag{3.2}$$

where u, v and w are the velocity components, P represents pressure, ρ density and E_T the total energy. The specific internal energy e can be obtained from

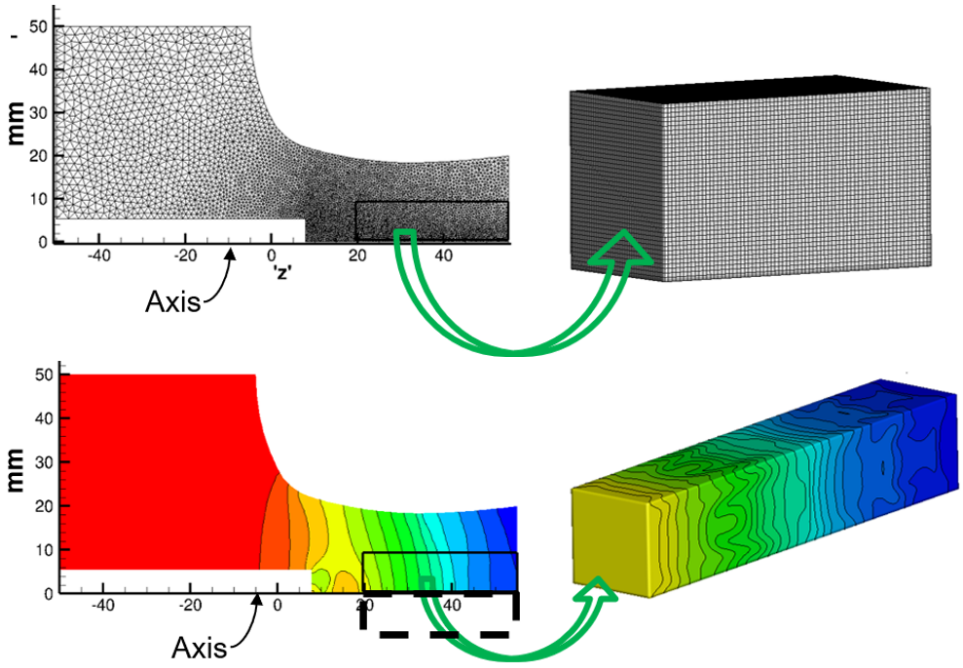

Figure 3.2 Results (pressure contours) from MC^3 (2D) are used as the initial conditions for the 3D code

$$e = E - \frac{1}{2}(u^2 + v^2 + w^2). \tag{3.3}$$

With SF6 being in a real gas state, the system of Eqs. 3.1 cannot be completed by the equation of state $P = \rho RT$. That is why the gas properties (R, e, P, T, ρ) are obtained from tabulated values.

As shown in Fig. 3.1, the computational domain is a cuboid (box) inside the nozzle whose position is chosen to be away from the zone of re-circulation of the flow as shown in Fig. 3.3.

The boundary conditions for the flow comprise one inlet and one outlet. For the other surrounding boundaries, the face is an inlet or an outlet using the following rule

$$B.C. \quad \begin{cases} Inlet & \overrightarrow{V}.\overrightarrow{n} \leq 0 \\ Outlet & \overrightarrow{V}.\overrightarrow{n} \geq 0 \end{cases}$$

where $\overrightarrow{n}$ is the face normal vector.

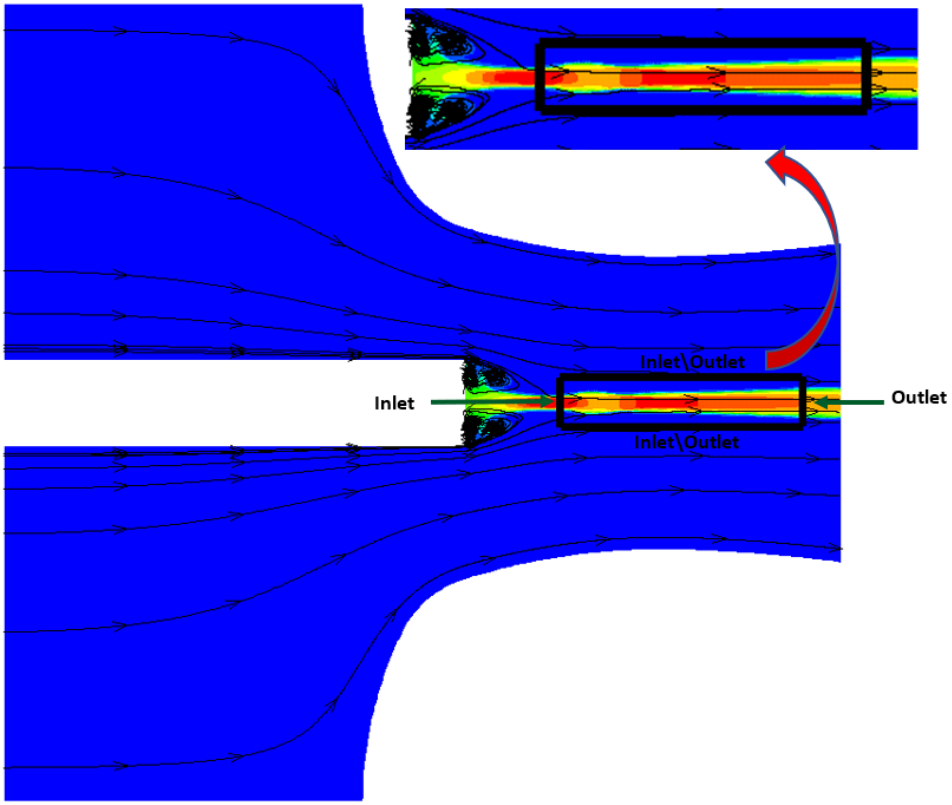

Figure 3.3 The box position and the type of boundary conditions for SF6 flow

Discretizing the equations using a finite volume scheme, it is obtained

$$U_{(i)}^{n+1} = U_{(i)}^{n} - \Delta t\Bigg(\frac{1}{\Delta x_i}[F_{(i+\frac{1}{2},j,k)}^{n} - F_{(i-\frac{1}{2},j,k)}^{n}] - \frac{1}{\Delta y_j}[G_{(i,j+\frac{1}{2},k)}^{n} - G_{(i,j-\frac{1}{2},k)}^{n}] - \frac{1}{\Delta z_k}[H_{(i,j,k+\frac{1}{2})}^{n} - H_{(i,j,k-\frac{1}{2})}^{n}]\Bigg) \tag{3.4}$$

with F, G, H defined in Eq. 3.2.

3.2.1 Roe's Scheme

The fluxes in Eq. 3.4 are calculated using Roe's scheme [39] which has been used extensively in the numerical flux calculation. The objective of Roe's scheme is to solve Eq. 3.1 at the interface of the cells based on the left (U_L) and right (U_R) values as shown in Fig. 3.4.

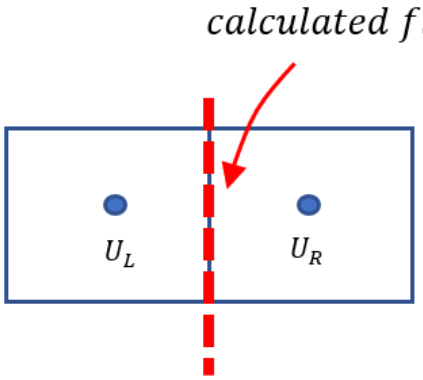

Figure 3.4 Left and right cell values used by Roe's scheme to determine the flux passing the interface

Roe's scheme proposes a Jacobian matrix ($\tilde{\mathcal{A}}$) to map U to F such that (mapping U to G and H follows a symmetry)

$$F_R - F_L = \tilde{\mathcal{A}}(U_R - U_L) \tag{3.5}$$

where

$$\tilde{\mathcal{A}} = \mathcal{A}(\tilde{u}, \tilde{v}, \tilde{w}, \tilde{H}) \tag{3.6}$$

and the Roe average operator defined as

$$\tilde{f}(\Phi) = \frac{\sqrt{\rho_L}\Phi_L + \sqrt{\rho_R}\Phi_R}{\sqrt{\rho_L} + \sqrt{\rho_R}}, \quad \Phi = \tilde{u}, \tilde{v}, \tilde{w}, \tilde{H} \tag{3.7}$$

$$\tilde{\rho} = \sqrt{\rho_L \rho_R}. \tag{3.8}$$

$$\tilde{\mathcal{A}} = \tilde{Q}\tilde{D}\tilde{Q}^{-1}, \tag{3.9}$$

where $\tilde{D} = diag(\lambda_1, \lambda_2, \lambda_3, \lambda_4,)$, with the eigenvalues defined as

$$\lambda_1 = \tilde{V} - \tilde{c}, \quad \lambda_2 = \tilde{V}, \quad \lambda_3 = \tilde{V} + \tilde{c} \quad \lambda_4 = \tilde{V}. \tag{3.10}$$

The corresponding eigenvectors can be then found by

$$
\begin{aligned}
e_1 &= (\tilde{u}-\tilde{c}, \tilde{v}-\tilde{c}, \tilde{w}-\tilde{c}, \tilde{H}-\tilde{V}\tilde{c})^T, && (3.11)\\
e_2 &= (\tilde{u}, \tilde{v}, \tilde{w}, \frac{1}{2}|\tilde{V}^2|)^T, && (3.12)\\
e_3 &= (\tilde{u}+\tilde{c}, \tilde{v}+\tilde{c}, \tilde{w}+\tilde{c}, \tilde{H}+\tilde{V}\tilde{c})^T, && (3.13)\\
e_4 &= (\Delta\tilde{u}-\Delta\tilde{V}, \Delta\tilde{v}-\Delta\tilde{V}, \Delta\tilde{w}-\Delta\tilde{V}, \tilde{u}\Delta u+\tilde{v}\Delta v+\tilde{w}\Delta w-\tilde{V}\Delta V)^T, && (3.14)\\
& && (3.15)
\end{aligned}
$$

with $|\tilde{V}|^2 = \tilde{u}^2+\tilde{v}^2+\tilde{w}^2$ and $c^2 = (\gamma-1)[H-\frac{1}{2}q^2]$ and H the total enthalpy. These eigenvectors have to satisfy the following equation,

$$\Delta U = \sum_{k=1}^{4} \alpha_k \; e_k, \tag{3.16}$$

where the α_k can be found from

$$
\begin{aligned}
\alpha_1 &= \frac{1}{2\tilde{c}^2}(\Delta P - \tilde{\rho}\tilde{c}\Delta V), && (3.17)\\
\alpha_2 &= \Delta\rho - \frac{\Delta P}{\tilde{c}^2}, && (3.18)\\
\alpha_3 &= \frac{1}{2\tilde{c}^2}(\Delta P + \tilde{\rho}\tilde{c}\Delta V), && (3.19)\\
\alpha_4 &= \tilde{\rho}. && (3.20)
\end{aligned}
$$

Finally, the components of the flux vector will be obtained as

$$\Delta F = \sum e_k \; \lambda_k \; \alpha_k. \tag{3.21}$$

As shown in [52], $|\Delta F_3|$ can be computed as follows to account for the real gas effect.

$$
\begin{aligned}
|\Delta F_3| &= (\tilde{H}+\tilde{V}\tilde{c})(|\tilde{V}+\tilde{c}|)(\frac{1}{2\tilde{c}^2}(\Delta P + \tilde{\rho}\tilde{c}\Delta u)) && (3.22)\\
&+ (\tilde{H}-\tilde{V}\tilde{c})(|\tilde{V}-\tilde{c}|)(\frac{1}{2\tilde{c}^2}(\Delta P - \tilde{\rho}\tilde{c}\Delta V)) + |X|
\end{aligned}
$$

where

$$\begin{aligned} X &= (\rho_R V_R H_R) - (\rho_L V_L H_L) \\ &- (\tilde{H} + \tilde{V}\tilde{c})(\tilde{V} + \tilde{c})(\frac{1}{2\tilde{c}^2}(\Delta P + \tilde{\rho}\tilde{c}\Delta V)) \\ &- (\tilde{H} - \tilde{V}\tilde{c})(\tilde{V} - \tilde{c})(\frac{1}{2\tilde{c}^2}(\Delta P - \tilde{\rho}\tilde{c}\Delta V)), \end{aligned} \tag{3.23}$$

and

$$|X| = X \cdot sign(\tilde{V}), \tag{3.24}$$

3.3 Ohmic Source term

To calculate the Ohmic heating, the electric potential are obtained from $\nabla.(\sigma\nabla\phi) = 0$ presented in the following

$$\nabla\sigma\nabla\phi + \sigma\nabla^2 = 0 \tag{3.25}$$

or

$$\sigma_x\phi_x + \sigma_y\phi_y + \sigma_z\phi_z + \sigma(\phi_{xx} + \phi_{yy} + \phi_{zz}) = 0. \tag{3.26}$$

Equation 3.26 is an elliptic PDE with variable coefficients. To solve this equation, a fourth order compact finite difference method [38] is implemented (ϕ is stored on the vertices). This method is capable of keeping the order of accuracy for the wide range of σ appearing in the arc. Easier implementation of Dirichlet boundary conditions is an advantage of compact methods. A 19-points stencil is considered around each vertex as shown in Fig. 3.5. Based on such a discretization the following expression is obtained

$$\sum_{l=0}^{18} c_l\phi_l = F_0 \tag{3.27}$$

where the coefficients $c_0 - c_{18}$ and F_0 are presented in APPENDIX A.

To solve Eq. 3.25, potentials on the anode and the cathode (ϕ_a, ϕ_c) are imposed as shown in Fig. 3.6.

It is noted that at the initial time ϕ_a and ϕ_c are not known when the solution initiates. To solve this problem it is assumed that

$$\phi_a = 1$$

$$\phi_c = 0.$$

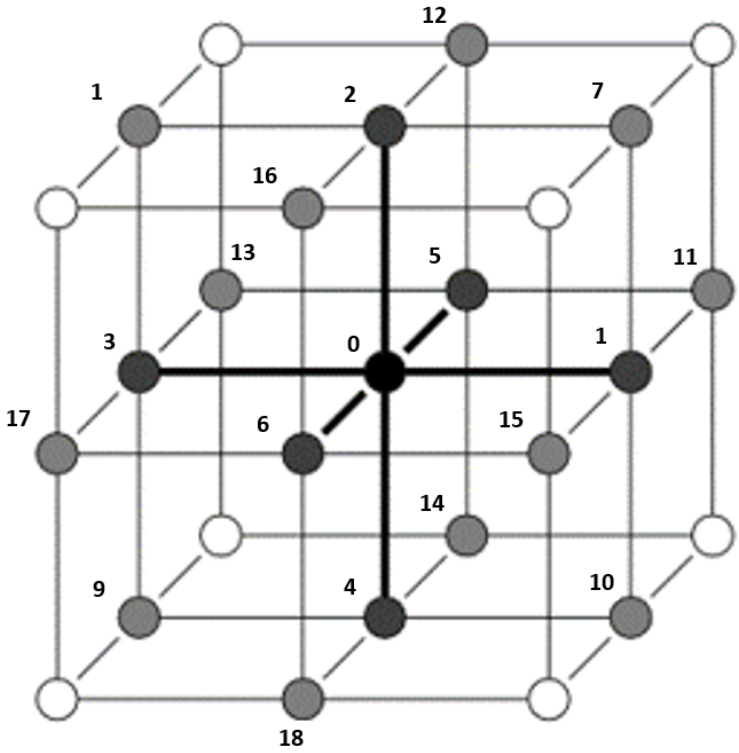

Figure 3.5 19 point stencil for the 4^{th} order compact finite difference method

Considering $e = -\nabla\phi$, the electric field E can be obtained by

$$E = Ve$$

where V is the potential difference between the electrodes and needs to be determined. From the total power relation,

$$IV = \int_{\Omega} \sigma |E|^2 \mathrm{d}v = V^2 \int_{\Omega} \sigma |e|^2 \mathrm{d}v \tag{3.28}$$

From Eq. 3.28, the potential difference is given by

$$V = \frac{I}{\int_{\Omega} \sigma |e|^2 \mathrm{d}v} \tag{3.29}$$

where I is the arc current. Finally, the Ohmic source term can be calculated according the Joule's law

$$S_{ohm} = \sigma(E.E) = \sigma |E|^2 \tag{3.30}$$

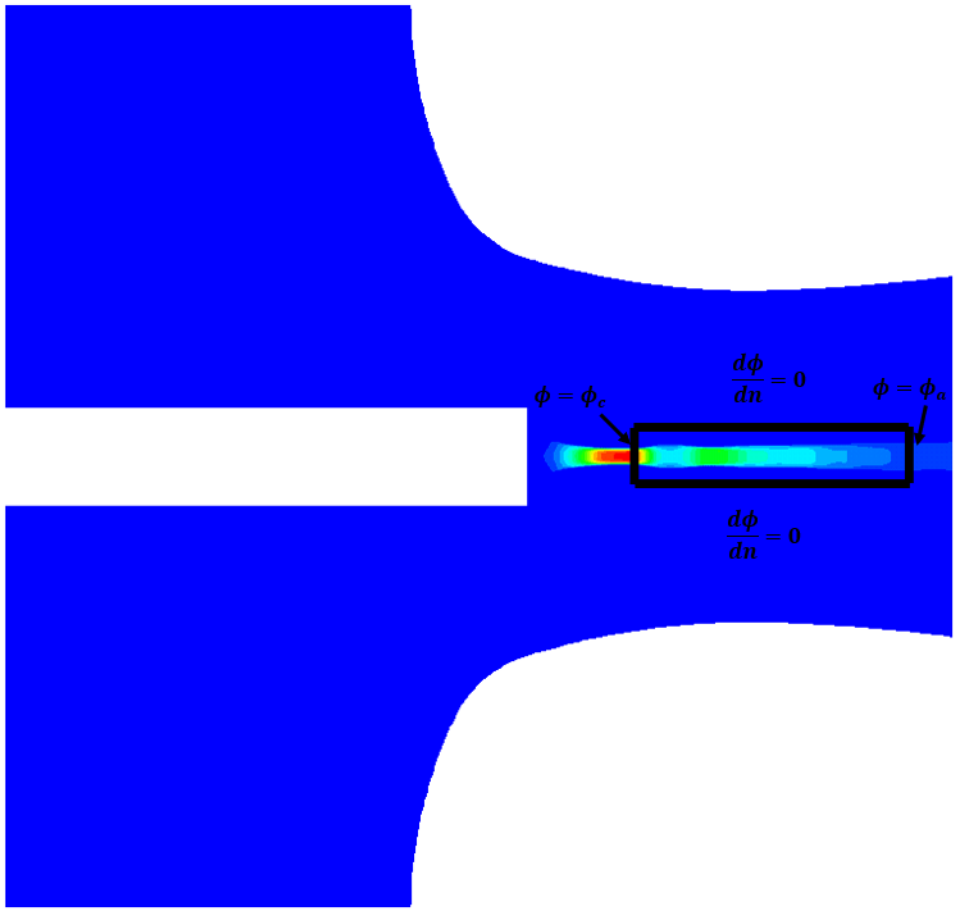

Figure 3.6 Boundary Conditions for calculating the Ohmic source term

3.4 Radiative Source Term

For calculating the radiative source term, the P1 method is used since it has the sufficient accuracy with less computational cost as compared to the DOM. For this reason, Eq. 2.21 (presented again for simplicity) should be solved to obtain the incident radiation for each band (G_v).

$$\nabla.(\frac{1}{K_v}\nabla G_v) = 3K_v(G_v - 4\pi I_{bv}). \tag{3.31}$$

To solve Eq. 2.21, a second order finite difference discretization is implemented. The complex nature of this equation such as the linear term (G_v) and high gradients of absorption coefficients, prevents the higher order compact methods to converge.

Once the incident radiation is obtained, the next step is to calculate the radiative heat transfer

$$S_{Rad} = \sum_{v=1}^{N_{band}} K_v(4\pi I_{v_l} - G_l). \tag{3.32}$$

The box is chosen so that it spans sufficiently far from the arc core. Therefore, zero incident radiation ($G_v = 0$) can be assumed for the boundaries, that lie in the cold flow. For the other boundaries, a Neumann condition is considered as shown in Fig. 3.7.

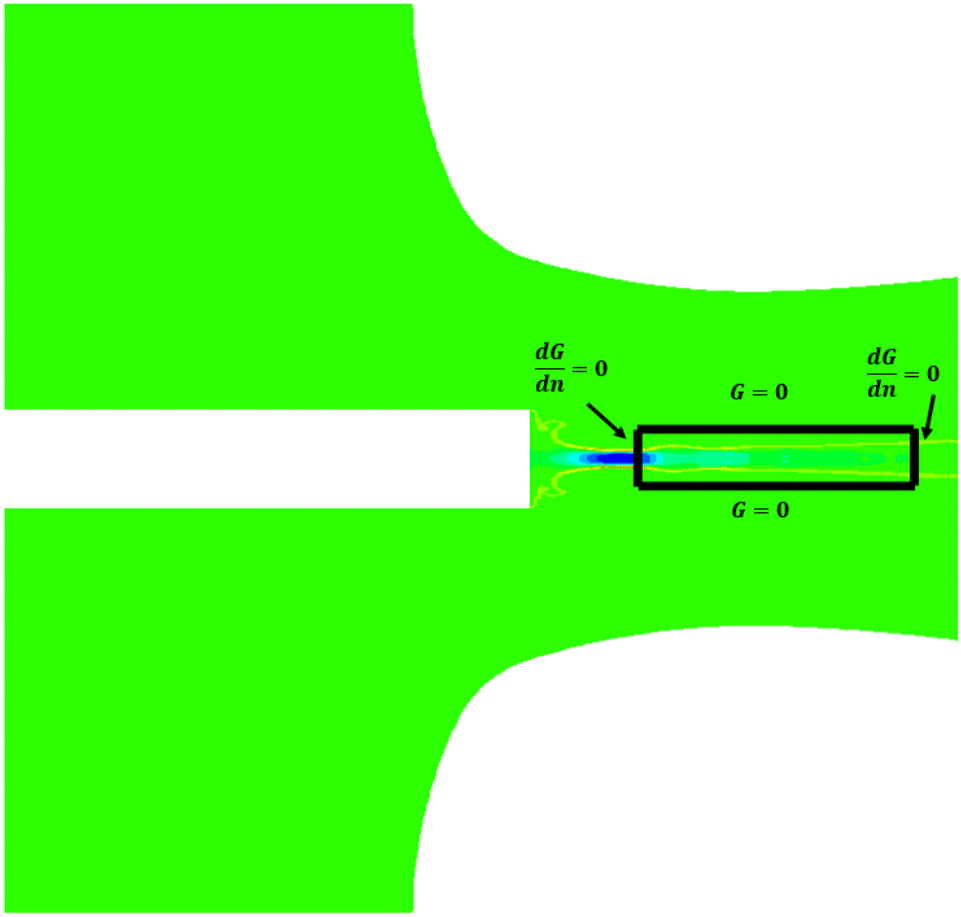

Figure 3.7 Boundary conditions for incident radiation determination

3.5 Linear System of Equation Solver

Solving for radiative and Ohmic energy source terms, a system of linear equations in the form of $Ax = b$ is obtained and should be solved. A is the coefficient matrix which is a very sparse matrix whose elements depend on the gas properties. While different methods are available to solve this system of equations, the choice of solver is very important since it must have the following characteristics:

1. Fast: the solver is applied to large matrices in case of a fine mesh.

2. Stabilized: based on the gas properties the coefficient matrix A contains a disparate range of numbers for calculating Ohmic and radiative source terms. A non-stabilized solver will diverge easily trying to handle such a highly irregular coefficient matrix.

3. Parallelizable: considering a fine mesh the solver should run on multi-core CPUs to avoid a very long computational time.

Iterative linear solvers have certain advantages over direct solvers when it comes to large sparse systems. Though in direct methods the round off error is absent, iterative methods are faster with a controlled order of accuracy. Within the available iterative solvers the Conjugate Gradient (CG) method is more popular due to the fast converging properties compared to Gauss Seidel and Jacobi methods. However it sometimes suffers from irregular convergence problem [40]. This problem is fixed by Stabilized Bi Conjugate Gradient method developed by H. A. van der Vorst [40] . This method is more efficient and converges faster and more smoothly than the other variations of CG method i.e. Biconjugate Gradient method and Conjugate Gradient Squared method. Iterative methods are usually used with pre-conditioners for a faster convergence. Jacobi (diagonal) pre-conditioner has been chosen for this simulation since it is simple to implement and compliant with parallel processing.

3.6 WENO Scheme

In order to increase the fidelity of the simulation, use has been made of WENO. This method is a variation of ENO (Essentially non-Oscillatory) schemes family. It is assumed that complex arc phenomena can be better accounted for when there is a global high order accuracy scheme for the cold flow, the source terms and time integration.

3.6.1 Idea

Traditional high order schemes use fixed stencils. For example for 3^{rd} order of accuracy for cell i, information from the adjacent cells (cell $i-1$ and $i+1$ in case of a central difference) should be also used. The more cells are included in the stencil, the higher the order of accuracy will be. Such traditional methods are necessarily oscillatory near discontinuities. In addition, refined mesh can not eliminate the oscillations.

ENO schemes were introduced by Harten, Engquist, Osher and Chakravarthy [42] for convection dominated, hyperbolic equations. Instead of choosing a fixed stencil, ENO schemes choose different stencils based on the calculated smoothness. These schemes have proved

efficient and accurate when applied to cases in which both discontinuous (shock) and smooth flow structures are present.

The WENO scheme was first presented by Liu, Osher and Chan [43]. They suggested a convex combination of all stencils instead of choosing just one. This was further improved by Jiang and Shu for high order finite difference schemes [44]. They implemented fifth order WENO for several applications including multidimensional calculations. WENO was further investigated for finite volume and finite difference schemes by Shu [41].

The initial WENO schemes were developed for a uniform mesh, and extended to non-uniform mesh [46] and unstructured mesh [47] [48]. WENO has shown to be more efficient, faster and more accurate than ENO schemes for the same stencils [48].

3.6.2 Implementation

The WENO scheme actually solves a reconstruction problem. Given a piecewise smooth function $u(x)$ for cells $I_i = [x_{i-\frac{1}{2}}, x_{i+\frac{1}{2}}]$, the cell average can be defined as

$$\overline{u}_i = \frac{1}{\Delta x_i} \int_{x_{i-\frac{1}{2}}}^{x_{i+\frac{1}{2}}} u(x)\mathrm{d}x. \tag{3.33}$$

With cells sizes Δx_i, an approximation to the function $u(x)$ can be obtained at the desired location e.g. cell boundary $x_{i+\frac{1}{2}}$ as described in Fig. 3.8.

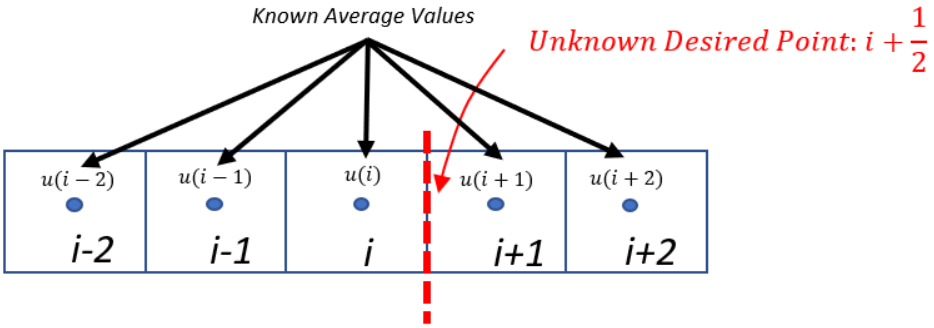

Figure 3.8 Definition of Reconstruction Problem

Considering the stencil comprising $\overline{u}_{i-1}, \overline{u}_i$ and $\overline{u}_{i+1}$ a second order polynomial $p(x)$ can be obtained as follows

$$\frac{1}{\Delta x_{i-1}} \int_{x_{i-\frac{3}{2}}}^{x_{i-\frac{1}{2}}} p(x)\mathrm{d}x = \overline{u}_{i-1} \tag{3.34}$$

$$\frac{1}{\Delta x_i}\int_{x_{i-\frac{1}{2}}}^{x_{i+\frac{1}{2}}} p(x)\mathrm{d}x = \overline{u}_i \tag{3.35}$$

$$\frac{1}{\Delta x_{i+1}}\int_{x_{i+\frac{1}{2}}}^{x_{i+\frac{3}{2}}} p(x)\mathrm{d}x = \overline{u}_{i+1} \tag{3.36}$$

The polynomial $p(x)$ does not need to be determined but its value at the desired point $x_{i+\frac{1}{2}}$ is of interest which yields

$$U_{i+\frac{1}{2}} = p(x_{i+\frac{1}{2}}) = -\frac{1}{6}\overline{u}_{i-1} + \frac{5}{6}\overline{u}_i + \frac{1}{3}\overline{u}_{i+1}. \tag{3.37}$$

Equation 3.37 is a third order approximation of $p(x)$ evaluated at $x_{i+\frac{1}{2}}$. Referring to Fig. 3.8, three stencils are conceivable for the five neighbour cells as shown in Fig. 3.9.

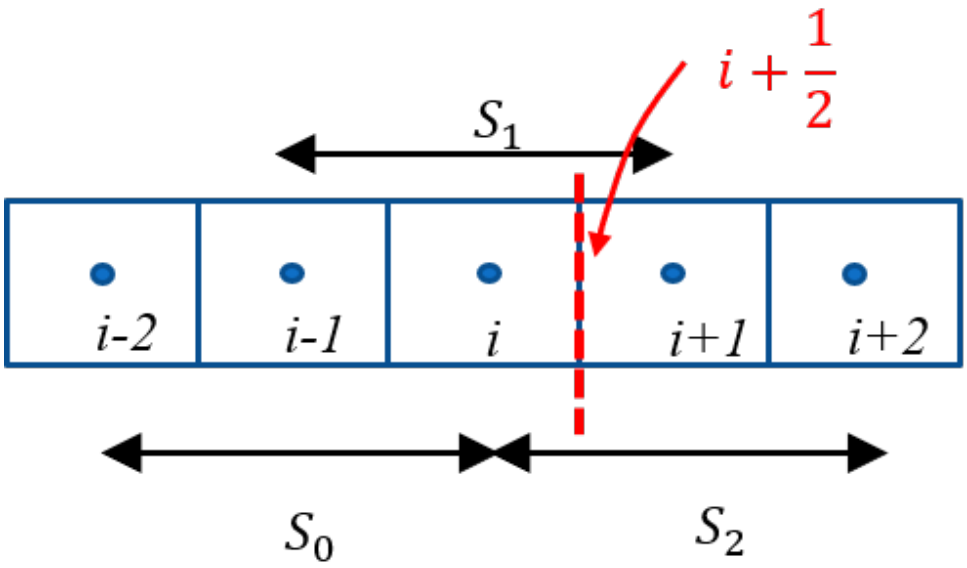

Figure 3.9 Three different stencils within the big (5 cells) stencil

Following the same procedure, the value at $x_{i+\frac{1}{2}}$ can be approximated according to each stencil (S_0, S_1 and S_2) given by the following expressions,

$$U^0_{i+\frac{1}{2}} = \frac{1}{3}\overline{u}_{i-2} - \frac{7}{6}\overline{u}_{i-1} + \frac{11}{6}\overline{u}_i, \tag{3.38}$$

$$U^1_{i+\frac{1}{2}} = -\frac{1}{6}\overline{u}_{i-1} + \frac{5}{6}\overline{u}_i + \frac{1}{3}\overline{u}_{i+1}, \tag{3.39}$$

$$U^2_{i+\frac{1}{2}} = \frac{1}{3}\overline{u}_i + \frac{5}{6}\overline{u}_{i+1} - \frac{1}{6}\overline{u}_{i+2}. \tag{3.40}$$

A combination of $U^{S=0,1,2}_{i+\frac{1}{2}}$ evaluated for different stencils will still be a third order accurate approximation

$$U_{i+\frac{1}{2}} = \gamma_0 U^0_{i+\frac{1}{2}} + \gamma_1 U^1_{i+\frac{1}{2}} + \gamma_2 U^2_{i+\frac{1}{2}} \tag{3.41}$$

As shown in [41], if $p(x)$ is smooth in all candidate stencils the coefficients $\gamma_0, \gamma_1, \gamma_2$ can be obtained from

$$\sum_{r=0}^{2} \gamma_r U^{(r)}_{i+\frac{1}{2}} = U_{i+\frac{1}{2}} \tag{3.42}$$

such that the obtained $U_{i+\frac{1}{2}}$ from Eq. 3.41 is fifth order accurate. Solving Eq. 3.42, $\gamma_0, \gamma_1, \gamma_2$ can be obtained as,

$$\gamma_0 = \frac{1}{10}, \gamma_1 = \frac{3}{5}, \gamma_2 = \frac{3}{10} \tag{3.43}$$

As mentioned, the obtained linear weights are obtained with the assumption of $p(x)$ being smooth. Thus, if there is a discontinuity in one of the stencils, the approximation will be oscillatory. To overcome this problem, instead of using linear weight, non-linear weights $\omega_{k=0,1,2}$ are introduced. These weights vary between $\gamma_{k=0,1,2}$ and 0 depending on the smoothness of $p(x)$. To evaluate the non-linear weights, the smoothness of $p(x)$ should be somehow calculated. It is measured by minimizing the total variation of the reconstruction polynomial inside the cells [41]. The smoothness indicator is thus given by,

$$\beta_{k=0,1,2} = \Delta x_i \int_{x_{i-\frac{1}{2}}}^{x_{i+\frac{1}{2}}} p'(x)^2 \mathrm{d}x + \Delta x_i^3 \int_{x_{i-\frac{1}{2}}}^{x_{i+\frac{1}{2}}} p''(x)^2 \mathrm{d}x \tag{3.44}$$

Equation 3.44 results in the following smoothness indicators,

$$\begin{aligned}
\beta_0 &= \frac{13}{12}(\overline{u}_{i-2} - 2\overline{u}_{i-1} + \overline{u}_i)^2 + \frac{1}{4}(\overline{u}_{i-2} - 4\overline{u}_{i-1} + 3\overline{u}_i)^2 \\
\beta_1 &= \frac{13}{12}(\overline{u}_{i-1} - 2\overline{u}_{i+1} + \overline{u}_i)^2 + \frac{1}{4}(\overline{u}_{i-1} - \overline{u}_{i+1})^2 \\
\beta_2 &= \frac{13}{12}(\overline{u}_i - 2\overline{u}_{i+1} + \overline{u}_{i+2})^2 + \frac{1}{4}(3\overline{u}_i - 4\overline{u}_{i+1} + \overline{u}_{i+1})^2
\end{aligned} \tag{3.45}$$

Finally, the non-linear weights can be obtained from,

$$\omega_k = \frac{\tilde{\omega_k}}{\tilde{\omega_0} + \tilde{\omega_1} + \tilde{\omega_2}} \tag{3.46}$$

where

$$\tilde{\omega_k} = \frac{\gamma_k}{(\varepsilon + \beta_k)^2} \tag{3.47}$$

ε is considered to avoid division by zero and is usually given the value of 10^{-6}. For the flux calculation using Roe scheme, the variables should be interpolated for both the left and the right of each face ($flux = f(U^L_{i+\frac{1}{2}}, U^R_{i+\frac{1}{2}})$). As shown in Fig.3.10, it is decided to calculate $U^L_{i+\frac{1}{2}}$ with more attention to left cells and $U^R_{i+\frac{1}{2}}$ with more focus on right cells.

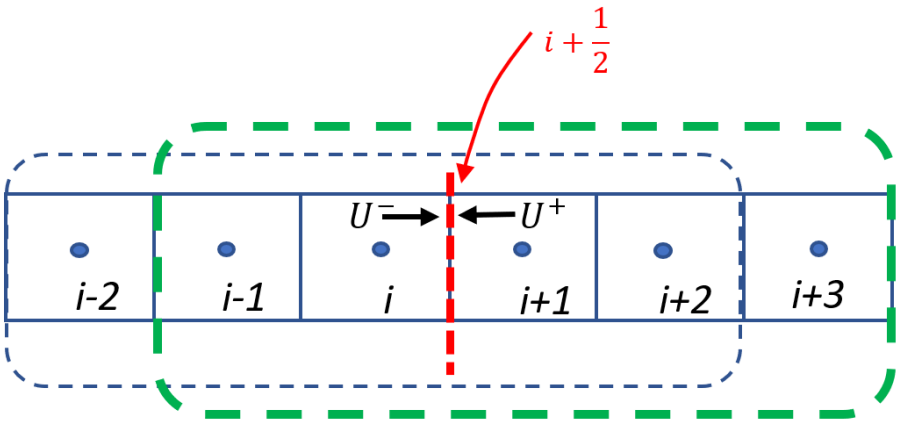

Figure 3.10 Choice of the five cell stencil for calculating $U^L_{i+\frac{1}{2}}$ and $U^R_{i+\frac{1}{2}}$

3.6.3 Extension to multi-dimensions

So far, a 1D stencil using WENO scheme has been presented. In case of finite volume schemes, the extension of WENO to 2D or 3D requires a high order integration on the faces to deal with non-linearity of the equations. This is elaborated for a 2D conservation equation as shown in Eq. 3.48,

$$u_t = f(u)_x + g(u)_y \tag{3.48}$$

For a 2D finite volume scheme, integration over x and y directions ($[x_{i-\frac{1}{2}}, x_{i+\frac{1}{2}}] \times [y_{j-\frac{1}{2}}, y_{j+\frac{1}{2}}]$)

gives

$$\begin{aligned}\frac{d\tilde{\overline{u}}_{ij}(t)}{dt} = &-\frac{1}{\Delta x_i \Delta y_j}\Bigg(\int_{y_{j-\frac{1}{2}}}^{y_{j+\frac{1}{2}}} f(u(x_{i+\frac{1}{2}}, y, t))\mathrm{d}y \\ &- \int_{y_{j-\frac{1}{2}}}^{y_{j+\frac{1}{2}}} f(u(x_{i-\frac{1}{2}}, y, t))\mathrm{d}y \\ &+ \int_{x_{i-\frac{1}{2}}}^{x_{i+\frac{1}{2}}} g(u(x, y_{j+\frac{1}{2}}, t))\mathrm{d}x \\ &- \int_{x_{i-\frac{1}{2}}}^{x_{i+\frac{1}{2}}} g(u(x, y_{j-\frac{1}{2}}, t))\mathrm{d}x\Bigg)\end{aligned} \tag{3.49}$$

where $\tilde{\overline{u}}$ is the cell average

$$d\tilde{\overline{u}}_{ij}(t) = -\frac{1}{\Delta x_i \Delta y_j}\int_{y_{j-\frac{1}{2}}}^{y_{j+\frac{1}{2}}}\int_{x_{i-\frac{1}{2}}}^{x_{i+\frac{1}{2}}} f(u(x, y, t))\mathrm{d}x\mathrm{d}y \tag{3.50}$$

$\overline{u}$ is the average in the x-direction

$$\overline{u}_{ij}(t) = -\frac{1}{\Delta x_i}\int_{x_{i-\frac{1}{2}}}^{x_{i+\frac{1}{2}}} u(x, y_j)\mathrm{d}x, \tag{3.51}$$

and $\tilde{u}$ is the average in the y-direction

$$\tilde{u}_{ij}(t) = -\frac{1}{\Delta y_j}\int_{y_{j-\frac{1}{2}}}^{y_{j+\frac{1}{2}}} u(x_i, y)\mathrm{d}y. \tag{3.52}$$

approximating Eq. 3.49 with a finite volume scheme it is obtained

$$\frac{d\tilde{\overline{u}}_{ij}(t)}{dt} = -\frac{1}{\Delta x_i}(\hat{f}_{i+\frac{1}{2},j} - \hat{f}_{i-\frac{1}{2},j}) - \frac{1}{\Delta y_j}(\hat{g}_{i,j+\frac{1}{2}} - \hat{g}_{i,j-\frac{1}{2}}) \tag{3.53}$$

with the fluxes defined as

$$\begin{aligned}\hat{f}_{i+\frac{1}{2},j} &= -\frac{1}{\Delta y_j}\int_{y_{j-\frac{1}{2}}}^{y_{j+\frac{1}{2}}} f(u(x_{i+\frac{1}{2}}, y, t))\mathrm{d}y \\ \hat{g}_{i,j+\frac{1}{2}} &= -\frac{1}{\Delta x_i}\int_{x_{i-\frac{1}{2}}}^{x_{i+\frac{1}{2}}} g(u(x, y_{i+\frac{1}{2}}, t))\mathrm{d}x\end{aligned} \tag{3.54}$$

if f and g are linear functions, to find $\tilde{\overline{u}}$, it will be sufficient to perform one interpolation on

y-direction and interpolate the result in x-direction. But f and g are non-linear so

$$f(\tilde{u}) \neq \widetilde{f(u)} \tag{3.55}$$

This will be more clear with an example: assuming that the non-linear function is $f(u) = \sqrt{u}$, averaging u and taking the root is not equal to taking the root of u and then taking the average. To solve the problem of non-linearity, an integral on Gaussian quadrature points, with sufficient order of accuracy, is needed. For the current research 2 quadrature points in each direction (4 on face) is used. Fig. 3.11 shows the Gaussian quadrature points on faces of a cell.

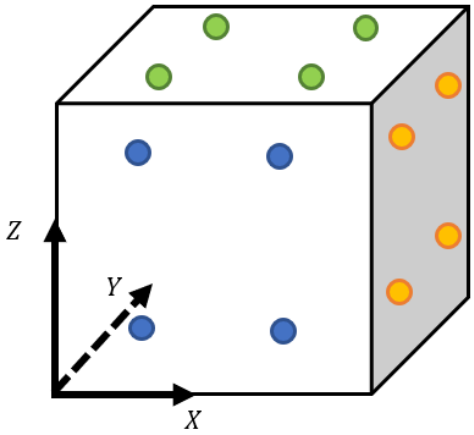

Figure 3.11 Gaussian quadrature points for faces on a cell

To perform this integration, the interpolation scheme has to be adapted to Gaussian quadrature points. In this research, the work of Titarev and Toro [49] is followed where they proposed Gaussian points $\xi_i \pm \frac{\Delta\xi}{2\sqrt{3}}$ on each direction. For the Gaussian point $\xi_i - \frac{\Delta\xi}{2\sqrt{3}}$ the linear weights are

$$\gamma_0 = \frac{210 - \sqrt{3}}{1080}, \gamma_1 = \frac{11}{18}, \gamma_2 = \frac{210 + \sqrt{3}}{1080} \tag{3.56}$$

and the approximation function evaluated at the Gaussian point is obtained from

$$\begin{aligned} u(\xi_i - \frac{\Delta\xi}{2\sqrt{3}}) = \omega_0 \left[u_i + (3u_i - 4u_{i+1} + u_{i+2}) \frac{\sqrt{3}}{12} \right] + \omega_1 \left[u_i - (-u_{i-1} + u_{i+1}) \frac{\sqrt{3}}{12} \right] \\ + \omega_2 \left[u_i - (3u_i - 4u_{i-1} + u_{i-2}) \frac{\sqrt{3}}{12} \right] \end{aligned} \tag{3.57}$$

For the Gaussian point $\xi_i + \frac{\Delta\xi}{2\sqrt{3}}$ the linear weights are

$$\gamma_0 = \frac{210+\sqrt{3}}{1080}, \gamma_1 = \frac{11}{18}, \gamma_2 = \frac{210-\sqrt{3}}{1080} \tag{3.58}$$

and the approximation function evaluated at the Gaussian point is obtained from

$$\begin{aligned} u(\xi_i - \frac{\Delta\xi}{2\sqrt{3}}) = \omega_0 \left[u_i - (3u_i - 4u_{i+1} + u_{i+2}) \frac{\sqrt{3}}{12} \right] + \omega_1 \left[u_i - (u_{i-1} - u_{i+1}) \frac{\sqrt{3}}{12} \right] \\ + \omega_2 \left[u_i - (-3u_i + 4u_{i-1} - u_{i-2}) \frac{\sqrt{3}}{12} \right] \end{aligned} \tag{3.59}$$

3.7 Temporal Integration

Discretization in time has to be of sufficient order of accuracy to be in accordance with spatial discretization. For the high order simulation of an arc, a 3^{rd} order TVD (Total Variation Diminishing) Runge-Kutta time integration scheme has been used (Eqn. 3.60) [51].

$$\begin{aligned} \overline{u}^1 &= \overline{u}^n + \Delta t L(\overline{u}^n) \\ \overline{u}^2 &= \frac{3}{4}\overline{u}^n + \frac{1}{4}\overline{u}^1 + \frac{1}{4}\Delta t L(\overline{u}^1) \\ \overline{u}^{n+1} &= \frac{1}{3}\overline{u}^n + \frac{2}{3}\overline{u}^2 + \frac{2}{3}\Delta t L(\overline{u}^2) \end{aligned} \tag{3.60}$$

where L is the finite volume scheme operator and Δt is the time step.

CHAPTER 4 Verification

This chapter is dedicated to the test cases which help different components of the arc simulation to be verified. There are different methods used to verify the numerical simulations of this research

- Comparison with analytical solutions
- Comparison with numerical solutions
- Method of Manufactured Solutions (MMS)
- Comparison with experiments

It is very important to verify all the different components of the solver before the validation, where the complete simulation is tested with all components in place and compared to experimental results. The 3D arc simulation code comprises the following subroutines which have been verified using different test cases presented in Table 4.1.

Table 4.1 Test cases for 3D arc simulation verification

Test case	**Equation verified**	**Gas type**
Shock tube	1D unsteady Euler equations	Perfect gas-air
Rayleigh flow	1D steady Euler equations + heat transfer	Perfect gas-air
Manufactured solution inside a cube	Ohmic source term (Helmholtz)	NA
Comparison of analytical-numerical solutions for P1 model	Radiative energy source term	NA
Shock tube	1D WENO scheme	Perfect gas-air
3D explosion	3D WENO scheme	Perfect gas-air
Steady arc	All equations	Real gas-SF6
Isothermal cylindrical arc	Radiative energy source term	NA

4.1 Shocktube

A shocktube test includes a box (tube) in which a diaphragm separates a high pressure from a low pressure region. At $t = 0\ s$, the diaphragm is removed which causes an expansion wave to move towards high pressure region and a shock wave to move towards the low pressure region as depicted in Fig. 4.1.

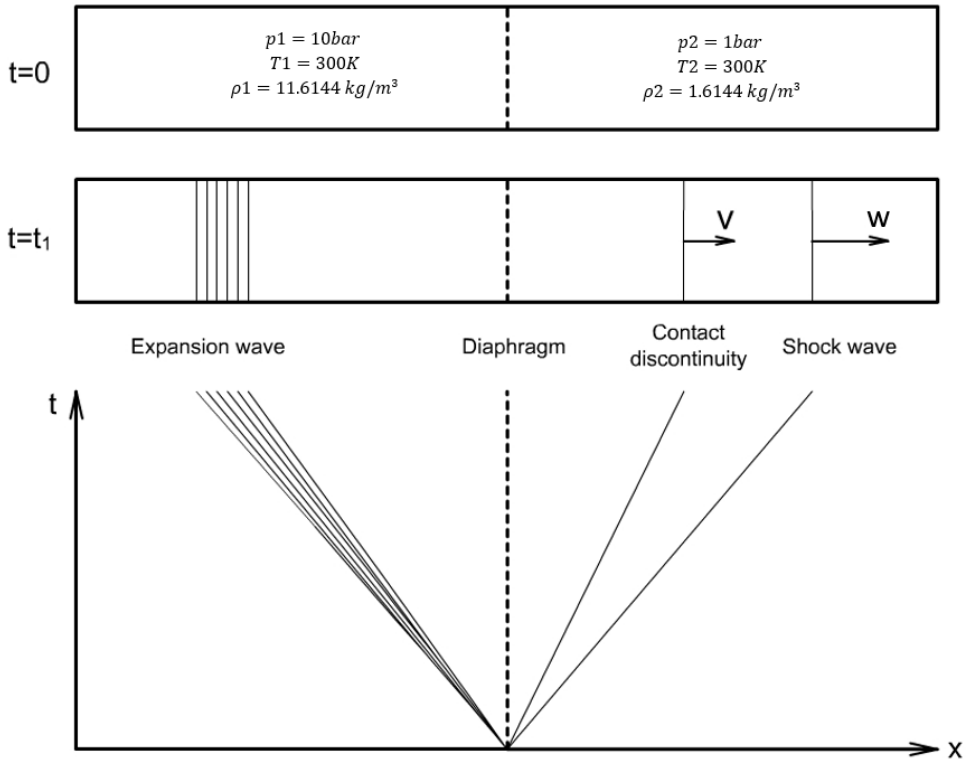

Figure 4.1 Shocktube problem

The availability of analytical solution for the shocktube makes it a popular test case for unsteady Euler equations. Fig. 4.2 shows the comparison of the density curves obtained from the numerical (101 points, CFL=0.5, t=0.007 s) and the exact solution. The importance of choosing the density curve are the gradients existing for both shock wave and contact regions.

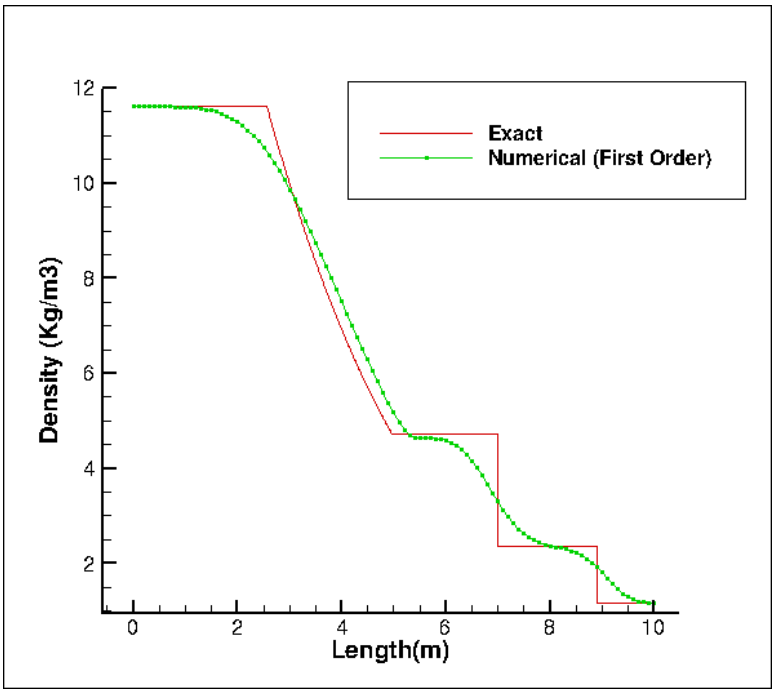

Figure 4.2 Shocktube density curves compared for the numerical (101 points, CFL=0.5) and the exact solution

As an inherent characteristic of a first order (as shown in Fig. 4.3) discretization, it is confirmed that a first order numerical solution yields diffusive results near the shock wave and the contact region. A discrepancy is also detectable for the expansion area. Being a 1D problem, the shocktube test has been repeated for x, y and z directions which led to the same results.

It can be concluded that although the numerical solution follows the exact solution trend, a first order solution is not suitable for an accurate prediction of the shock wave, the contact region and the expansion region. The solution can be enhanced using a finer mesh or a higher order discretization.

It will be shown in Section 4.3.2 that how the 5^{th} WENO improves the numerical solution of shocktube in the expansion region while providing a better capability of predicting the shock wave and the contact region.

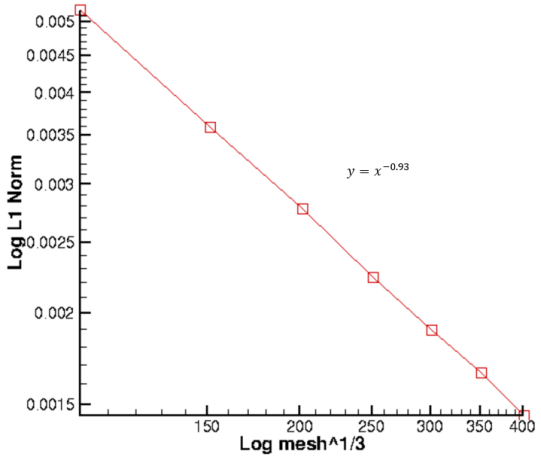

Figure 4.3 Shocktube grid refinement study

4.2 Rayleigh Flow

Rayleigh flow considers a frictionless flow in a constant area duct with heat transfer as presented schematically in Fig. 4.4. This test case is suitable for steady, inviscid subsonic and supersonic flows. Having a source term involved, this case becomes an efficient verification for 3D arc simulation.

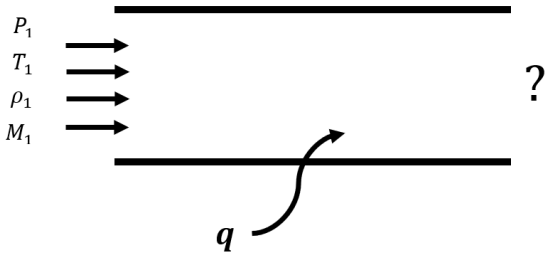

Figure 4.4 Definition of the Rayleigh flow problem

The properties of the gas can be found analytically via the following relations

$$\frac{T_{02}}{T_{01}} = 1 + \frac{q}{C_P T_{01}}, \tag{4.1}$$

$$\frac{P_2}{P_1} = \frac{1 + \gamma M_1^2}{1 + \gamma M_2^2}, \tag{4.2}$$

$$\frac{\rho_2}{\rho_1} = \left(\frac{1+\gamma M_2^2}{1+\gamma M_1^2}\right)\left(\frac{M_1}{M_2}\right)^2, \tag{4.3}$$

$$\frac{T_2}{T_1} = \left(\frac{1+\gamma M_1^2}{1+\gamma M_2^2}\right)^2\left(\frac{M_2}{M_1}\right)^2, \tag{4.4}$$

$$\frac{T_{02}}{T_{01}} = \left(\frac{T_2}{T_1}\right)^2\left(\frac{1+\frac{\gamma-1}{2}M_2^2}{1+\frac{\gamma-1}{2}M_1^2}\right), \tag{4.5}$$

and

$$\frac{P_{02}}{P_{01}} = \frac{P_2}{P_1}\left(\frac{1+\frac{\gamma-1}{2}M_2^2}{1+\frac{\gamma-1}{2}M_1^2}\right)^{\frac{\gamma}{\gamma-1}} \tag{4.6}$$

where T_0 denotes the total temperature, P_0 the total pressure, ρ density, M Mach number, C_P the specific heat capacity, γ the specific heat ratio and q the added heat per unit mass (J/Kg).

To solve this problem, air is assumed to flow in a channel with known stagnation properties. Heat is added to the channel at the rate of 11758000 $Watt/m^3$ as shown in Fig. 4.5.

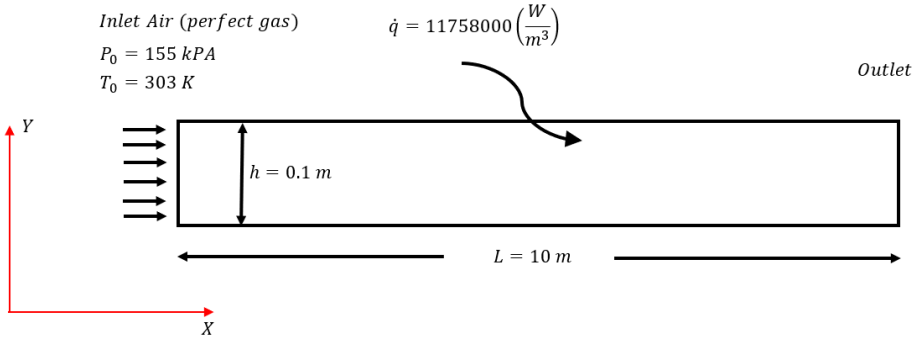

Figure 4.5 Rayleigh flow test case

The numerical and exact results are compared for pressure, temperature and the Mach number values in Fig. 4.6.

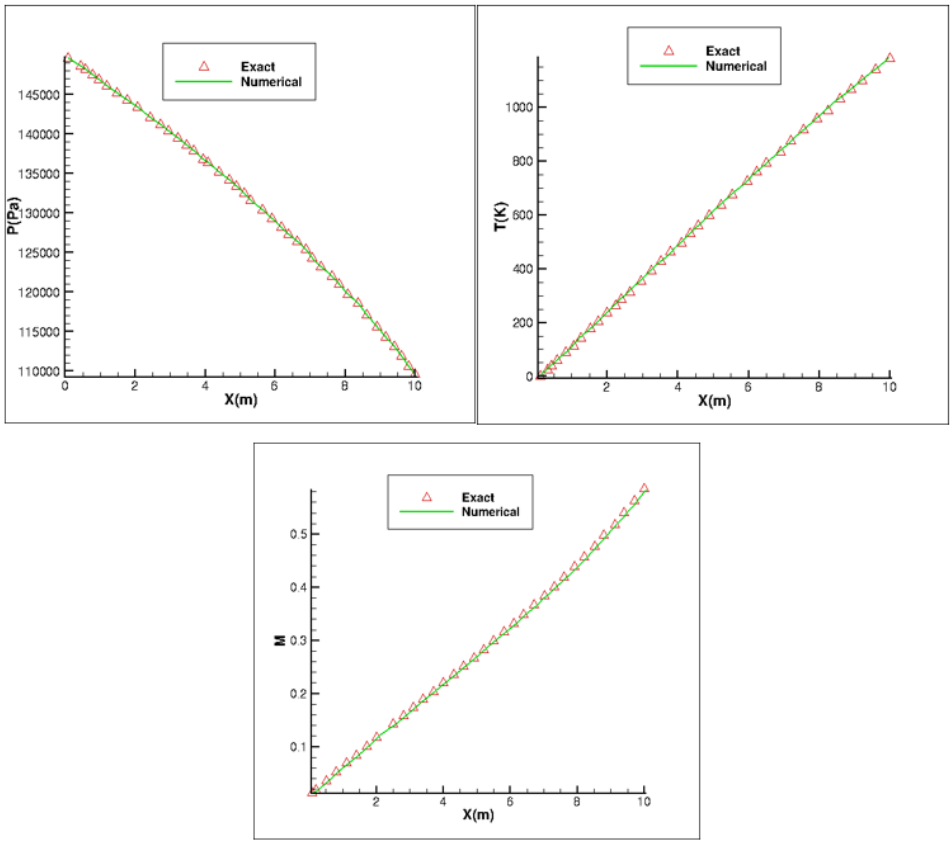

Figure 4.6 Analytical and numerical outlet results compared for a channel with $T_0 = 303K$, $P_0 = 155kPA$ and a fixed heat rate of 11758 KW/m^3

As shown in Fig.4.6, the numerical and the exact solutions are in a good agreement.

In the next step, the Rayleigh flow test case is repeated with a variable source term. The heat rate is a function of the channel length to make the test case more sophisticated

$$q(x) = 5000(x + 1). \tag{4.7}$$

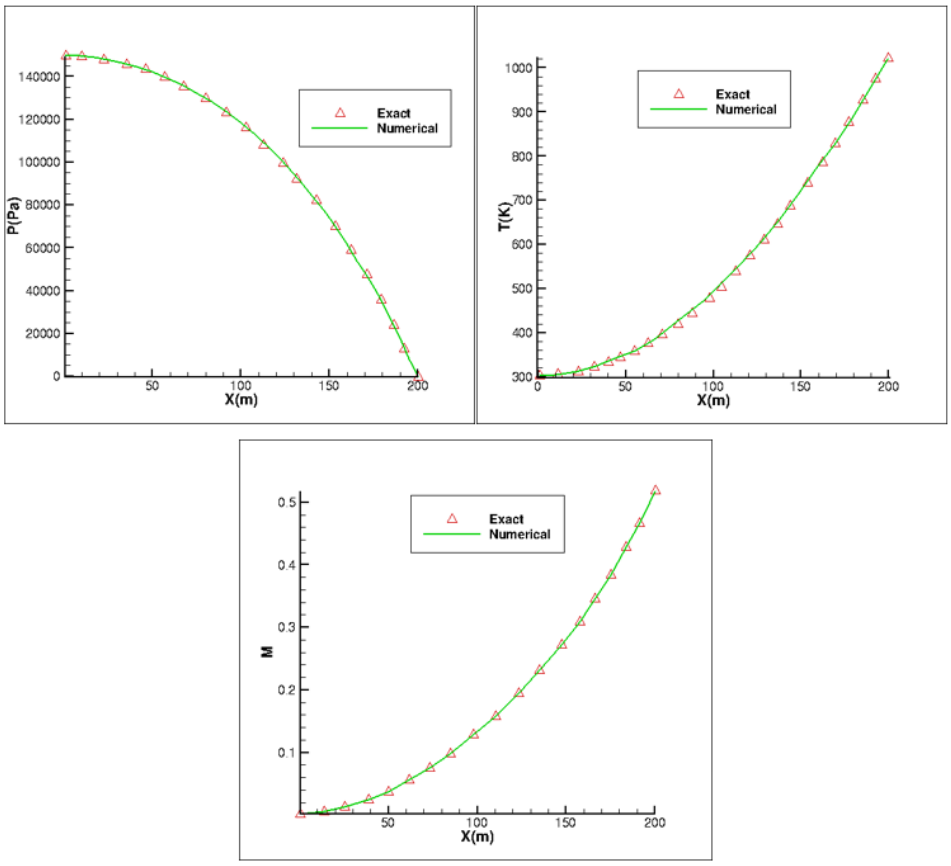

Figure 4.7 Analytical and numerical outlet results compared for a channel with $T_0 = 303K$, $P_0 = 155kPA$ and a heat rate dependant on the longitudinal position of the channel ($5(x+1)$ KW/m^3)

Fig. 4.7 shows quite good agreement between the exact and the numerical results.

4.3 Ohmic Source Term solver

To verify the 4^{th} order compact finite difference method used to calculate the Ohmic source term, the method is used to solve Eqn. 3.25 presented again here for convenience.

$$\nabla\sigma\nabla\phi + \sigma\nabla^2 = 0 \tag{4.8}$$

or

$$\sigma_x\phi_x + \sigma_y\phi_y + \sigma_z\phi_z + \sigma(\phi_{xx} + \phi_{yy} + \phi_{zz}) = 0. \tag{4.9}$$

The analytical form of the manufactured solution is considered to be

$$\hat{\phi}(x,y,z) = sin(\pi x)cos(\pi y)cos(\pi z). \tag{4.10}$$

Substituting Eqn. 4.10 in to Eqn. 4.9 and assuming $\hat{\sigma}(x,y,z) = x + y + z$ gives

$$\hat{\sigma_x}\hat{\phi_x} + \hat{\sigma_y}\hat{\phi_y} + \hat{\sigma_z}\hat{\phi_z} + \hat{\sigma}(\hat{\phi_{xx}} + \hat{\phi_{yy}} + \hat{\phi_{zz}}) = S. \tag{4.11}$$

where S, the analytical source term is given by

$$\begin{aligned} S = (1+y+z)\pi cos(\pi x)cos(\pi y)cos(\pi z) - (1+x+z)\pi sin(\pi x)sin(\pi y)cos(\pi z) \\ -(1+x+y)\pi sin(\pi x)cos(\pi y)sin(\pi z) - (x+y+z)3\pi^2 sin(\pi x)cos(\pi y)cos(\pi z) \end{aligned} \tag{4.12}$$

Eqn. 4.11 is solved inside a cube (dimensions of 1m, shown in Fig. 4.8) with the following boundary conditions

$$\begin{aligned} &\hat{\phi}(x=0) = \hat{\phi}(x=1) = 0 \\ &\hat{\phi}_{y=0} = \hat{\phi}_{y=1} = 0 \\ &\hat{\phi}_{z=0} = \hat{\phi}_{z=1} = 0 \end{aligned} \tag{4.13}$$

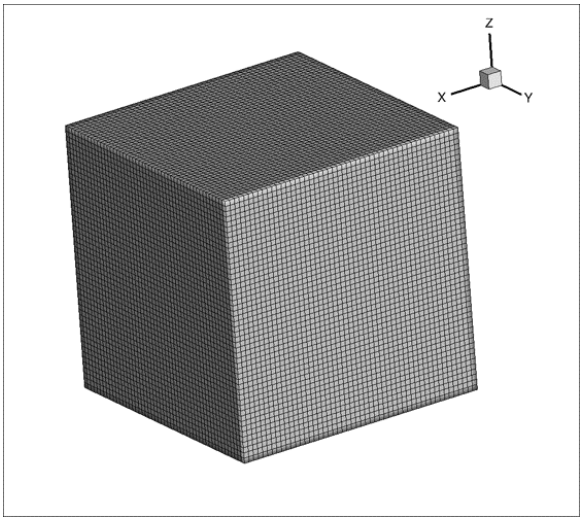

Figure 4.8 Computational domain for the 4^{th} order compact finite difference method

The system of equations were solved with the BiCGSTAB (Bi Conjugate Gradient Stabilized) method and with a convergence tolerance of $\varepsilon < 10^{-6}$. The solution was repeated 6 times with the mesh refined at each level. The order of the accuracy can be found by plotting the error in a *loglog* format as shown in Fig. 4.10.

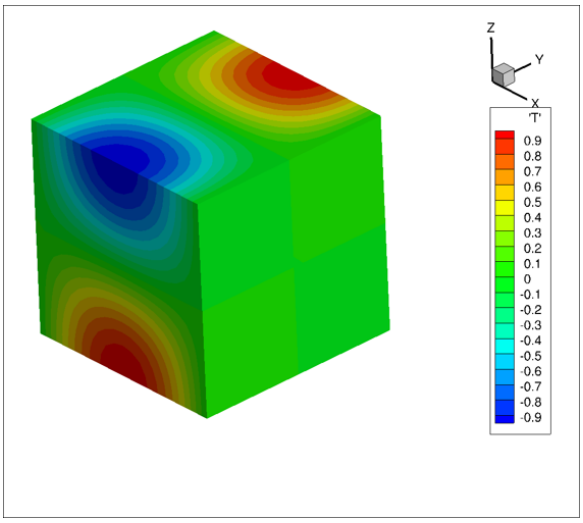

Figure 4.9 Solution of Eqn. 4.11 with the $\hat{\phi}(x=0) = \hat{\phi}(x=1) = 0$, $\hat{\phi}_{y=0} = \hat{\phi}_{y=1} = 0$, $\hat{\phi}_{z=0} = \hat{\phi}_{z=1} = 0$

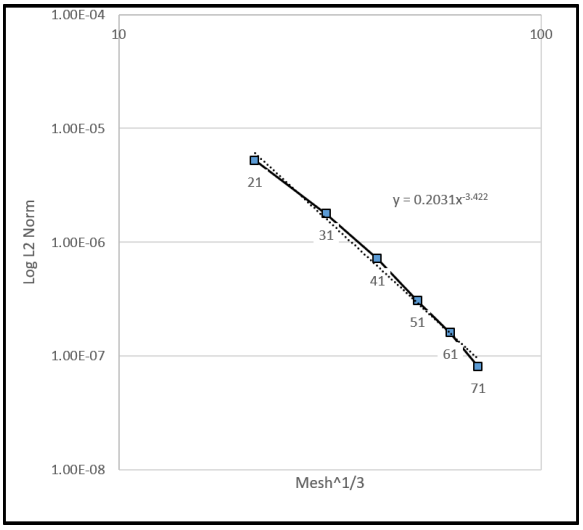

Figure 4.10 Order of accuracy calculation for the 4^{th} order compact finite difference method

The error was calculated via the L_2 norm

$$L_2 = \frac{1}{N}\sqrt{\sum_{j=1}^{N}(u_j^{numerical} - u_j^{exact})^2} \tag{4.14}$$

As shown in Fig. 4.10, the calculated order of accuracy is 3.422.

4.3.1 P1 Model Solver

Since the P1 model has more complex equations compared to the Ohmic source term equation, two different verifications are are presented

1. Comparison to an analytical solution
2. Comparison to numerical results

Comparison to an analytical solution

In the second step of the radiative energy solver verification, Eqn. 3.31 is simplified to yield an ODE with a exact solution.

If the total absorption coefficient is considered as a constant, for one dimension, Eqn. 3.31 reduces to (the subscript v is removed for a better demonstration)

$$\nabla.(\frac{1}{K_v}\nabla G_v) = 3K_v(G_v - 4\pi I_{bv}) \implies \frac{1}{K}G_{xx} = 3KG - 12K\pi I_b \tag{4.15}$$

or

$$\frac{1}{K}G_{xx} - 3KG = S. \tag{4.16}$$

where $S = -12K\pi I_b$ can be treated as a source term. The Eqn. 4.16 is solved in the same box introduced in Fig. 4.9 with four Neumann and two Dirichlet boundary conditions expressed as follows

$$\begin{aligned} &G_x(x=0) = G_x(x=L) = 0 \\ &G_y(y=0) = G_y(y=L) = 0 \\ &G(z=0) = G(z=L) = 0 \end{aligned} \tag{4.17}$$

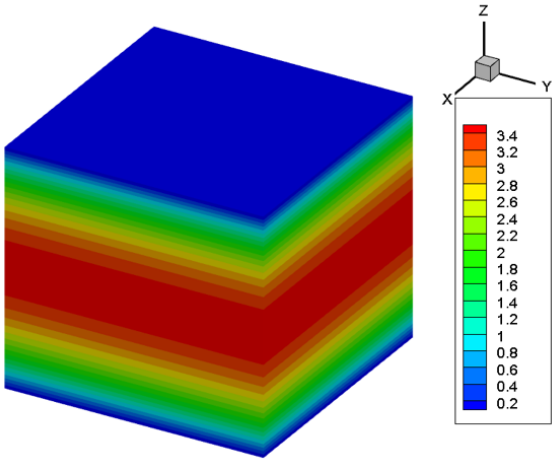

(a) Contours of the function $G(x, y, z)$

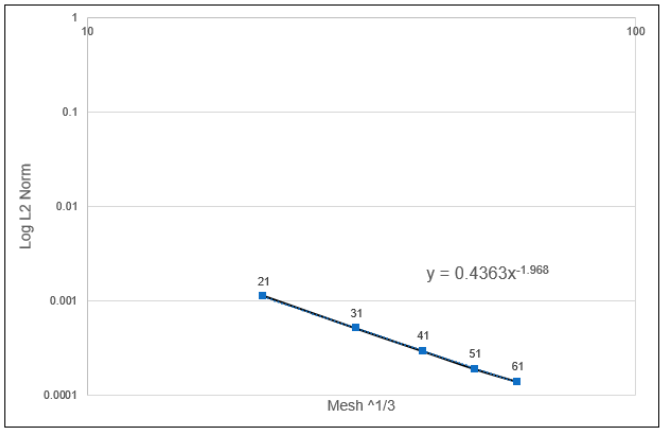

(b) the L2 norm of errors

Figure 4.11 Analytical and numerical solution of Eqn. 4.16 with $G_x(x = 0) = G_x(x = L) = 0$, $G_y(y = 0) = G_y(y = L) = 0$, $G(z = 0) = G(z = L) = 0$

With the mentioned boundary conditions, the function $G(x, y, z)$ has the following exact solution

$$G(x) = \frac{S}{3K^2} - \frac{exp(\sqrt{3}Kx)(S - Sexp(-\sqrt{3}K))}{3K^2exp(\sqrt{3}K) - exp(-\sqrt{3}K)} + \frac{exp(-\sqrt{3}Kx)(S - Sexp(\sqrt{3}K))}{3K^2exp(\sqrt{3}K) - exp(-\sqrt{3}K)} \quad (4.18)$$

Solving the equation using the 2^{nd} order finite difference, the results have been compared to the exact solution. The contours of the function $G(x, y, z)$ as well as the L2 norm of errors are shown in Fig. 4.11. As shown, there is an acceptable agreement between the numerical and the exact solution. The discrepancy between the two results decreases with mesh refinement. The slope of the trend line in Fig. 4.11b shows that the numerical solution has the accuracy of 1.96 which is expected due to the 2^{nd} order discretization.

Isothermal Cylindrical Arc

As a second test case, a comparison to NEC method is presented. This test case comprises a cylindrical Arc ($T_{arc} > 10000K$) surrounded by a cold SF6 ($T_{Cold} = 500K$) as shown in Fig. 4.13.

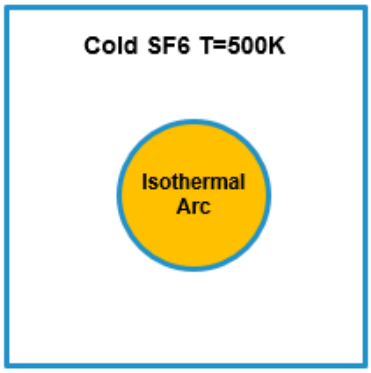

Figure 4.12 Isothermal arc in cold SF6

The arc core temperature was varied from 10000K to 30000K and the net radiation was calculated based on the scheme explained in Section 3.4 using the P1 model (Eqn 3.32). The result is then compared to the work Liebermann and Lowke [45] as shown in Fig. 4.13.

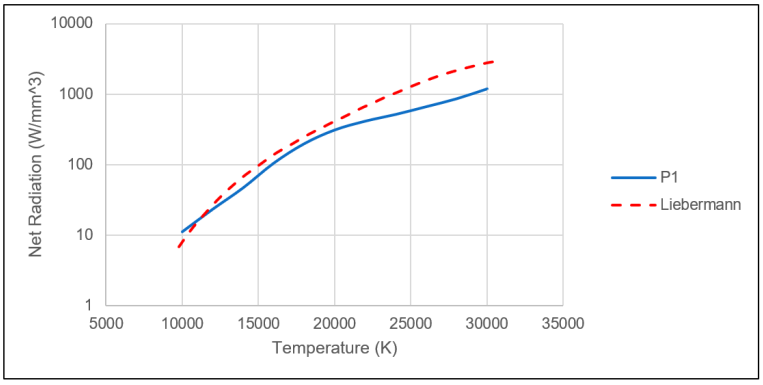

Figure 4.13 Net radiation obtained by the P1 model for a cylindrical Arc ($T_{arc} > 4000K$) surrounded by a cold SF6 ($T_{Cold} = 500K$) compared to the work of Liebermann and Lowke [45]

The comparison shows a relatively good agreement between the two curves for the range of $10000K < T < 20000K$. For higher temperatures, the discrepancy increases (it should be noted that the curves are plotted in *log* scale).

The difference can be mostly related to the range of the wavelength spectrum covered by the the two calculations. In this research, 5 bands are considered in the net radiation calculation which cover wavelengths from 30 to 3000 nm, while Liebermann and Lowke considered a spectral range of 100 to 15500 nm. Also, the NEC model provides the net emission at the arc center, while the P1 model provides a radial distribution of the radiant intensity which also takes into account the cold boundary of the arc.

4.3.2 WENO Scheme Verification

To verify the implemented WENO scheme two test cases are established.

1D Shocktube

In this test case the shocktube problem described in Section 4.1 is solved using the WENO method and the results are compared to the exact and the 1^{st} solution. Fig. 4.14 shows the solution of the WENO scheme applied to a shocktube. A comparison between the 1^{st} order, the WENO scheme and the reference solution shows that the WENO scheme leads to an important improvement of the numerical simulation in the expansion, the shock wave and the discontinuity regions, for a same number of points.

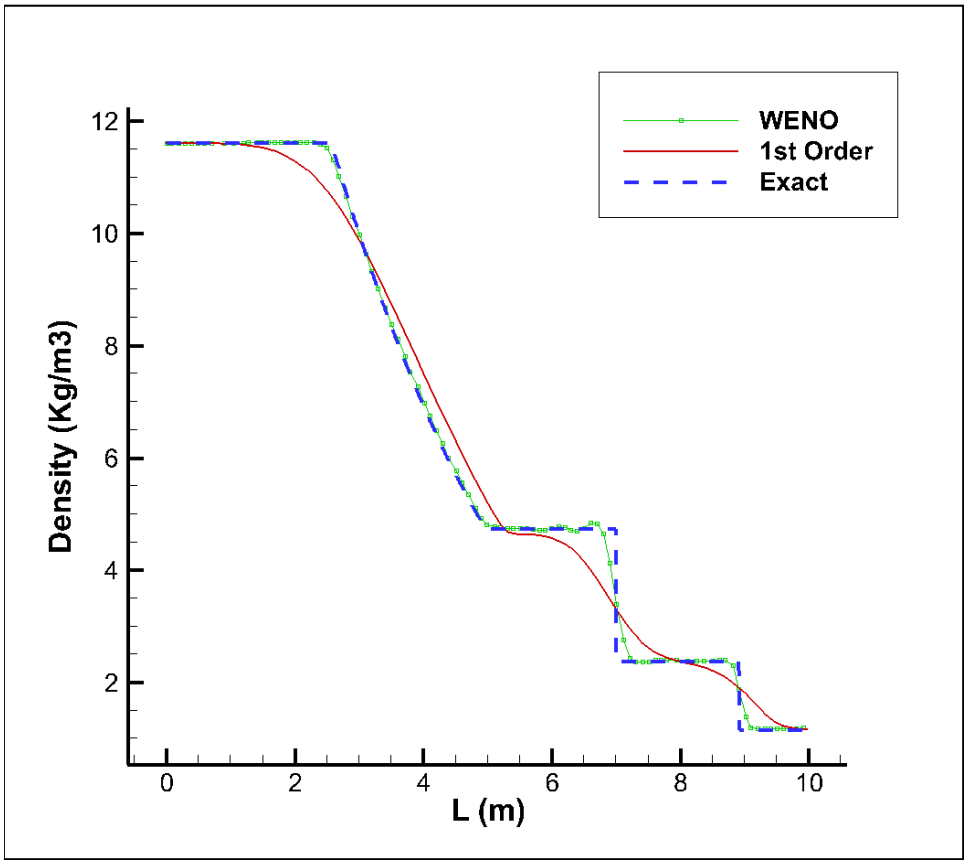

Figure 4.14 A comparison between the 1^{st} order, the WENO scheme and the exact solution for the shocktube problem, 101 points, CFL=0.5

Despite a smooth solution in the shock wave and the expansion regions, the WENO scheme demonstrates slight oscillations in the discontinuity region. As shown in Fig. 4.15, these oscillations can be avoided by increasing the number of the points.

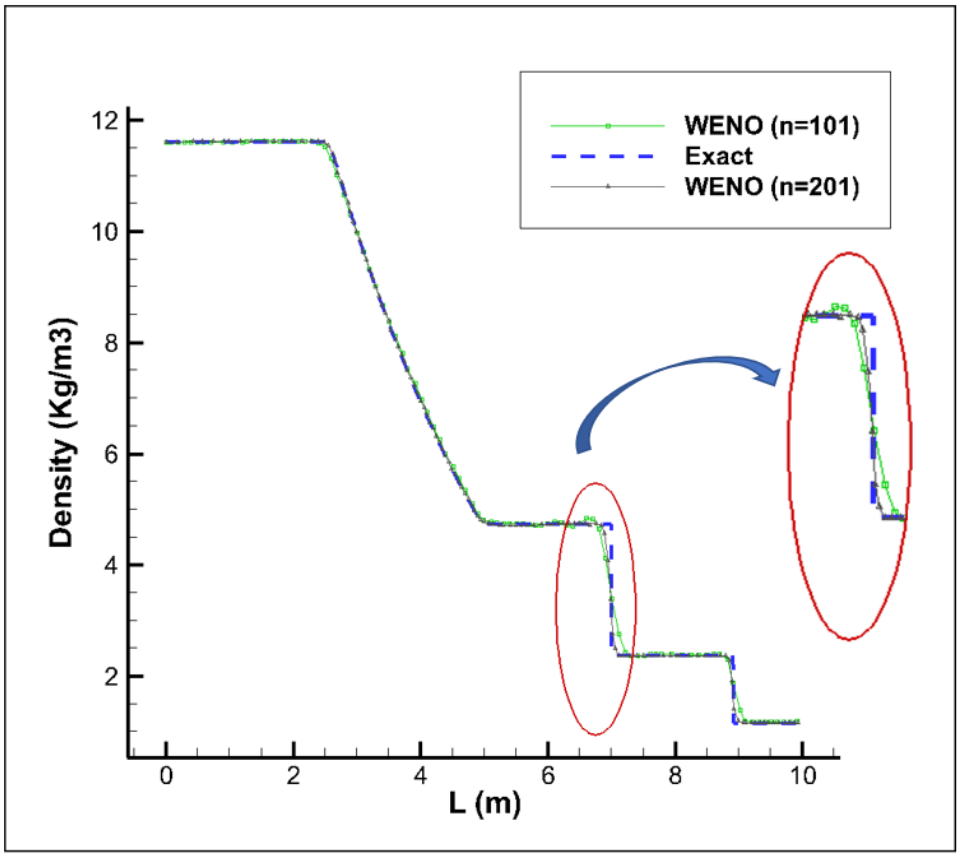

Figure 4.15 The WENO scheme results in oscillations near the contact region that can be avoided by the increasing the number of the points

4.3.3 3D explosion

As explained in the work of Titarev and Toro [49], this test case is a 3D explosion (similar to a shocktube problem in a 3D context) which is used to evaluate WENO scheme. In this research, the same problem is solved and the results are compared with the reference as well as the 1^{st} order solutions.

This problem considers a cube in which a discontinuity of pressure and density is initialized at rest ($u = v = w = 0m/s$) at the time of $t = 0s$, as shown in Fig. 4.16. Similar to the shocktube problem, the contact (a sphere of radius 0.4 m) is removed, letting the high pressure gas drive the low pressure gas. The flow evolves for a period of 0.25 seconds.

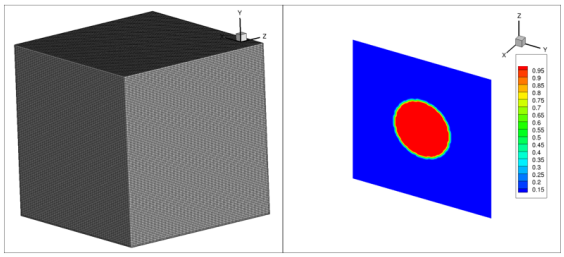

$$\rho, P = \begin{cases} (1.0, 1.0) & r \leq 0.4 \\ (0.125, 0.1) & r > 0.4 \end{cases}$$

Figure 4.16 3D explosion problem (initial conditions)

This problem is solved using both the 1^{st} order, and the WENO scheme. Fig. 4.17 shows the results compared to a reference solution with a very fine mesh (for more details refer to the Section 17.1 of [50]). The 1^{st} order solution provides a diffusive solution which is not able to predict the shock waves and the contact region, accurately. Conversely, the WENO scheme provides a very accurate solution for the shock waves. The same accuracy applies to the contact regions. Furthermore, the prediction of the maximum density has a considerable difference using the 1^{st} order and the WENO schemes.

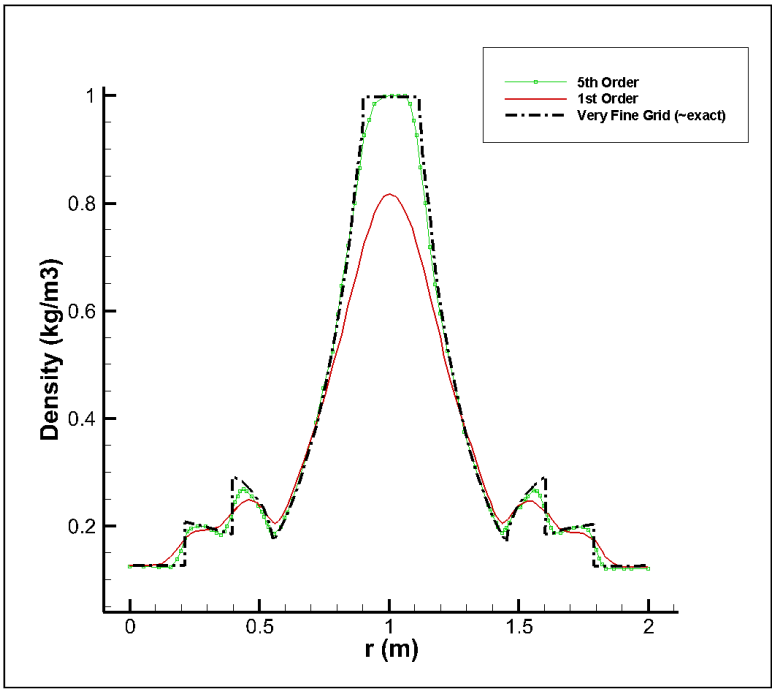

Figure 4.17 radial density profiles for the 3D explosion problem compared for the 1^{st} order scheme, the WENO scheme and the results on a very fine grid (close to exact solution)

4.3.4 Steady Arc

Having verified all the components included in the arc simulation (flow solver, Ohmic heat solver, radiative energy solver and WENO high order scheme) there are still two drawbacks to this verification strategy

1. A test case with all components involved is missing.
2. All test cases included a perfect gas, whereas in the arc simulation a real gas assumption is made.

To resolve these drawbacks, a simple test case is proposed: a steady arc is established and kept at a constant current of 1000 A long enough (1 ms) for the gas properties to converge. This is done for the computational domain inside the Aachen nozzle as explained in Fig. 3.1 and with boundary conditions detailed in Chapter 3. Dimensions of the computational domain are $6mm \times 6mm \times 30mm$ and the mesh size is $\Delta x = \Delta y = \Delta z = 0.176mm$. The simulation CFL number is chosen to be 0.6. In this test case, tables of real gas are used to determine the properties of SF6.

As shown in Fig. 4.18, arc pressure, density and temperature remain steady after several oscillations.

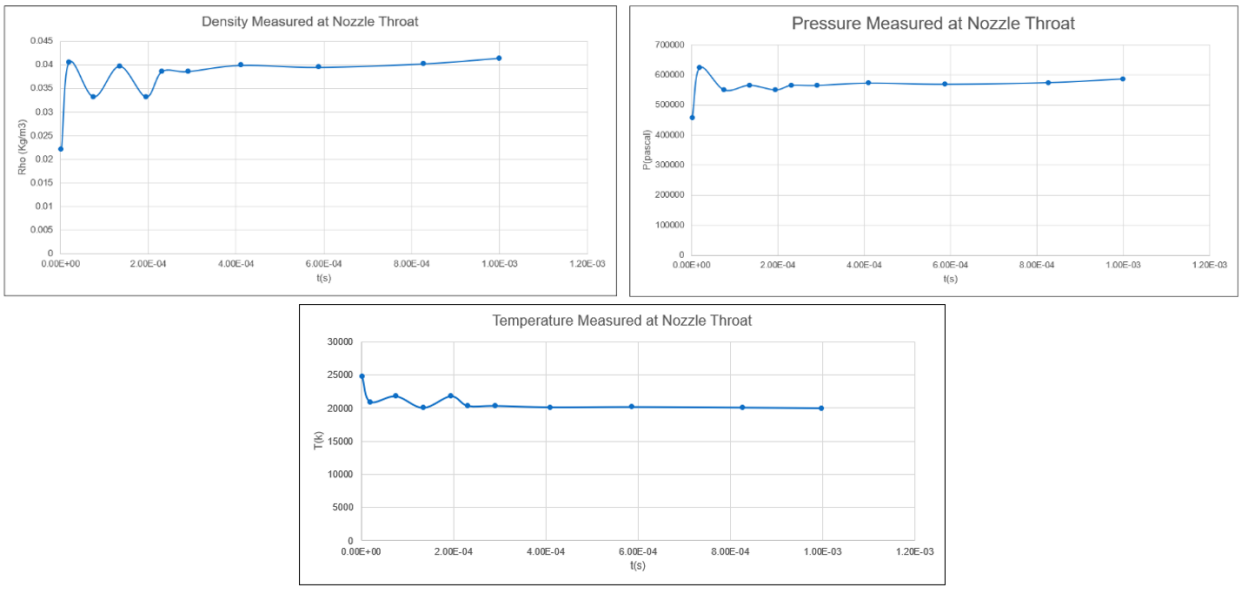

Figure 4.18 Convergence of different gas properties in a steady arc of 1 ms

As a characteristic of arc, the voltage behaviour has been investigated with respect to time as shown in Fig. 4.19. After an overshoot of 450 V all gas properties converged and the arc

remains steady in the 3D solver with all different solver components coupled.

Fig. 4.18 also suggests that the arc must be kept steady for a reasonable period of time before the current is ramped down to the CZ. With this approach, overshoots and undershoots can be avoided leading to more realistic results. In this research, when the arc is initialized with I=1000 A, for the first $5 \times 10^{-5} s$ the current is kept constant.

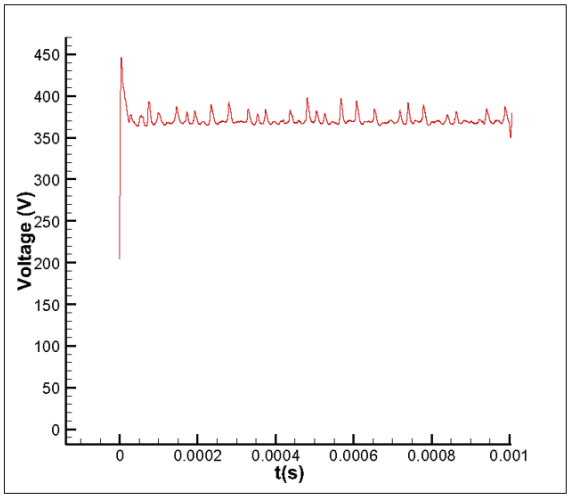

Figure 4.19 Convergence of arc voltage with respect to time

CHAPTER 5 Results and Validation

This chapter is structured with the aim of 1) showing the validation of the SF6 arc simulations and 2) investigating the results regarding the 3D effects and the CZ, separately. All results are presented for a computational domain with the dimensions $6mm \times 6mm \times 30mm$ and with a mesh size of $\Delta x = \Delta y = \Delta z = 0.176mm$ (5.1). The initial current is, for all cases, 1000 A which does not change for the first $5 \times 10^{-5}s$ as detailed in Section 4.3.4. The arc is decreased to CZ with a rate of $\frac{dI}{dt} = -16A\mu s^{-1}$. For the sake of robustness, the simulation CFL number is 0.6 in all cases.

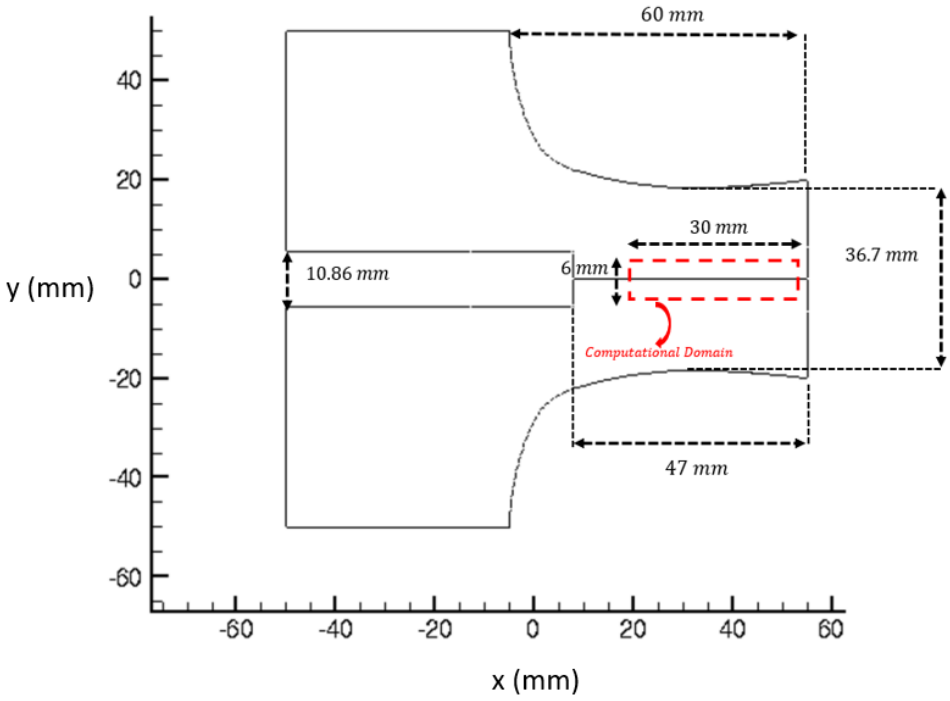

Figure 5.1 Geometry details of the nozzle and the computational domain

5.1 Validation

Arc experimental data is scarce in the literature and only a few existing arc property measurements can be used to validate this simulation. This research uses the temperature profile measurement (available for 100 A and 600 A) as presented in the work of [23]. In Fig. 5.3, the arc temperature profile obtained from the 1^{st} order and the 5^{th} order 3D simulations has been compared to experimental data for 600 A. The location of the temperature profile extraction is depicted in Fig. 5.2.

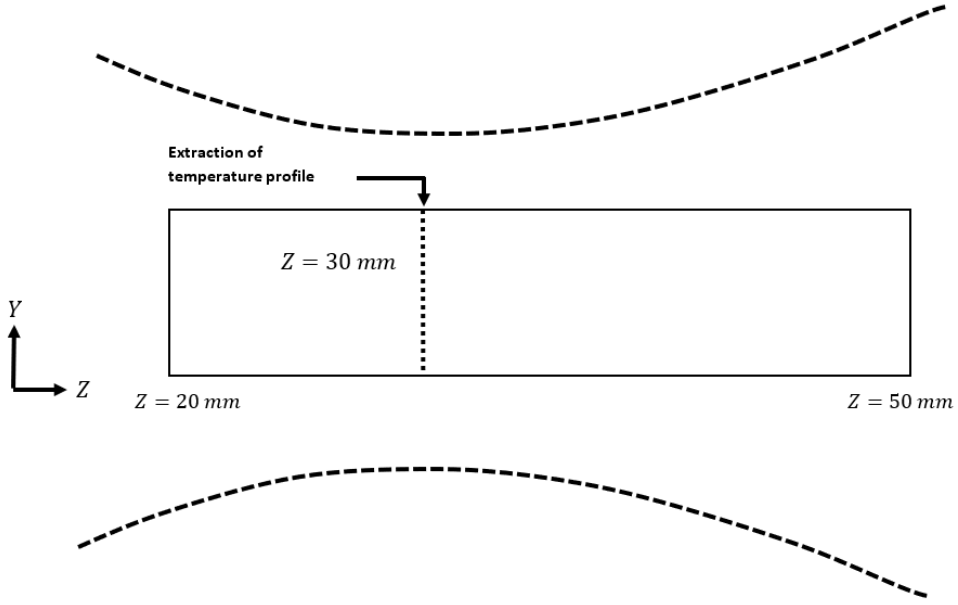

Figure 5.2 Temperature profile extraction details

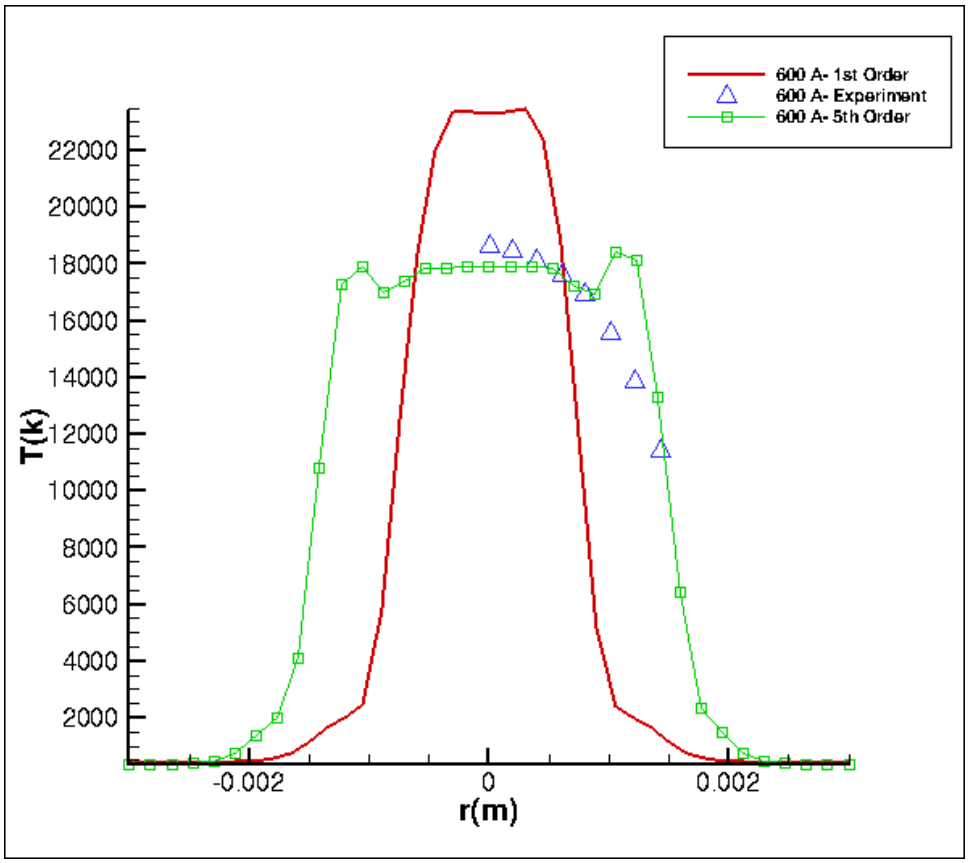

Figure 5.3 A comparison of the numerical (1^{st} order and 5^{th} order) and experimental arc temperature profiles for I=600 A

The discussion regarding this comparison can grouped into the following three categories:

1. Maximum Temperature

   The maximum temperature of the arc (arc core) measured by experiment has the value of 18658 K. This is while the 1^{st} order simulation predicts a core temperature of 23312 K (24.9 % over-estimation) and the 5^{th} order method gives 17923 K (3.9 % under-estimation). A considerable improvement is observed in the max temperature prediction using the WENO 5^{th} order method compared to the 1^{st} order results.

2. Arc Radius

   The arc region can be defined as region where the gaseous medium is electrically conductive. When the temperature exceeds 3500 K the electrical conductivity (σ) of SF6 is large enough to make $\nabla.(\sigma\nabla\phi) = 0$ a meaningful equation. Therefore, it can be simply stated that the arc is present where T $>$ 3500 K.

Using this definition, the arc radius predicted by the 1^{st} order simulation is 0.994 mm while the 5^{th} order scheme predicts a 1.65 mm arc. The experimental data is not available below 11500 K, however it can be inferred that the arc is larger than 1.4mm (the arc radius corresponding to 11500 K).

3. Arc Boundary

   Arc boundary is the interface of the arc plasma and the cold flow. It is observed that WENO resolves the arc boundary better than the 1^{st} order scheme, however, neither follows the expected trend of the arc boundary. The experimental profile shows a smooth transition from the arc core to the boundaries, whereas both numerical methods show sharper curves than expected.

   The reason of such discrepancy is the lack of viscous fluxes. As confirmed in [23], the absence of viscosity causes the solver to neglect the turbulent mixing which is the dominant mechanism in mixing of the hot plasma with the cold flow.

Obtaining the same temperature profile comparison at 100 A, presented in Fig. 5.4, confirms the validation for a smaller current.

1. Maximum Temperature

   The existing measured temperature predicts 14853 K as maximum. The 1^{st} and 5^{th} order schemes give 17205 K (15.8 % over-estimation) and 13584 k (8.5 % under-estimation), respectively. This confirms that WENO is still the more accurate scheme.

2. Arc Radius

   The value of the arc radius predicted by the 1^{st} order scheme is 0.85 mm while with WENO method, this amount is increased to 1.05 mm. Based on the last point of the measured temperature, the arc radius is larger than 0.7 mm.

3. Arc Boundary

   As for the 600 A arc, neither methods is capable of predicting an accurate arc boundary due to the absence of viscous terms.

5.2 Current Zero Investigation

The arc is investigated at the CZ providing a detailed information (contours, curves, profiles) regarding the properties such as temperature, pressure, density, the Mach number and velocity. Furthermore, the variation of the arc voltage and resistance from the initial current

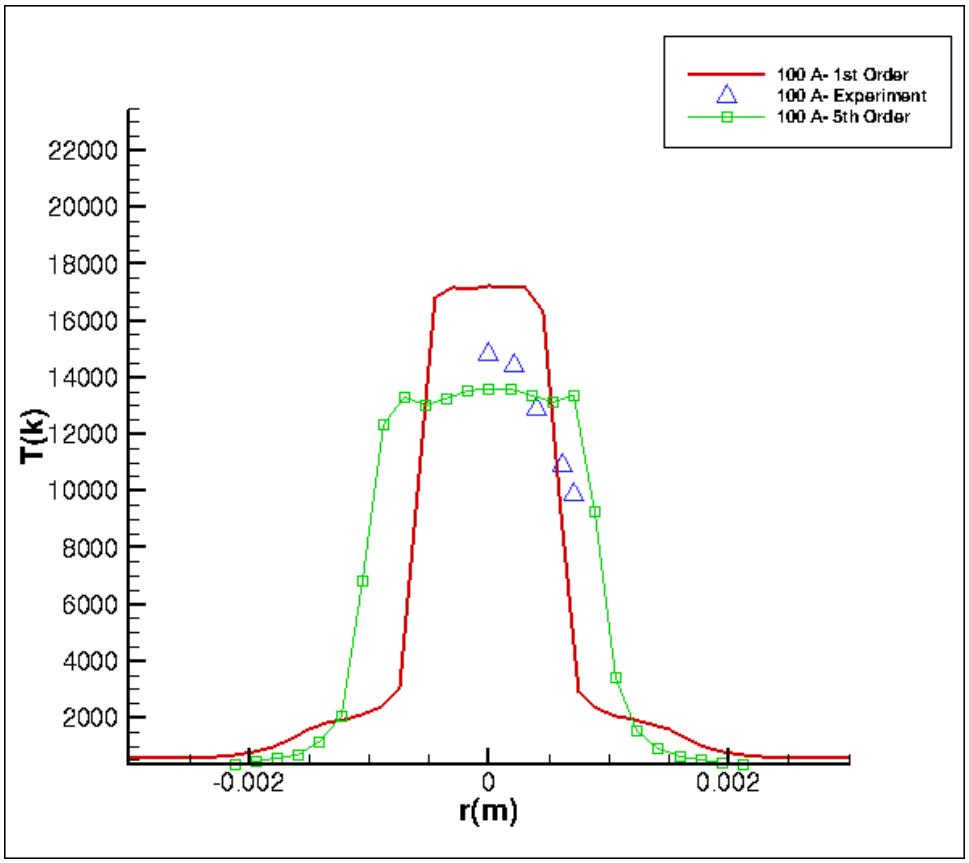

Figure 5.4 A comparison of the numerical (1^{st} order and 5^{th} order) and experimental arc temperature profiles for I=100 A

($I = 1000A$) to the CZ is presented, as well as the energy balance. At each point, the 1^{st} order results are compared to their 5^{th} order counterpart. All sections are for Z=30 mm at the nozzle throat (as shown in Fig. 5.2) unless otherwise stated.

5.2.1 Flow Properties

Temperature

As shown in Fig. 5.5 the arc temperature reaches 14047 K at the section of Z=30 mm while the arc radius measures 0.50 mm. The smallest arc radius (0.336 mm), where the arc has the tendency to break, is found at Z=42 mm where the temperature reaches 16081 K as shown in Fig. 5.5c. The fast transition from the arc core to the arc boundary can be inferred from the radial temperature profile slope.

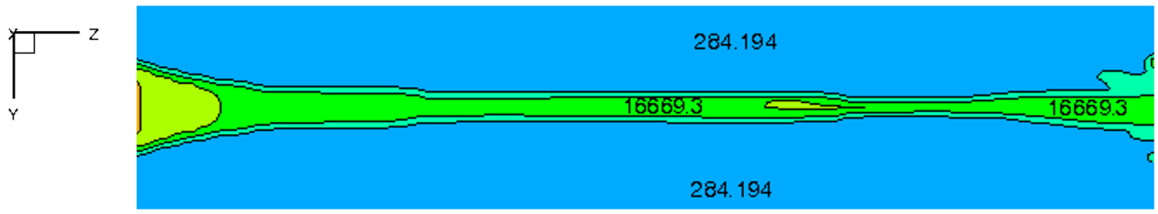

(a) Contours

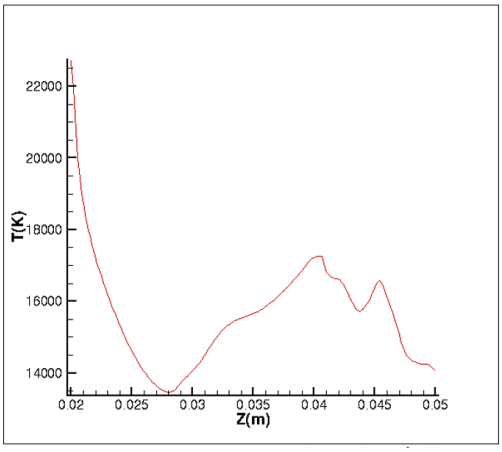

(b) Along axis

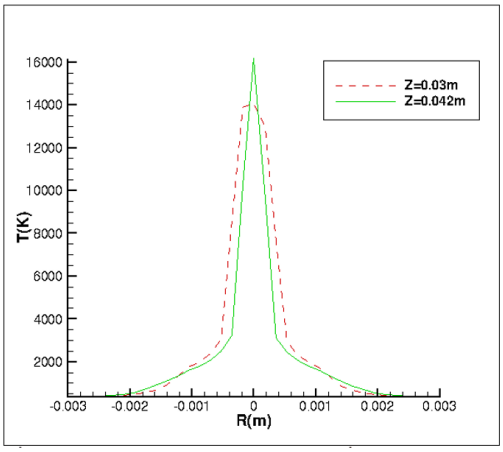

(c) Radial

Figure 5.5 Temperature obtained by the 1^{st} order scheme at CZ

Comparison of the arc temperature for 1^{st} and 5^{th} order:

- Arc Radius

  Contrary to the 1^{st} order scheme, the radial temperature profile obtained from the 5^{th} order scheme (Fig. 5.6c) shows a relatively constant arc radius (0.88 mm) in different sections. The 1^{st} order simulation predicts a smaller radius. This is the same trend as presented in Section 5.1.

- Max Temperature

  As previously concluded in Section 5.1, the WENO scheme predicts a lower temperature than the 1^{st} order scheme. At CZ, the temperature varies between 9500 K and 10500 K for the WENO scheme, whereas this value varies between 13000 K and 16500 K for the 1^{st} order scheme.

- Temperature Variation Along the Arc Axis

  It can be observed from Fig. 5.6b that the variation of the temperature obtained by WENO is considerably less than the temperature calculated by the 1^{st} order scheme.

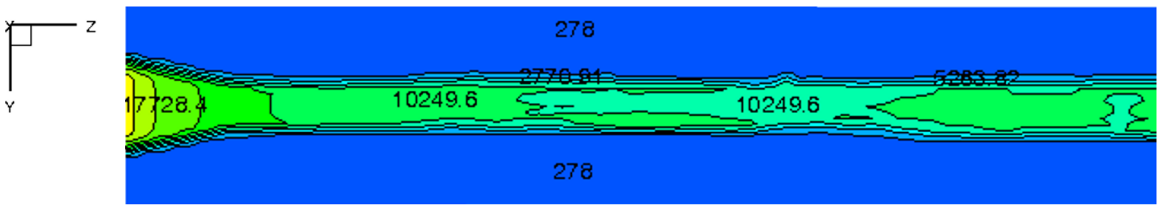

(a) Contours

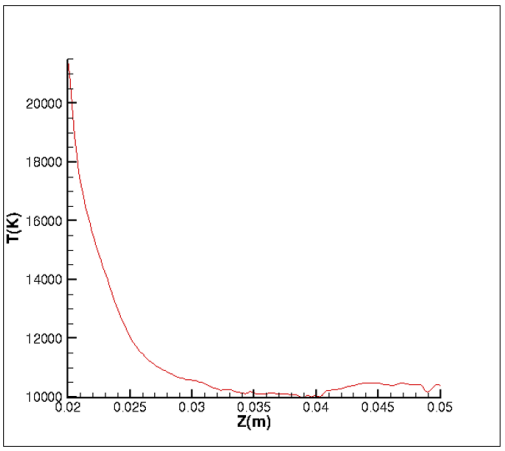

(b) Along axis

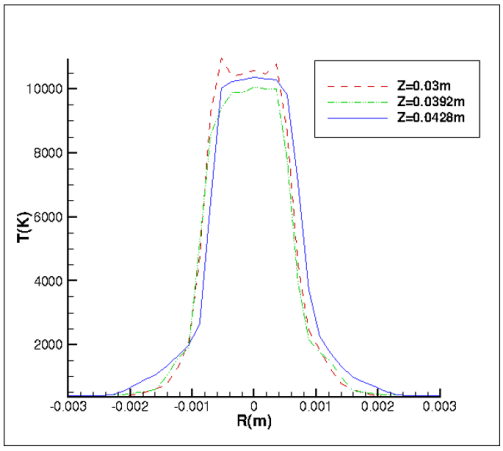

(c) Radial

Figure 5.6 Temperature obtained by the 5^{th} order scheme at CZ

Pressure

The 1^{st} order pressure calculation shows a variation between 6.5 bar and 3.3 bar along the arc axis as shown in Fig. 5.7. This range is almost the same for the 5^{th} order pressure results (Fig. 5.8). Both schemes predict a pressure drop in the arc boundaries. While the 1^{st} order pressure contours seems very symmetric, WENO scheme introduces asymmetry to the pressure distribution.

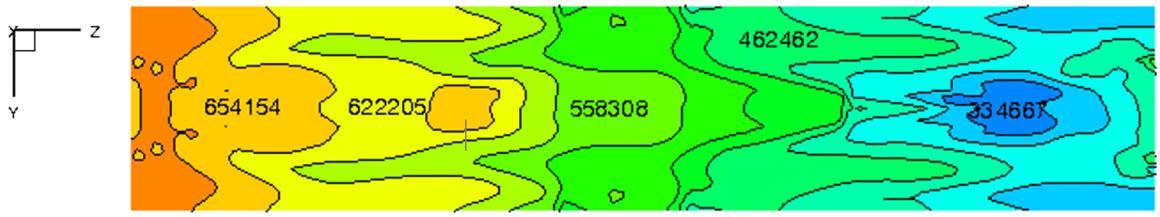

(a) Contours

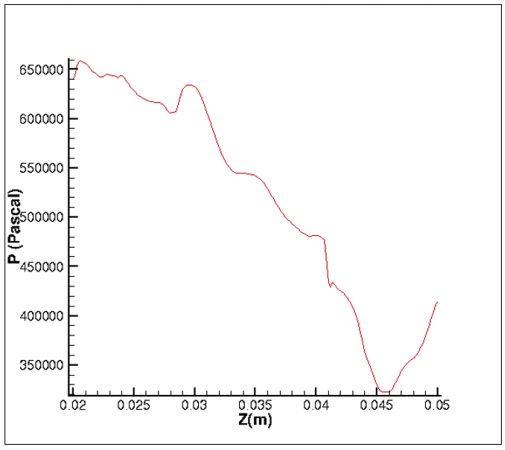

(b) Along axis

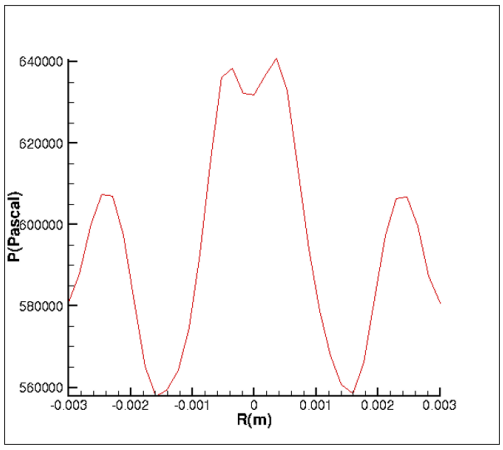

(c) Radial

Figure 5.7 Pressure obtained by the 1^{st} order scheme at CZ

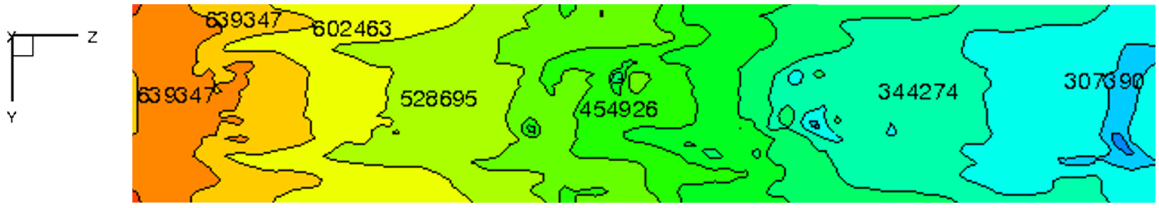

(a) Contours

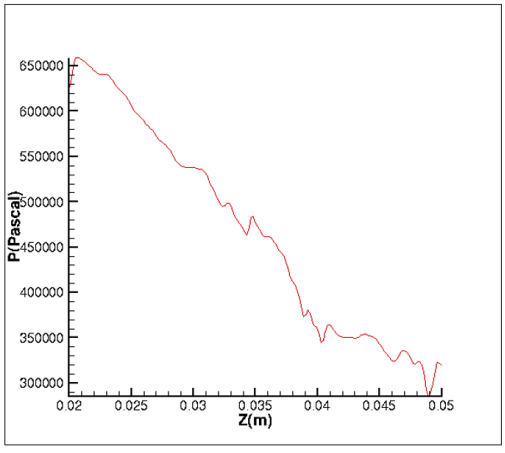

(b) Along axis

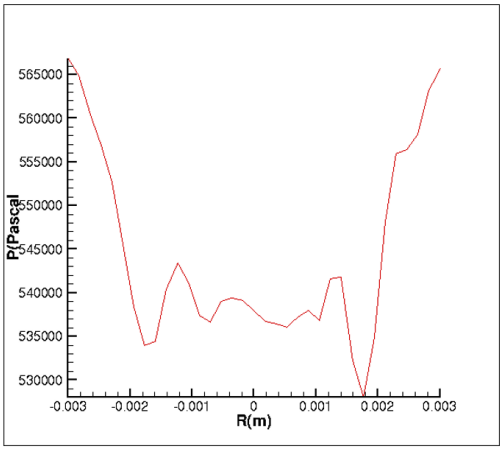

(c) Radial

Figure 5.8 Pressure obtained by the 5^{th} order scheme at CZ

Density

With a very low density in the arc core and high density gradients at the arc boundaries, density calculation is very critical in arc simulation and must be treated cautiously particularly in high order simulations. The following characteristics can be found from the density contours and curves; obtained from different schemes (Fig. 5.9 the 1^{st} order scheme, Fig. 5.10 the 5^{th} order scheme).

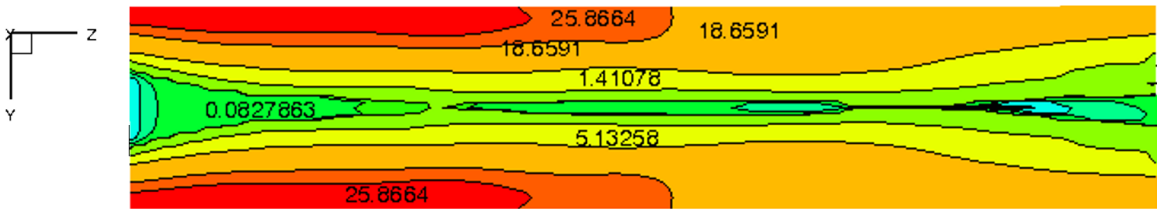

(a) Contours

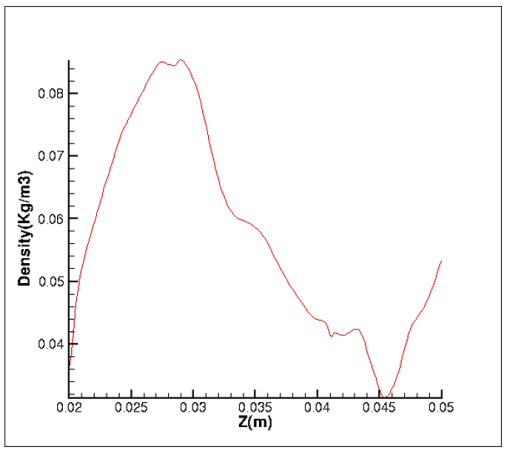

(b) Along axis

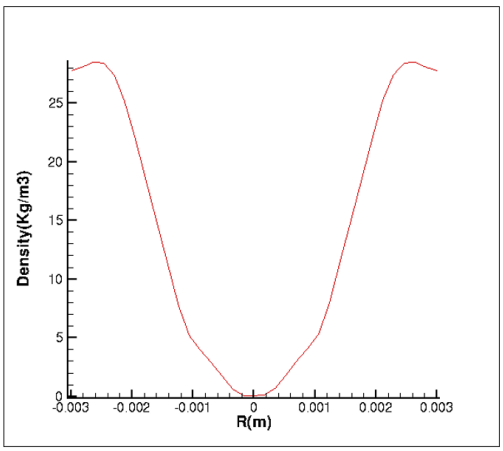

(c) Radial

Figure 5.9 Density obtained by the 1^{st} order scheme at CZ

- Reduced Mass in the Arc Core

  The density varies between 0.02 and 0.15 kg/m^3 in the arc core. This means the mass inside the arc core is relatively small compared to the values away from the arc core.

- High Gradients

  Both 1^{st} and 5^{th} order schemes result in high gradient density curves as shown in Fig. 5.9 and 5.10. This exists for both the arc core and the arc boundary.

  The density gradient is smaller near the arc core for the WENO scheme. One reason might be the treatment carried out to prevent negative density. Due to the high gradient

as well as near-zero values, density can become negative which is not realistic and causes the code to crash. Negative values of density and pressure usually occur for high order analysis of low density or low pressure problems. Negative values can be obtained during spatial reconstructions or temporal integration. For negative values created over time, different class of positivity preserving methods exist ([54–56]). The method used in this research addresses the positivity preserving over the spatial reconstruction. As explained in Section 3.6.2, a stencil of five cells is used to interpolate the gas properties on the desired points or

$$v_{int} = IntFunction(v_1, v_2, v_3, v_4, v_5) \tag{5.1}$$

where v is the interpolated variable and $IntFunction$ is the interpolation function. A negative value can be prevented by using an always positive function e.g. exp such that

$$v_{int} = exp(IntFunction(log(v_1), log(v_2), log(v_3), log(v_4), log(v_5))). \tag{5.2}$$

In this research the solver automatically switches to Eqn. 5.2 if a negative density or pressure is detected.

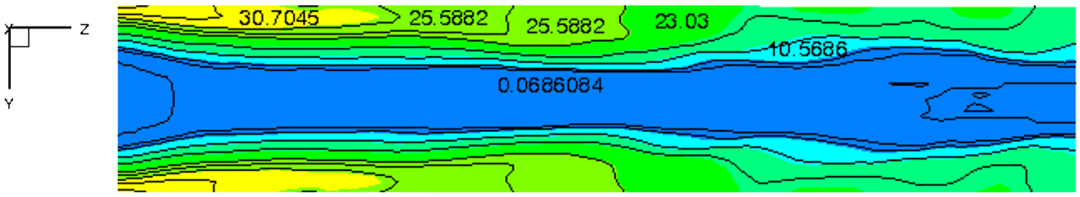

(a) Contours

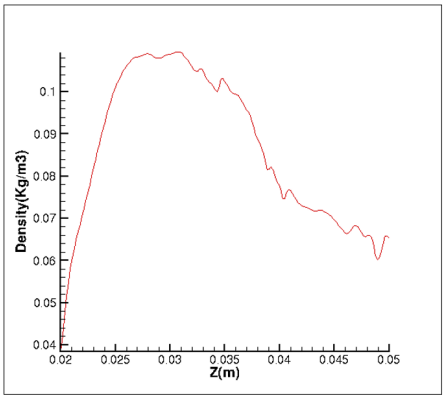

(b) Along axis

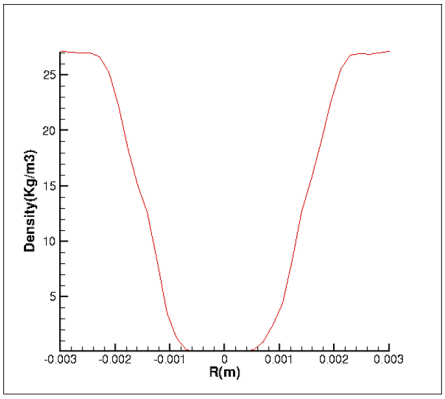

(c) Radial

Figure 5.10 Density obtained by the 5^{th} order scheme at CZ

Mach number

Mach contours reveal that both subsonic and supersonic flows exist in the arc as confirmed in [14]. While for the 1^{st} order simulation, the Mach number is higher at the arc boundary than at the arc core (Fig. 5.11), the WENO scheme predicts a different behaviour where the Mach number becomes lower at the arc boundary compared to the arc core (Fig. 5.12). As mentioned previously, high gradient properties in the arc boundary lead to a different behaviour in the arc core than at the arc boundary. The contours obtained by both 1^{st} order and WENO schemes are relatively symmetric which shows that the arc remains symmetric at the CZ when initialized symmetrically at I=1000 A.

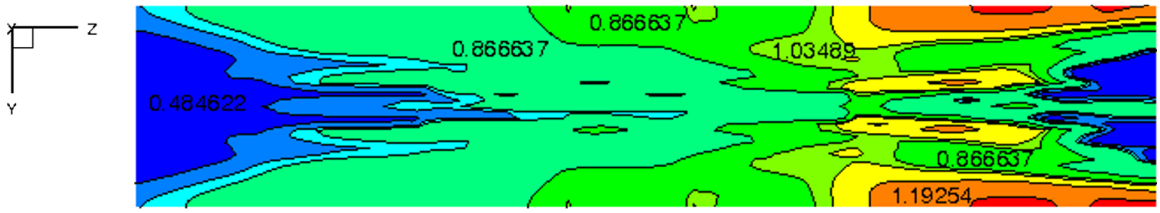

(a) Contours

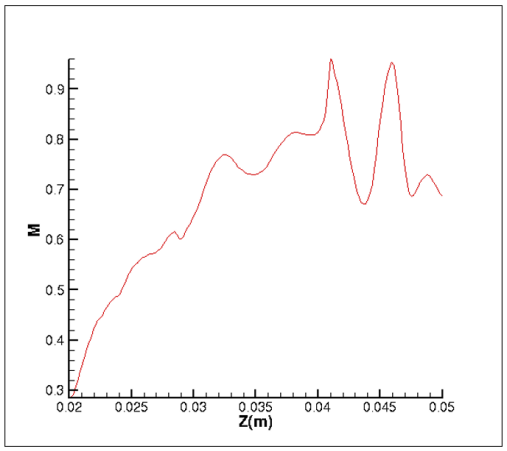

(b) Along axis

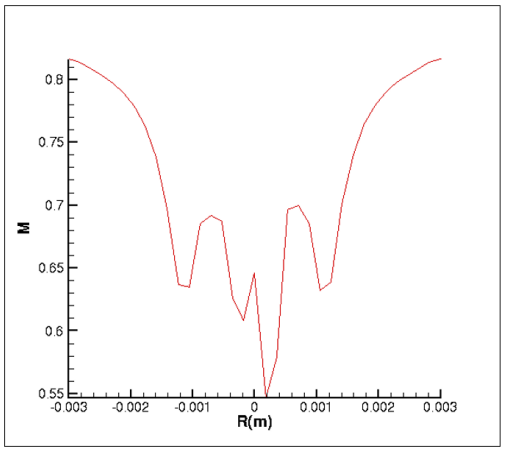

(c) Radial

Figure 5.11 Mach number obtained by the 1^{st} order scheme at CZ

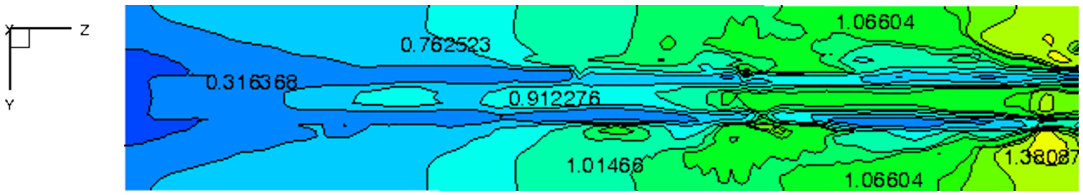

(a) Contours

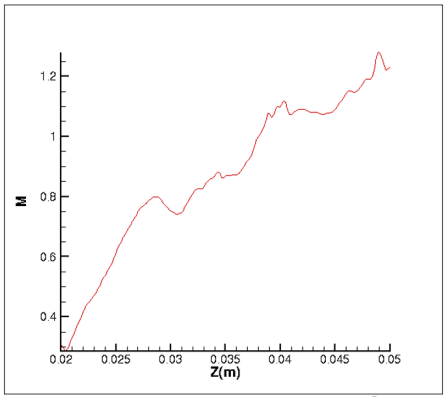

(b) Along axis

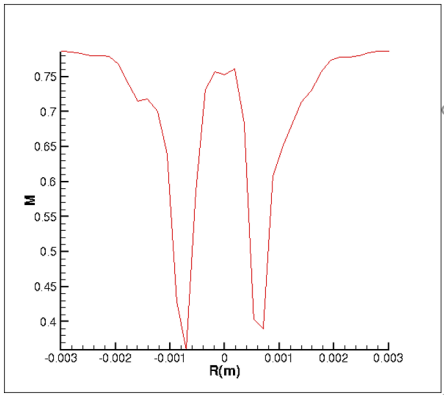

(c) Radial

Figure 5.12 Mach number obtained by the 5^{th} order scheme at CZ

Axial velocity

The calculated velocity by both 1^{st} and 5^{th} order schemes reaches 3400 m/s. The high velocity makes convection the dominant transport mechanism. Both radial velocity profiles show the same velocity value (around 2000 m/s) whereas the velocity behaviour along the arc axis is slightly different. It increases almost constantly in the results predicted by the WENO scheme (Fig.5.14) while the 1^{st} order velocity calculation (Fig. 5.13) presents two peaks.

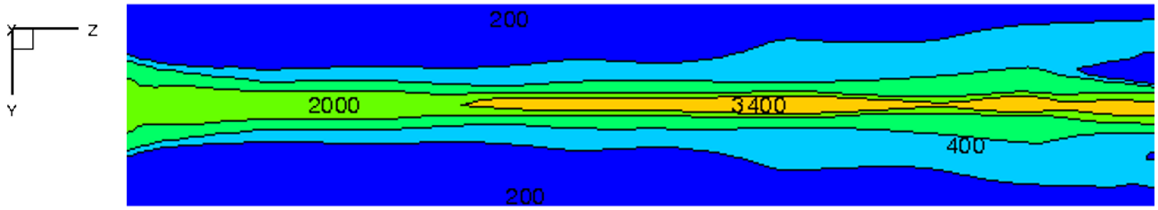

(a) Contours

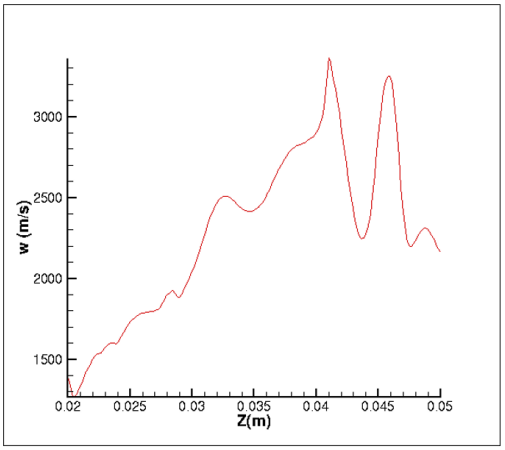

(b) Along axis

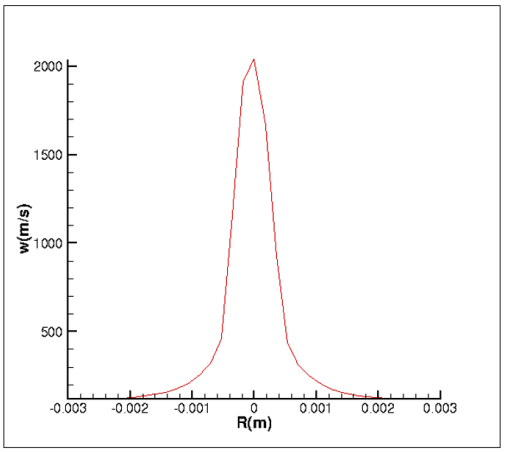

(c) Radial

Figure 5.13 Velocity obtained by the 1^{st} order scheme at CZ

Although the 5^{th} order velocity follows the same trend at CZ as the initial arc (i.e reaching the max velocity value at the nozzle exit), it is difficult to determine which is more accurate.

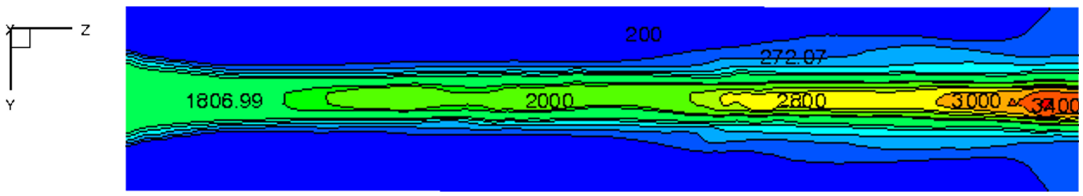

(a) Contours

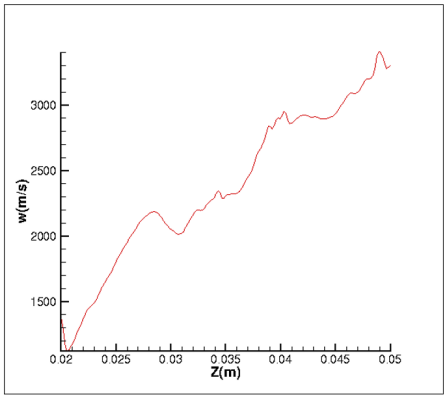

(b) Along axis

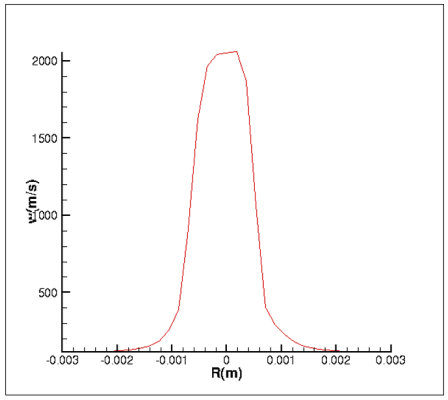

(c) Radial

Figure 5.14 Velocity obtained by the 5^{th} order scheme at CZ

5.2.2 Arc Properties

An investigation of the arc properties such as resistance and voltage gives a global view of arc behaviour over time. As discussed in chapter 3, the arc voltage can be calculated from Eqn. 3.29 repeated here for simplicity.

$$V = \frac{I}{\int_\Omega \sigma |e|^2 \mathrm{d}v} \tag{5.3}$$

therefore, the arc resistance is given by

$$R = \frac{1}{\int_\Omega \sigma |e|^2 \mathrm{d}v} \tag{5.4}$$

or

$$R = \frac{1}{\sum_{n=1}^{ncell} \sigma_n |e_n|^2 \Delta v} \tag{5.5}$$

for a discrete domain.

Fig. 5.15 shows the variation of arc resistance from the initial point (I=1000 A) to CZ from which the following characteristics can be extracted

- The Resistance Value

  While the resistance obtained from the 1^{st} order scheme reaches 34 Ohm at the CZ, WENO scheme predicts no more than 5.3 Ohm. Considering Eqn. 5.4, either the electrical conductivity σ or the electrical field e accounts for this difference. Remembering that the plasma conductivity σ has a strong dependency on the temperature which is lower for the 5^{th} order scheme (discussed in Section 5.2.1), σ values are reduced when obtained by the WENO and cannot be considered as the reason of reduced resistance. Therefore, it can be concluded that the value of the electric field has increased when calculated by the WENO.

- Resistance-Time Curve Trend

  The behaviour of the resistance from I=1000 A to CZ is the same for both schemes: the arc resistance increases as the current decreases. This is expected from the arc since the decrease of current leads to a decrease in the Ohmic source term. On the other hand, as time evolves, the cold SF6 has more time to interact with the arc and make it cooler. Consequently at CZ, the gas medium is less conductive due to a lower temperature (lower σ) which is an equivalent to the resistance increase.

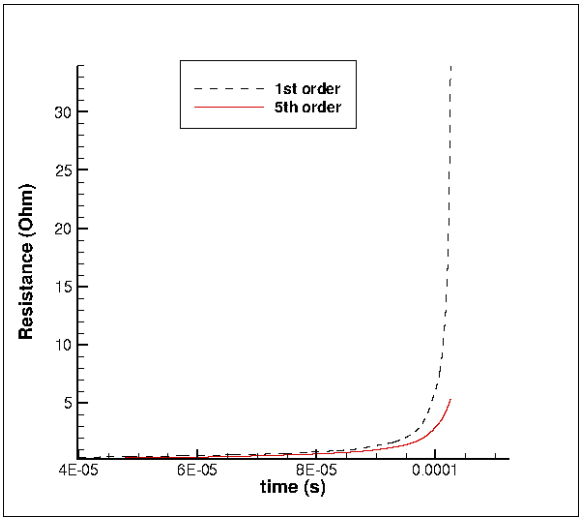

Figure 5.15 Arc resistance variation with time compared for the 1^{st} order and the 5^{th} order schemes

The investigation of arc voltage variation with time is of importance. Particularly at the CZ, the network voltage starts to influence the circuit breaker instantly and, as discussed in chapter 1, a restriking post-arc might make the gaseous medium conductive again.

Fig. 5.16 shows the arc voltage variation over time obtained from the 1^{st} order and the WENO schemes. The following information can be inferred from the two curves:

- Voltage Value

  It is observed that the voltage calculated by the 5^{th} order scheme has a lower value than that from the 1^{st} order scheme. When I=1000 A, the voltage is calculated at 372 V and 296 V by the 1^{st} and the 5^{th} order schemes, respectively. Since the WENO scheme predicts a lower arc resistance, lower calculation of voltage (compared to the 1^{st} order results for a similar current) is expected. This difference diminishes as the current approaches CZ.

- Voltage-Time Curve Trend

  Both curves shown in Fig. 5.16 demonstrate that the voltage tends to zero at CZ (1.25 V predicted by the 1^{st} order and 8.8 V calculated by the 5^{th} order scheme). As shown in Fig. 5.17, this trend is confirmed by Leseberg [53] who investigated the same nozzle as this research.

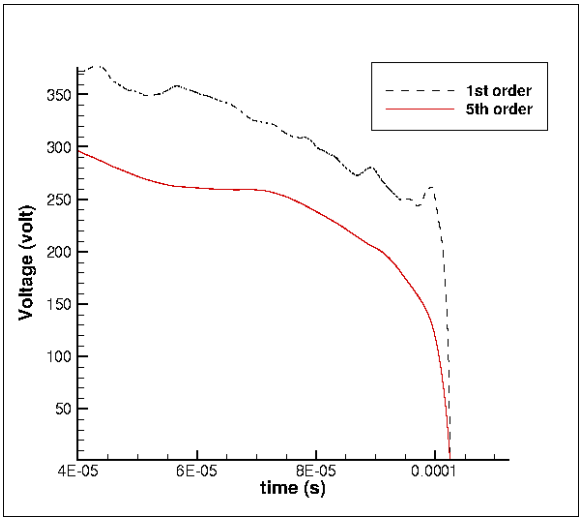

Figure 5.16 Arc voltage variation with time compared for the 1^{st} order and the 5^{th} order schemes

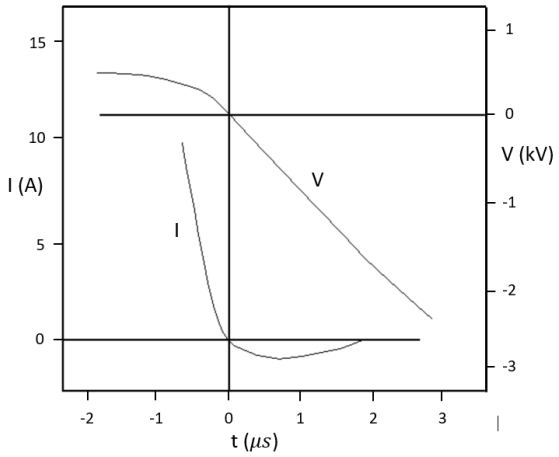

Figure 5.17 Voltage and current curves versus time from the work of Leseberg [53] showing voltage approaches zero at CZ for the Aachen nozzle

As another arc property, the variation of the arc radius with time is compared for the 1^{st} order and the WENO schemes in Fig. 5.18. As expected, the arc radius decreases as the current approaches zero for both schemes. It has been already discussed (Section 5.2.1) that the predicted arc radius is smaller for the 1^{st} order scheme as compared to the 5^{th} order scheme. While both schemes result in roughly the same arc radius for I=1000 A, a large discrepancy is observed between the two schemes for I=700 A. Finally, as discussed in Section 5.2.1, the smallest arc radius is obtained at the CZ.

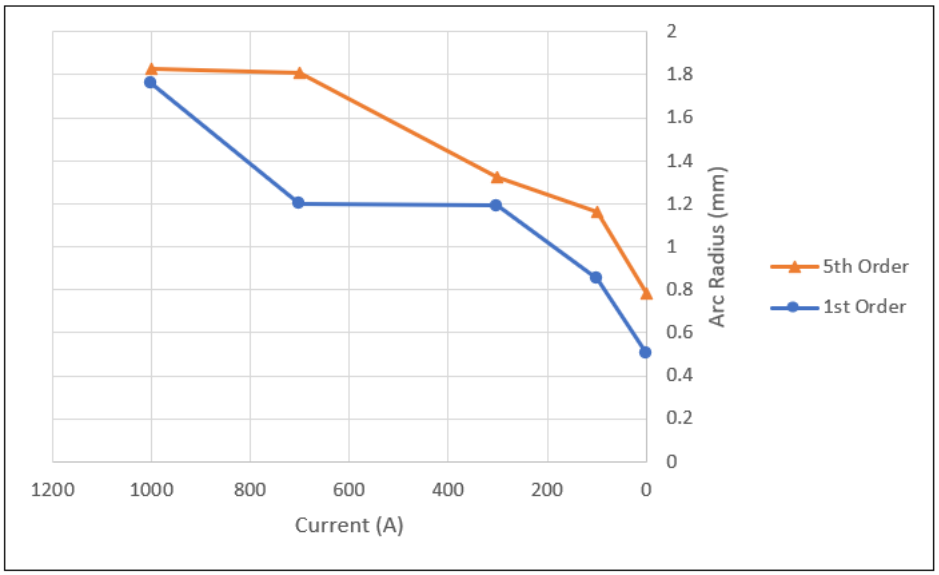

Figure 5.18 Arc radius variation with time compared for the 1^{st} order and the 5^{th} order schemes

5.2.3 Energy Source Terms Close to CZ

In Figs. 5.19 and 5.20 the Ohmic and the radiative source terms are compared for the 1^{st} order and the 5^{th} order schemes, respectively. With this analysis on the energy source terms, the following items can be concluded when the current is very close to zero (0.5-0.1 A),

- General Characteristics

  As shown for the energy sources, the heat is generated by the ohmic energy (positive) in the arc core while radiation cools the arc by transferring the energy from the arc core (negative) to the arc boundary (positive). Beyond the arc boundaries both energy sources are zero.

- The Predicted Energy Value

  As expected, the value of the Ohmic and the radiative energies are predicted with a lower amount with the WENO scheme compared to the 1^{st} order scheme. This can be explained by remembering that the radiative and the Ohmic heating depend strongly on the temperature, which has lower values when calculated by the WENO scheme.

- Ohmic Energy VS. Radiative Energy

  The value of the Ohmic source term is directly proportional to the current. That is why it is expected (and observed in Fig. 5.19) that the Ohmic source term approaches zero at CZ. Compared to the radiative energy, the Ohmic energy is negligible. It can be concluded that radiation remains the dominant energy transfer mechanism from the initial point (I=1000 A) to CZ.

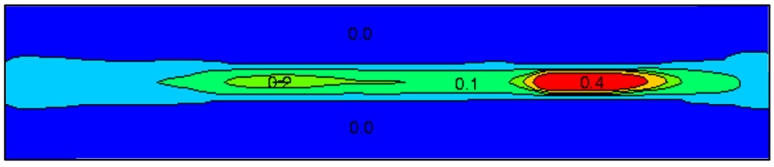

(a) 1^{st} order

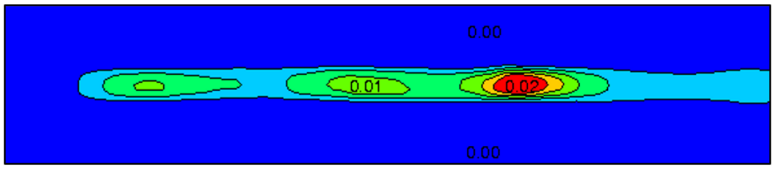

(b) 5^{th} order

Figure 5.19 The contours of the Ohmic energy ($\frac{w}{mm^3}$)

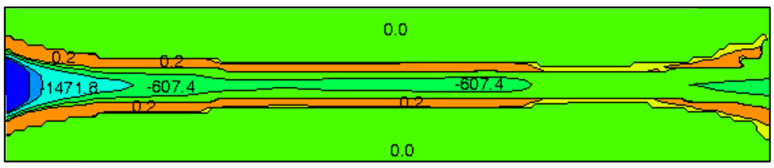

(a) 1^{st} order

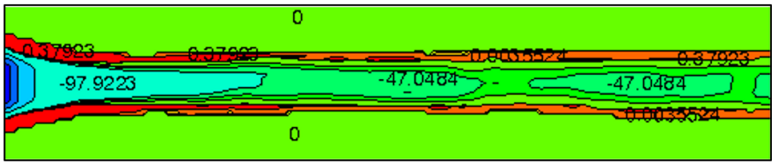

(b) 5^{th} order

Figure 5.20 The contours of the radiative energy ($\frac{w}{mm^3}$)

5.3 Arc 3D Effects

One objective of this research is to investigate the capability of the Euler equations to capture the arc 3D effects. In experiment, the arc does not remain axisymmetric, especially when the current decreases to zero [10]. However, reviewing the numerical simulation presented for the arc at CZ (Section 5.2) it is observed that arc remains symmetric.

Since the arc-flow in the circuit breakers is never perfectly symmetric, in this section the computational domain around the arc is initially displaced slightly from the center as shown in Fig. 5.21 to introduce a slight asymmetry and to enhance the simulation.

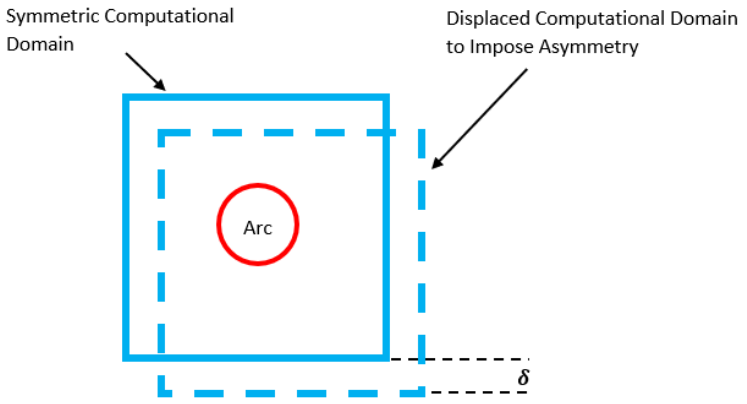

Figure 5.21 Arc center displaced slightly to generate a small asymmetry

The goals of generating this asymmetry are to

1. Investigate the appearance of arc 3D effects and if these effects can be numerically simulated.

2. Quantify the impact of such 3D effects on the arc resistance and eventually lead to a predictive capability of the arc extinction.

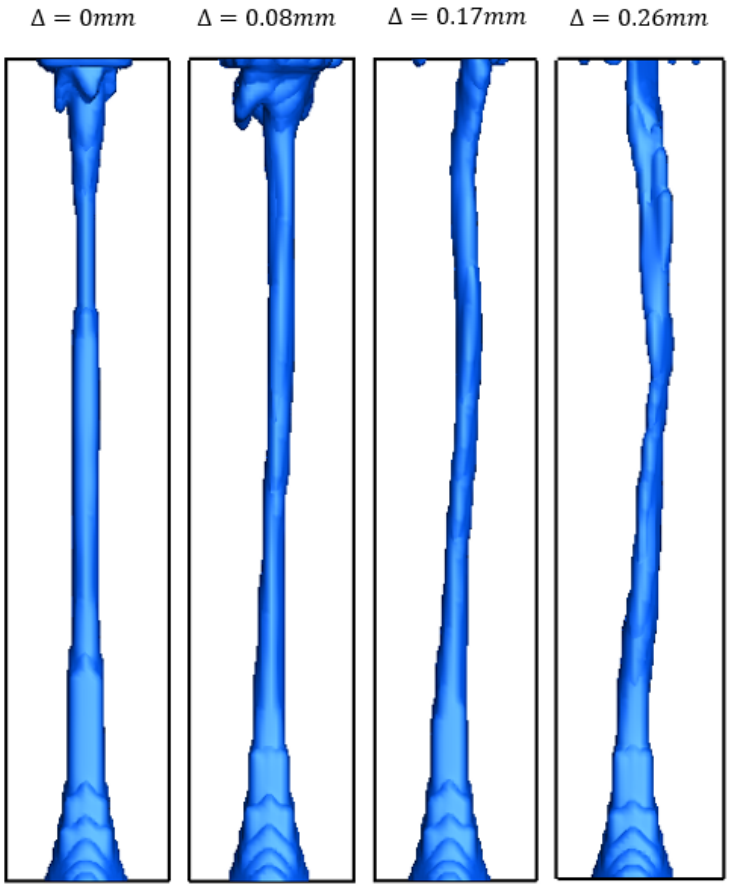

Figure 5.22 Iso-surface of T=4000 K showing the arc 3D effects increase with the growth of computational domain displacement

Using the 1^{st} order scheme, the displacement δ, as shown in Fig. 5.21, is varied from 0 to $0.26mm$ (this value has been chosen based on mesh size i.e $0.0\Delta x, 0.5\Delta x, 1.0\Delta x, 1.5\Delta x$). As shown in Fig. 5.22 the iso-surfaces of T=4000 K (representing the arc) suggests an asymmetry. With the increase of δ, more deviation from the arc axis is observed which results is more 3D features. Another observation is that the 3D arc has a random shape which is not symmetric with respect to either ZY or ZX planes. It is worth mentioning that in all cases shown in Fig. 5.22 the arc is initialized symmetrically at 1000 A.

The same 3D behaviour can be found for the other arc properties out of which temperature, axial velocity and the radiative energy have been shown in Fig. 5.23. To simplify the analysis, only the results for the arc with $\delta = 0.26mm$ are presented.

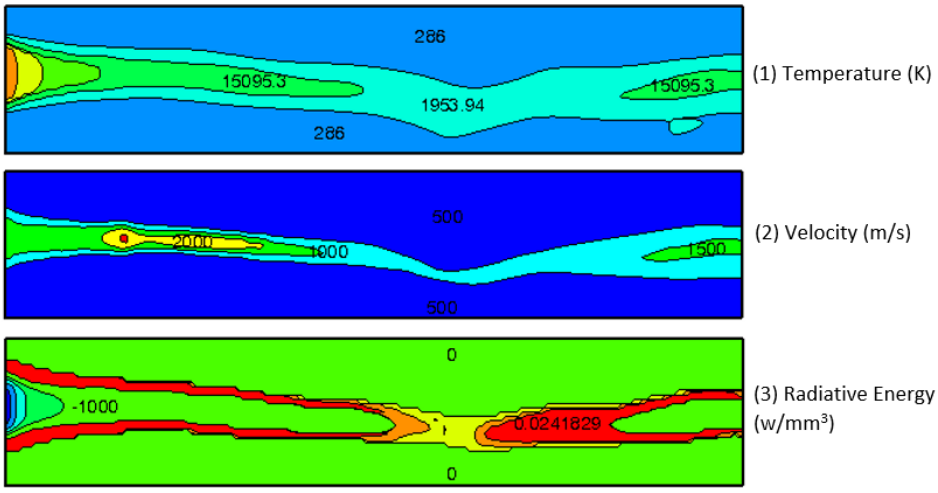

Figure 5.23 The 3D effect observed in the temperature, axial velocity and the radiative energy for the arc with $\delta = 0.26mm$ at CZ

5.3.1 Arc 3D Effects Measurement

Having presented qualitative results illustrating the arc 3D behaviour, this section provides a more detailed investigation on the arc resistance affected by this 3D effect.

Despite the importance of all the arc properties, the arc resistance is chosen for more investigations for the two following reasons:

1. The arc resistance represents a global property. This is while other properties such as temperature, pressure, density and etc. vary from point to point, which makes it less informative to elaborate on them.

2. At CZ, the arc resistance is a critical parameter on which the extinction or re-ignition highly depend. Accurate prediction of the resistance is crucial since it has a strong impact on the circuit breaker performance.

As shown in Fig. 5.24, as the computational domain is more eccentric (more asymmetry), the arc resistance increases. This clearly conveys the importance of 3D arc simulation at CZ. The increase in the arc resistance is not linear with respect to the displacement. The value of

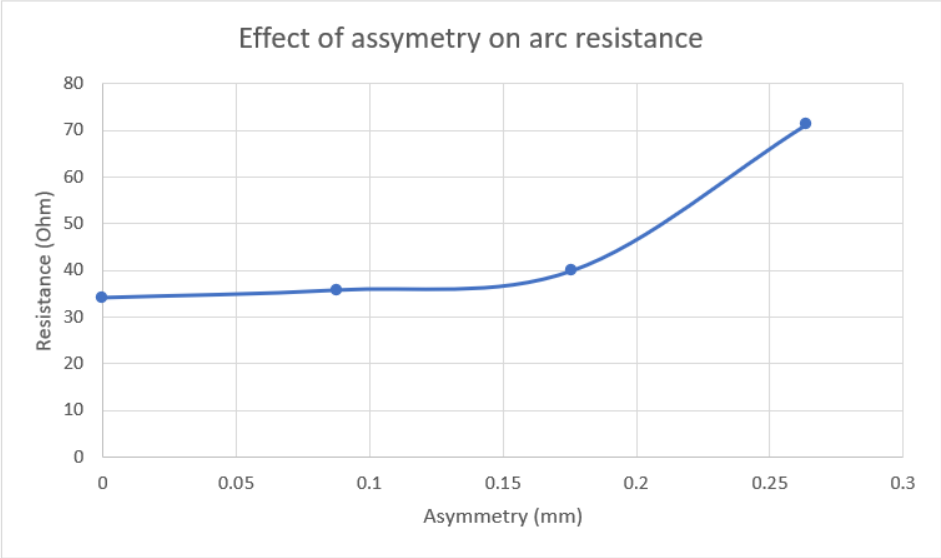

Figure 5.24 Arc 3D behaviour impact on the calculation of the gaseous medium resistance at cZ

the resistance for $\delta = 0.26mm$ is 80% more than the resistance associate with $\delta = 0.176mm$. This is while for the other δ values the change in resistance is smaller. As a conclusion, for a more 3D arc, the resistance is larger.

CHAPTER 6 CONCLUSION

This research was conducted to investigate the arc extinction in a 3D context using high order of accuracy schemes. The results of this investigation can be categorized as follows

1. The WENO scheme has a considerable effect on the flow properties (pressure, temperature, density) and the arc properties (radius, voltage, resistance). The comparison of the measurements with numerical temperature profiles suggests more accurate results are obtained by the WENO compared to the 1^{st} order method. However, more experimental data is still needed to validate both flow and arc properties.

2. The arc core is predicted more accurately as compared to the arc boundary. While the arc core is more dominated by the convective terms, in the arc boundary, the diffusive terms (viscosity related terms) become more important. Turbulence mixing has a major contribution in the fast transition that occurs from the hot plasma to the cold gas in the arc boundary.

   This research studies the capability of the Euler equations to capture the arc 3D effect and thus the results are more accurate in predicting the arc core than the arc boundary. For more accurate arc temperature profile in the boundaries, Navier-Stokes equations should be applied to the simulations and turbulence should be included, ideally withing an LES framework.

3. Arc 3D effects can be captured using Euler equations when a slight asymmetry is imposed on the arc initial conditions.

4. As δ (computational domain eccentricity) is increased, more asymmetry is introduced to the simulation and therefore, more 3D effects can be observed at CZ. The arc resistance is directly proportional to the 3D effects. This confirms the necessity of 3D arc simulation particularly at CZ.

5. Radiative energy is not negligible even at CZ when the lowest arc temperature values are observed. Although the current approaches zero, the plasma is still hot enough to emit radiative energy.

6.1 Limitations

The following limitations can be pointed out for the approach used in this research:

1. The computational domain used in this research is away from the walls and the electrodes. Despite the simplicity, the Dirichlet boundary conditions are applied on the faces of the computational box instead of the electrodes. This modelling error can be mitigated by considering the boundaries of the computational box as close to the electrodes as possible.

2. The structured Cartesian mesh used in this research is a pre-requisite for the 4^{th} order compact finite difference method used to calculate the Ohmic heating. The WENO scheme is also dependant on a uniform Cartesian mesh in which $\Delta x = \Delta y = \Delta z$. This means that this code cannot be applied to complex geometries without further modifications. Currently, Immersed Boundary Method (IBM) is under investigation by the research team to use Cartesian grid for more complex geometries.

3. While the 1^{st} order method takes 18 hrs to run, WENO's computational cost is 50 hrs for the same case (196,520 cells, $\Delta x = \Delta y = \Delta z = 0.176mm$, CFL=0.6, 20 cores of Intel(R) Core(TM) i9-9820X CPU @ 3.30GHz). This shows the considerable computational cost required by the WENO scheme which is due to the interpolations in 3 directions, the Gaussian integration on the faces and the high order time integration.

4. This research is based on the coupling with an in-house code (MC^3). The arc is initialized on MC^3 and the results are mapped on the 3D code developed in this research, to be ramped down to the CZ. The arc ignition cannot be simulated by the 3D code. Therefore, this code cannot be used as an end-to-end solution for the arc simulation.

6.2 Future Research

With this research being an opening to 3D arc extinction simulations, the 3D effects can be further investigated by carrying out the following improvements in future:

1. It will be helpful to add viscous terms to the Euler equations and study the arc extinction in a laminar flow context. This will increase the accuracy of arc boundary prediction and therefore, the radial temperature profile.

2. Turbulence modeling can be added to the 3D code for a better understating of the arc boundaries. PML model would be a helpful starting point since it has been addressed

in arc simulation literature. However, a better option would be LES which comes at a higher computational cost.

3. Regarding WENO, it is suggested that a finite difference approach replaces the finite volume approach. For finite difference based WENO schemes, the extension to multi-dimensions is faster and easier since the non-linearity problem does not exist and the Gaussian integration on the faces is not necessary.

4. Arc foot has been observed to move in this research, however, meaningful interpretation of this movement needs more investigation.

REFERENCES

[1] N. P. T. Basse, R. Bini, and M. Seeger, "Measured turbulent mixing in a small-scale circuit breaker model," *Appl. Opt.*, vol. 48, no. 32, pp. 6381–6391, Nov 2009. [Online]. Available: http://ao.osa.org/abstract.cfm?URI=ao-48-32-6381

[2] D. Swindler *et al.*, "Transient recovery voltage considerations in the application of medium-voltage circuit breakers," *IEEE Transactions on Industry Applications*, vol. 33, no. 2, pp. 383 – 8, 1997/03/. [Online]. Available: http://dx.doi.org/10.1109/28.567999

[3] I. P. Shkarofsky, *The Particle Kinetics of Plasmas*. Addison-Wesley.

[4] M. Boulos, P. Fauchais, and E. Pfender, *Thermal Plasmas: Fundamentals and Applications*. Springer US, 2013.

[5] P. M. Bellan, *Fundamentals of Plasma Physics*. Cambridge University Press, 2006.

[6] W. Feng-hua, J. Zhi-jian, and Z. Zi-shu, "Fluid flow modeling of arc plasma and bath circulation in dc electric arc furnace," *Journal of Iron and Steel Research International*, vol. 13, no. 5, pp. 7 – 13, Sept. 2006. [Online]. Available: http://dx.doi.org/10.1016/S1006-706X(06)60086-1

[7] P. Maruzewski *et al.*, "Simulation of arc-electrode interaction using sheath modelling in sf6 circuit-breakers," *Journal of Physics D (Applied Physics)*, vol. 35, no. 9, pp. 891 – 9, 2002/05/07. [Online]. Available: http://dx.doi.org/10.1088/0022-3727/35/9/309

[8] B. Chervy, A. Gleizes, and M. Razafinimanana, "Thermodynamic properties and transport coefficients in sf6-cu mixtures at temperatures of 300-30000 k and pressures of 0.1-1 mpa," *Journal of Physics D (Applied Physics)*, vol. 27, no. 6, pp. 1193 – 206, 1994/06/14. [Online]. Available: http://dx.doi.org/10.1088/0022-3727/27/6/017

[9] H. Pellegrin *et al.*, "Computation of the self-induced magnetic field in circuit-breaker arcs," *IEEE Transactions on Plasma Science*, vol. 25, no. 5, pp. 974 – 81, 1997/10/. [Online]. Available: http://dx.doi.org/10.1109/27.649609

[10] M. Seeger, "Perspectives on research on high voltage gas circuit breakers," *Plasma Chemistry and Plasma Processing*, vol. 35, no. 3, pp. 527 – 41, 2015/05/. [Online]. Available: http://dx.doi.org/10.1007/s11090-014-9595-4

[11] T. Christen, F. Kassubek, and R. Gati, "Radiative heat transfer and effective transport coefficients," in *Heat Transfer*, A. Belmiloudi, Ed. Rijeka: IntechOpen, 2011, ch. 4. [Online]. Available: https://doi.org/10.5772/13853

[12] V. Aubrecht and M. Bartlova, "Net emission coefficients of radiation in air and sf6 thermal plasmas," *Plasma Chemistry and Plasma Processing*, vol. 29, no. 2, pp. 131 – 47, 2009/04/. [Online]. Available: http://dx.doi.org/10.1007/s11090-008-9163-x

[13] M. Seeger *et al.*, "An integral arc model for ablation controlled arcs based on cfd simulations," *Journal of Physics D (Applied Physics)*, vol. 39, no. 10, pp. 2180 – 91, 2006/05/21. [Online]. Available: http://dx.doi.org/10.1088/0022-3727/39/10/029

[14] X. Zhang, J. Trepanier, and R. Camarero, "Numerical simulation of a 2 ka convection-stabilized nitrogen arc using cfd tools," *Journal of Physics D (Applied Physics)*, vol. 30, no. 23, pp. 3240 – 52, 1997/12/07. [Online]. Available: http://dx.doi.org/10.1088/0022-3727/30/23/008

[15] C. Franck and M. Seeger, "Application of high current and current zero simulations of high-voltage circuit breakers," *Contributions to Plasma Physics*, vol. 46, no. 10, pp. 787 – 97, 2006//. [Online]. Available: http://dx.doi.org/10.1002/ctpp.200610079

[16] M. Melot *et al.*, "Comparison of numerical models in radiative heat transfer with application to circuit-breaker simulations," *Mathematics and Computers in Simulation*, vol. 82, no. 12, pp. 2982 – 96, 2012/08/. [Online]. Available: http://dx.doi.org/10.1016/j.matcom.2012.07.002

[17] S. Eby, J. Trepanier, and X. Zhang, "Modelling radiative transfer in sf6 circuit-breaker arcs with the p-1 approximation," *Journal of Physics D (Applied Physics)*, vol. 31, no. 13, pp. 1578 – 88, 1998/07/07. [Online]. Available: http://dx.doi.org/10.1088/0022-3727/31/13/012

[18] J. C. Chai and S. V. Patankar, *Discrete-Ordinates and Finite-Volume Methods for Radiative Heat Transfer*. John Wiley Sons, Ltd, 2009, ch. 9, pp. 297–323. [Online]. Available: https://onlinelibrary.wiley.com/doi/abs/10.1002/9780470172599.ch9

[19] J. Trelles *et al.*, "Arc plasma torch modeling," *Journal of Thermal Spray Technology*, vol. 18, no. 5-6, pp. 728 – 52, 2009/12/. [Online]. Available: http://dx.doi.org/10.1007/s11666-009-9342-1

[20] Hassanzadeh, Pedram, "An efficient computational method for thermal radiation in participating media," 2007. [Online]. Available: http://hdl.handle.net/10012/3135

[21] D. Eichhoff *et al.*, "Study of an ablation-dominated arc in a model circuit breaker," *Journal of Physics D: Applied Physics*, vol. 45, no. 30, 2012. [Online]. Available: http://dx.doi.org/10.1088/0022-3727/45/30/305204

[22] S. Arabi, J.-Y. Trepanier, and R. Camarero, "Transient simulation of nozzle geometry change during ablation in high-voltage circuit breakers," *Journal of Physics D: Applied Physics*, vol. 48, no. 4, 2015. [Online]. Available: http://dx.doi.org/10.1088/0022-3727/48/4/045501

[23] M. T. C. Fang and Q. Zhuang, "Current zero behaviour of an SF_6 gas-blast arc. I. laminar flow," *Journal of Physics D Applied Physics*, vol. 25, pp. 1197–1204, Aug. 1992.

[24] C. Delalondre *et al.*, "Transient three dimensional simulation of electric arc," *High Temperature Material Processes: An International Quarterly of High-Technology Plasma Processes*, vol. 2, no. 1, pp. 129–142, 1998.

[25] M. T. C. Fang, Q. Zhuang, and X. J. Guo, "Current-zero behaviour of an SF6 gas-blast arc. II. turbulent flow," *Journal of Physics D: Applied Physics*, vol. 27, no. 1, pp. 74–83, jan 1994. [Online]. Available: https://doi.org/10.1088%2F0022-3727%2F27%2F1%2F011

[26] J. Yan, K. Nuttall, and M. Fang, "A comparative study of turbulence models for SF6 arcs in a supersonic nozzle," *Journal of Physics D (Applied Physics)*, vol. 32, no. 12, pp. 1401 – 6, 1999/06/21. [Online]. Available: http://dx.doi.org/10.1088/0022-3727/32/12/317

[27] C. Delalondre, S. Zakrai, and O. Simonin, "Turbulence Modeling in Electric Arcs," in *Abstracts of international symposium on heat and mass transfer under plasma conditions*, Izmir, 1994, p. 88. [Online]. Available: https://inis.iaea.org/search/search.aspx?orig{_}q=RN:28005403

[28] T.-H. Shih *et al.*, "New k- eddy viscosity model for high reynolds number turbulent flows," *Computers and Fluids*, vol. 24, no. 3, pp. 227 – 238, 1995. [Online]. Available: http://dx.doi.org/10.1016/0045-7930(94)00032-T

[29] V. Yakhot *et al.*, "Development of turbulence models for shear flows by a double expansion technique," *Physics of Fluids A (Fluid Dynamics)*, vol. 4, no. 7, pp. 1510 – 20, 1992/07/. [Online]. Available: http://dx.doi.org/10.1063/1.858424

[30] A. Iordanidis and C. Franck, "Self-consistent radiation-based simulation of electric arcs: Ii. application to gas circuit breakers," *Journal of Physics D: Applied*

Physics, vol. 41, no. 13, pp. 135 206 (9 pp.) –, 2008/07/07. [Online]. Available: http://dx.doi.org/10.1088/0022-3727/41/13/135206

[31] M. Kato *et al.*, *Modelling Flow-induced Oscillations in Turbulent Flow Around a Square Cylinder*. University of Manchester, Institute of Science and Technology, 1992. [Online]. Available: https://books.google.ca/books?id=ZOEJMwEACAAJ

[32] J. SMAGORINSKY, "General circulation experiments with the primitive equations," *Monthly Weather Review*, vol. 91, no. 3, pp. 99–164, 1963. [Online]. Available: https://doi.org/10.1175/1520-0493(1963)091<0099:GCEWTP>2.3.CO;2

[33] M. Germano *et al.*, "A dynamic subgrid-scale eddy viscosity model," *Physics of Fluids A (Fluid Dynamics)*, vol. 3, no. 7, pp. 1760 – 5, 1991/07/. [Online]. Available: http://dx.doi.org/10.1063/1.857955

[34] N. Markatos, "The mathematical modelling of turbulent flows," *Applied Mathematical Modelling*, vol. 10, no. 3, pp. 190 – 220, 1986/06/. [Online]. Available: http://dx.doi.org/10.1016/0307-904X(86)90045-4

[35] G. Frind and J. Rich, "Recovery speed of axial flow gas blast interrupter: Dependence on pressure and di/dt for air and sf6." *IEEE Transactions on Power Apparatus and Systems*, vol. PAS-93, no. 5, pp. 1675 – 1684, 1974.

[36] W. Hermann *et al.*, "Investigation on the physical phenomena around current zero in hv gas blast breakers." *IEEE Transactions on Power Apparatus and Systems*, vol. PAS-95, no. 4, pp. 1165 – 1176, 1976.

[37] D. Biswas *et al.*, "Studies on fluid-plasma interaction associated with basic gas blast characteristics based on a high-order les turbulence model," *IEEJ Transactions on Power and Energy*, vol. 133, no. 5, pp. 417 – 423, 2013. [Online]. Available: http://dx.doi.org/10.1541/ieejpes.133.417

[38] J. Zhang, "An explicit fourth-order compact finite difference scheme for three-dimensional convection-diffusion equation," *Communications in Numerical Methods in Engineering*, vol. 14, no. 3, pp. 209 – 18, 1998/03/. [Online]. Available: http://dx.doi.org/10.1002/(SICI)1099-0887(199803)14:3<209::AID-CNM139>3.0.CO;2-P

[39] P. Roe, "Approximate riemann solvers, parameter vectors, and difference schemes," *Journal of Computational Physics*, vol. 135, no. 2, pp. 250 – 8, 1997/08/. [Online]. Available: http://dx.doi.org/10.1006/jcph.1997.5705

[40] H. Van Der Vorst, "Bi-cgstab: a fast and smoothly converging variant of bi-cg for the solution of nonsymmetric linear systems," *SIAM Journal on Scientific and Statistical Computing*, vol. 13, no. 2, pp. 631 – 44, 1992/03/, smoothly converging;nonsymmetric linear systems;conjugate gradients-squared;bi-conjugate gradients;. [Online]. Available: http://dx.doi.org/10.1137/0913035

[41] C.-W. Shu, *Essentially non-oscillatory and weighted essentially non-oscillatory schemes for hyperbolic conservation laws.* Berlin, Heidelberg: Springer Berlin Heidelberg, 1998, pp. 325–432. [Online]. Available: https://doi.org/10.1007/BFb0096355

[42] A. Harten *et al.*, "Uniformly high order accurate essentially non-oscillatory schemes. iii," *Journal of Computational Physics*, vol. 71, no. 2, pp. 231 – 303, 1987/08/. [Online]. Available: http://dx.doi.org/10.1016/0021-9991(87)90031-3

[43] X.-D. Liu, S. Osher, and T. Chan, "Weighted essentially non-oscillatory schemes," *Journal of Computational Physics*, vol. 115, no. 1, pp. 200 – 212, 1994. [Online]. Available: http://www.sciencedirect.com/science/article/pii/S0021999184711879

[44] G.-S. Jiang and C.-W. Shu, "Efficient implementation of weighted ENO schemes," *Journal of Computational Physics*, vol. 126, no. 1, pp. 202 – 228, 1996. [Online]. Available: http://www.sciencedirect.com/science/article/pii/S0021999196901308

[45] R. Liebermann and J. Lowke, "Radiation emission coefficients for sulfur hexafluoride arc plasmas," *Journal of Quantitative Spectroscopy and Radiative Transfer*, vol. 16, no. 3, pp. 253 – 264, 1976. [Online]. Available: http://www.sciencedirect.com/science/article/pii/0022407376900674

[46] R. Wang, H. Feng, and R. J. Spiteri, "Observations on the fifth-order weno method with non-uniform meshes," *Applied Mathematics and Computation*, vol. 196, no. 1, pp. 433 – 447, 2008. [Online]. Available: http://dx.doi.org/10.1016/j.amc.2007.06.024

[47] R. Abgrall, "On essentially non-oscillatory schemes on unstructured meshes: analysis and implementation," *Journal of Computational Physics*, vol. 114, no. 1, pp. 45 – 58, Sept. 1994. [Online]. Available: http://dx.doi.org/10.1006/jcph.1994.1148

[48] C. Hu and C.-W. Shu, "Weighted essentially non-oscillatory schemes on triangular meshes," *Journal of Computational Physics*, vol. 150, no. 1, pp. 97 – 127, 1999/03/20. [Online]. Available: http://dx.doi.org/10.1006/jcph.1998.6165

[49] V. Titarev and E. Toro, "Finite-volume weno schemes for three-dimensional conservation laws," *Journal of Computational Physics*, vol. 201, no. 1, pp. 238 – 60, 2004/11/20. [Online]. Available: http://dx.doi.org/10.1016/j.jcp.2004.05.015

[50] E. Toro, *Riemann Solvers and Numerical Methods for Fluid Dynamics: A Practical Introduction*. Springer Berlin Heidelberg, 2009.

[51] C.-W. Shu and S. Osher, "Efficient implementation of essentially non-oscillatory shock-capturing schemes," *Journal of Computational Physics*, vol. 77, no. 2, pp. 439 – 471, 1988. [Online]. Available: http://www.sciencedirect.com/science/article/pii/0021999188901775

[52] S. Arabi, J.-Y. Trepanier, and R. Camarero, "A simple extension of roe's scheme for real gases," *Journal of Computational Physics*, vol. 329, pp. 16 – 28, 2017/01/15. [Online]. Available: http://dx.doi.org/10.1016/j.jcp.2016.10.067

[53] D. Leseberg, "Holographische Interferometrie und optische Spektroskopie an einem SF6-Schaltlichtbogen," Ph.D. dissertation, Aachen, 1982, aachen, Techn. Hochsch., Diss., 1982. [Online]. Available: http://publications.rwth-aachen.de/record/68289

[54] R. Zhang, M. Zhang, and C.-W. Shu, "High order positivity-preserving finite volume weno schemes for a hierarchical size-structured population model," *Journal of Computational and Applied Mathematics*, vol. 236, no. 5, pp. 937 – 949, 2011, the 7th International Conference on Scientific Computing and Applications, June 13–16, 2010, Dalian, China. [Online]. Available: http://www.sciencedirect.com/science/article/pii/S0377042711002548

[55] X. Zhang and C.-W. Shu, "Positivity-preserving high order finite difference weno schemes for compressible euler equations," *Journal of Computational Physics*, vol. 231, no. 5, pp. 2245 – 2258, 2012. [Online]. Available: http://www.sciencedirect.com/science/article/pii/S0021999111006759

[56] D. V. Kotov, H. M. Yee, and B. Sjögreen, "Comparative study on high-order positivity-preserving weno schemes," 2014.

APPENDIX A FOURTH ORDER COMPACT FINITE DIFFERENCE SCHEME

A 3D convection-diffusion equation has the form of the following equation

$$\Delta u(x,y,z) + (\lambda(x,y,z), \mu(x,y,z), \Phi(x,y,z)).\nabla u(x,y,z) = f(x,y,z)$$

the 19 point discretization to find u follows the following formula

$$\sum_{l=0}^{18} c_l u_l = F_0$$

where $c_0 - c_{18}$ and F_0 are given by

$$c_0 = -[24 + h^2(\lambda_0^2 + \mu_0^2 + \Phi_0^2) + h(\lambda_1 - \lambda_3 + \mu_2 - \mu_4 + \Phi_5 - \Phi_6)]$$

$$\begin{aligned} c_1 = 2 &- \frac{h}{4}(2\lambda_0 - 3\lambda_1 - \lambda_2 + \lambda_3 - \lambda_4 - \lambda_5 - \lambda_6) \\ &+ \frac{h^2}{8}[4\lambda_0^2 + \lambda_0(\lambda_1 - \lambda_3) + \mu_0(\lambda_2 - \lambda_4) + \Phi_0(\lambda_5 - \lambda_6)] \end{aligned}$$

$$\begin{aligned} c_2 = 2 &- \frac{h}{4}(2\mu_0 - \mu_1 - 3\mu_2 - \mu_3 + \mu_4 - \mu_5 - \mu_6) \\ &+ \frac{h^2}{8}[4\mu_0^2 + \lambda_0(\mu_1 - \mu_3) + \mu_0(\mu_2 - \mu_4) + \Phi_0(\mu_5 - \mu_6)] \end{aligned}$$

$$\begin{aligned} c_3 = 2 &+ \frac{h}{4}(2\lambda_0 + \lambda_1 - \lambda_2 - 3\lambda_3 - \lambda_4 - \lambda_5 - \lambda_6) \\ &+ \frac{h^2}{8}[4\lambda_0^2 - \lambda_0(\lambda_1 - \lambda_3) - \mu_0(\lambda_2 - \lambda_4) - \Phi_0(\lambda_5 - \lambda_6)] \end{aligned}$$

$$c_4 = 2 + \frac{h}{4}(2\mu_0 - \mu_1 + \mu_2 - \mu_3 - 3\mu_4 - \mu_5 - \mu_6)$$
$$+ \frac{h^2}{8}[4\mu_0^2 - \lambda_0(\mu_1 - \mu_3) - \mu_0(\mu_2 - \mu_4) - \Phi_0(\mu_5 - \mu_6)]$$

$$c_5 = 2 - \frac{h}{4}(2\Phi_0 - \Phi_1 - \Phi_2 - \Phi_3 - \Phi_4 - 3\Phi_5 + \Phi_6)$$
$$+ \frac{h^2}{8}[4\Phi_0^2 + \lambda_0(\Phi_1 - \Phi_3) + \mu_0(\Phi_2 - \Phi_4) - \Phi_0(\Phi_5 - \Phi_6)]$$

$$c_6 = 2 + \frac{h}{4}(2\Phi_0 - \Phi_1 - \Phi_2 - \Phi_3 - \Phi_4 + \Phi_5 - 3\Phi_6)$$
$$+ \frac{h^2}{8}[4\Phi_0^2 - \lambda_0(\Phi_1 - \Phi_3) - \mu_0(\Phi_2 - \Phi_4) - \Phi_0(\Phi_5 - \Phi_6)]$$

$$c_7 = 1 + \frac{h}{2}(\lambda_0 + \mu_0) + \frac{h}{8}(\lambda_2 - \lambda_4 + \mu_1 - \mu_3) + \frac{h^2}{4}\lambda_0\mu_0$$

$$c_8 = 1 - \frac{h}{2}(\lambda_0 - \mu_0) - \frac{h}{8}(\lambda_2 - \lambda_4 + \mu_1 - \mu_3) - \frac{h^2}{4}\lambda_0\mu_0$$

$$c_9 = 1 - \frac{h}{2}(\lambda_0 + \mu_0) - \frac{h}{8}(\lambda_2 - \lambda_4 + \mu_1 - \mu_3) + \frac{h^2}{4}\lambda_0\mu_0$$

$$c_10 = 1 + \frac{h}{2}(\lambda_0 - \mu_0) - \frac{h}{8}(\lambda_2 - \lambda_4 + \mu_1 - \mu_3) - \frac{h^2}{4}\lambda_0\mu_0$$

$$c_11 = 1 + \frac{h}{2}(\lambda_0 + \Phi_0) + \frac{h}{8}(\lambda_5 - \lambda_6 + \Phi_1 - \Phi_3) + \frac{h^2}{4}\lambda_0\Phi_0$$

$$c_1 2 = 1 + \frac{h}{2}(\mu_0 + \Phi_0) + \frac{h}{8}(\mu_5 - \mu_6 + \Phi_2 - \Phi_4) + \frac{h^2}{4}\mu_0\Phi_0$$

$$c_1 3 = 1 - \frac{h}{2}(\lambda_0 - \Phi_0) - \frac{h}{8}(\lambda_5 - \lambda_6 + \Phi_1 - \Phi_3) - \frac{h^2}{4}\lambda_0\Phi_0$$

$$c_1 4 = 1 - \frac{h}{2}(\mu_0 - \Phi_0) - \frac{h}{8}(\mu_5 - \mu_6 + \Phi_2 - \Phi_4) - \frac{h^2}{4}\mu_0\Phi_0$$

$$c_1 5 = 1 + \frac{h}{2}(\lambda_0 - \Phi_0) - \frac{h}{8}(\lambda_5 - \lambda_6 + \Phi_1 - \Phi_3) - \frac{h^2}{4}\lambda_0\Phi_0$$

$$c_1 6 = 1 + \frac{h}{2}(\mu_0 - \Phi_0) - \frac{h}{8}(\mu_5 - \mu_6 + \Phi_2 - \Phi_4) - \frac{h^2}{4}\mu_0\Phi_0$$

$$c_1 7 = 1 - \frac{h}{2}(\lambda_0 + \Phi_0) + \frac{h}{8}(\lambda_5 - \lambda_6 + \Phi_1 - \Phi_3) + \frac{h^2}{4}\lambda_0\Phi_0$$

$$c_1 8 = 1 - \frac{h}{2}(\mu_0 + \Phi_0) + \frac{h}{8}(\mu_5 - \mu_6 + \Phi_2 - \Phi_4) + \frac{h^2}{4}\mu_0\Phi_0$$

$$F_0 = \frac{h^2}{2}(6f_0 + f_1 + f_2 + f_3 + f_4 + f_5 + f_6) + \frac{h^3}{4}[\lambda_0(f_1 - f_3) + \mu_0(f_2 - f_4) + \Phi_0(f_5 - f_6)]$$